AVO ANALYSIS AND IMPEDANCE INVERSION
FOR FLUID PREDICTION IN HOOVER FIELD, GULF OF MEXICO

A Thesis

Presented to

the Faculty of the Department of Earth and Atmospheric Sciences

University of Houston

In Partial Fulfillment

of the Requirements for the Degree

Master of Science

By

Charles Bassey Inyang

May 2009

AVO ANALYSIS AND IMPEDANCE INVERSION FOR FLUID PREDICTION IN HOOVER FIELD, GULF OF MEXICO

Charles Bassey Inyang

APPROVED:

Dr. John Castagna, Chairman

Dr. Janok Bhattacharya, Member

Dr. Tad Smith, Member

Dean, College of Natural Sciences and Mathematics

Acknowledgements

My sincere gratitude goes to my adviser for his timely advice and encouragement. I also wish to thank my committee members, Dr. Bhattacharya and Dr. Tad Smith for their support and advice. I wish to thank Dr. Casey and administrative staff of the department for their support. I acknowledge all students who provided assistance during this research and preparation for defense; especially Jeremy, Jadranka, Felipe, Chirag, and Okey. I acknowledge the management and staff of Fusion Petroleum Technologies Incorporated for their financial, technical, and moral support. I acknowledge all Professors whose classes I took, which enabled me to carry out this research. I also acknowledge Jay and Santos for IT support. I thank my family for their unconditional support and encouragement. I also thank Inyang and Eji Effiong, Emeka Onuoha, Daniel and Amaka Dei, DC SALT, my house fellowship, RCCG dominion chapel, friends and colleagues for their support, encouragement and prayers. For all those whose names I did not mention, it wouldn't have been possible without you all. Finally, I wish to thank Almighty God for life, favor, perseverance, and success even during rough and tough times.

AVO ANALYSIS AND IMPEDANCE INVERSION
FOR FLUID PREDICTION IN HOOVER FIELD, GULF OF MEXICO (GOM)

An Abstract of a Thesis

Presented to

the Faculty of the Department of Earth and Atmospheric Sciences

University of Houston

In Partial Fulfillment

of the Requirements for the Degree

Master of Science

By

Charles Bassey Inyang

May 2009

Abstract

The Hoover deep-water field reservoir, comprises low-impedance turbidite oil sands, and is a bright spot which exhibits Class IV AVO characteristics. Although the AVO effect on the hydrocarbon is minimal, conventional AVO modeling and analysis on synthetics from logs and extracted traces from near- and far-angle stacks show that one can discriminate oil from brine for which amplitude drops relatively faster with offset. This is achieved by using cross plots and attributes derived from AVO intercept (A), gradient (B), or reflection coefficients (Rp and Rs) such as scaled Poisson's ratio, fluid factor, and sum of reflection coefficients. Both absolute and relative impedance inversion methods, applied on the near- and far-angle stacked volumes, also identify the hydrocarbon-saturated section of the reservoir as a bright spot. The far-angle stack impedance volume shows a reduction in the number of bright spots, compared to the near-angle stack. Inversion results also show that the reservoir is not as homogenous as observed on the input seismic. There is variation in horizontal impedance contrast between oil- and brine-saturated reservoir sands, depending on the inversion method used. Inversions carried out with or without using an initial model, also yield similar results. Although low impedance associated with bright amplitudes is not an unambiguous indicator of hydrocarbon sands, AVO analysis, as well as inversion of near- and far-stacked seismic data, offer an opportunity for additional measurements which can be used to reduce risk.

Table of contents

List of figures

List of tables

Chapter 1: Introduction

1.1 Introduction

Deep-water or turbidite systems are “sediments that have been transported under gravity-flow processes and deposited in the marine environment, beneath storm-wave base, from the slope to the floor of the basin” (Slatt, 2006, p.339). According to Slatt, “engineering definition of deep water refers to offshore reservoirs that have been drilled in modern water depths more than 500 m” (p.340). It has been observed that discoveries in the deep-water have been increasing rapidly, although it was less than 5 % of the world’s oil production in 2007 (Weimer and Slatt, 2007). Bright spots have been recognized as potential hydrocarbon indicators, but it has also been observed that they are not unique to hydrocarbons, as they can also be caused by the presence of lithology such as coal, over pressured shales, and high porosity sands (Chiburis et al., 1993; Sen, 2006). Without consideration of the AVO response, the uncertainty of the interpretation increases. Bright spots are common in deep-water reservoirs in the Gulf of Mexico, of which the oil-saturated Hoover field reservoir is a typical example.

Burtz et al. (2002) reported that the AVO effect is minimal within the Hoover Field reservoir sands. However, no results of any AVO modeling or analysis to discriminate hydrocarbon from brine were provided to support this claim. They had also carried out band-limited impedance inversion with which they identified the oil-saturated sands (Fig. 1.1) and predicted the net-oil thickness (Fig. 1.2). They concluded that this gives a good representation of intrinsic rock properties. However, the area of investigation was limited to the central portion of the survey, and lateral extent of the reservoir sands within the survey area was not determined.

This research applies conventional AVO analysis techniques and post-stack impedance inversion methods on seismic and well-log data (1) to discriminate low-impedance oil-saturated reservoir sands from brine-saturated reservoir sands, (2) to delineate the distribution of potential oil-saturated reservoir sands in the entire survey area, and (3) compare the effectiveness of inversion methods used in fluid and lithology identification.

1.2 Geologic setting

1.2.1 Gulf of Mexico

The Gulf of Mexico is described by Boorman et al. (2006, p.15) "as a roughly circular structural basin, approximately 1,500 km in diameter, filled with up to 15 km of sediments ranging in age from Late Triassic to Holocene". They also added that about 20 % of the surface area lies in water depth greater than 3,000 m (≈9800 ft). It covers a surface area of 1,500,000km^2 (≈579,000 mi^2); it is somewhat shallow along the coastal continental shelf areas and is deepest in the Sigsbee Deep at about 4000 m (≈13,100 ft) (http://www.worldatlas.com/aatlas/infopage/gulfofmexico.htm) (Figs. 1.3 and 1.4). It was formed as a result of sea-floor spreading, which resulted from the break up of Pangea, and it is characterized by widespread evaporite deposits, which form and destroy hydrocarbon traps (Boorman et al., 2006).

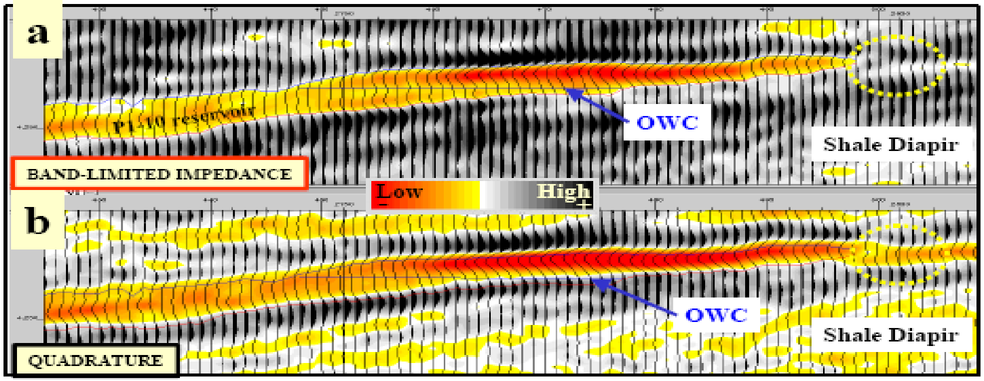

Figure 1.1: Acoustic impedance inversion results (a) band-limited impedance and (b) quadrature (from Burtz et al., 2002).

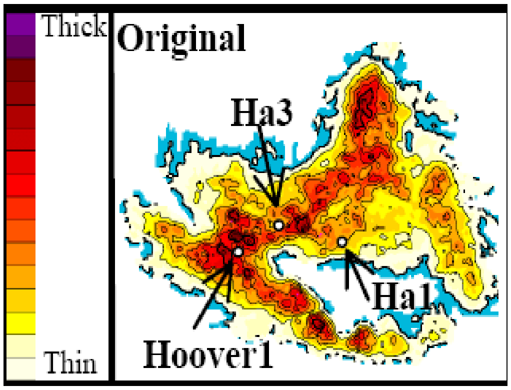

Figure 1.2: Prediction map of net-oil thickness before drilling HA-3 (from Burtz et al., 2002).

Figure 1.3: Location map of the Gulf of Mexico (from worldatlas.com)

1.2.2 Hoover Field

The Hoover field, discovered in 1997, is located 160 miles (≈257500 m) south of Galveston, Texas in 1463 m (4800 ft) of water, (Fig. 1.4) in the Diana mini-basin (Burtz et al., 2002). Cogswell (2001) outlined its reservoir-sand properties as follows: it is an unconsolidated deep-water turbidite in a proximal/channelized position relative to the sediment entry point into the P1:10 basin; its average permeability is ≈1.2 darcies, and the Pliocene-aged reservoir sand thins out as it gets over the structurally high portions of the field. He further observed that the hydrocarbon-trapping mechanism is a low-relief anticline. It is associated with an underlying deep-seated salt structure; is an oil only reservoir, with API gravity of 30°, and has a "bright spot" seismic signature (Fig. 1.5).

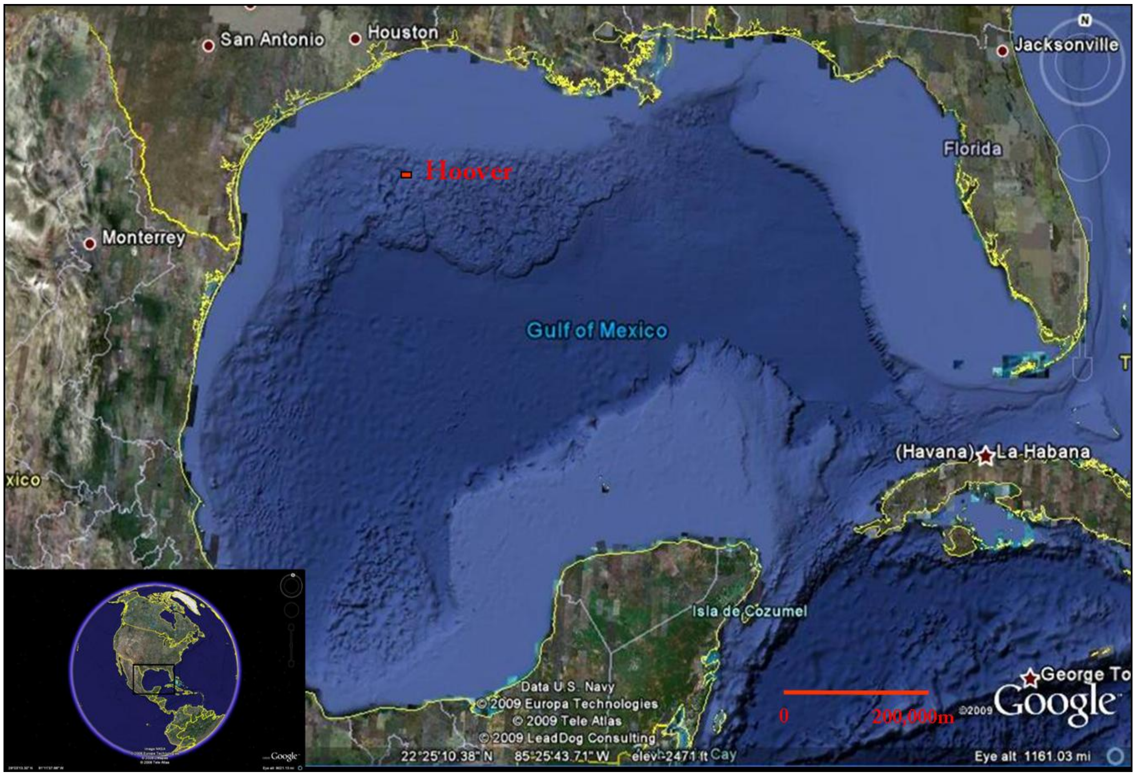

Figure 1.4: Map showing the location of Hoover field in the Gulf of Mexico (modified from www.googleearth.com).

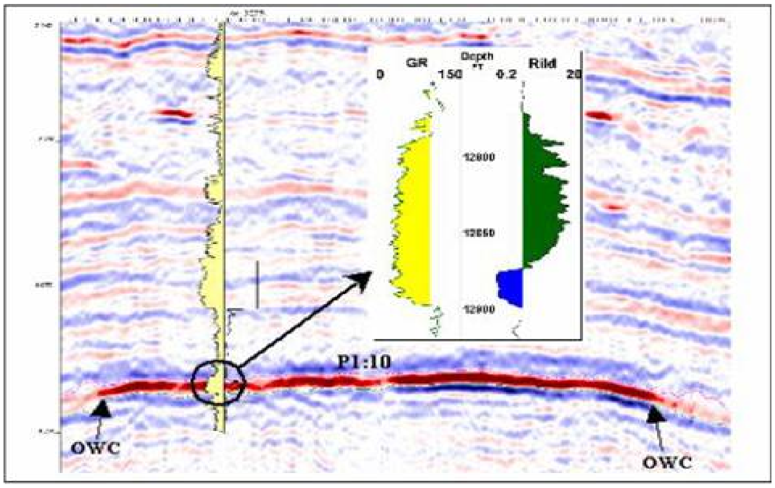

Figure 1.5: Seismic section with log through the Hoover P1:10 reservoir horizon showing the bright spot, oil-water contact and some reservoir properties (from Cogswell, 2001).

1.3 Data acquisition and processing

Seismic data and well logs used for this research were provided by Exxon Mobil Exploration Company (EMEC). The seismic data include: full-stacked, near- (0-15^o) and far- (30-42^o) angle stacked volumes (Figs. 1.6, 1.7 and 1.8 respectively). They were acquired by Veritas in 1997-1999, processed in 1999-2000 as Kirchhoff pre-stack time migration, controlled phase and true amplitude. The dimension is between ILN (inline) 31800 and 34290 (numbering increment of 5) and CDP/XLN (crossline) 2130 and 3422 (numbering increment of 1). ILN spacing is 19.81 m (65 ft), XLN spacing is 12.50 m (41 ft), sample rate is 4 ms and volume is limited to 5 sec (1251 samples). This survey covers an area of about 163,000,000 m^2 (1,754,000,000 ft^2). Available well logs include: gamma ray, resistivity, P-wave sonic, density, caliper, and neutron porosity. However, only wells that pass through the reservoir and have at least a density or P-wave sonic log were used in this study.

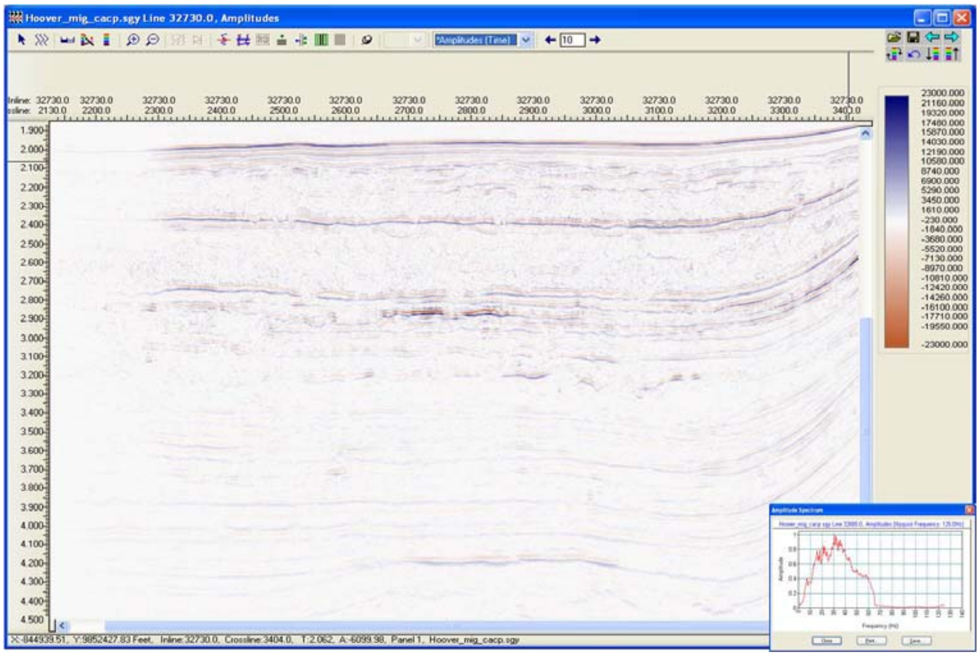

Figure 1.6: Full-stacked seismic section with frequency spectrum of 0-65 Hz and dominant frequency of about 32 Hz (bottom right).

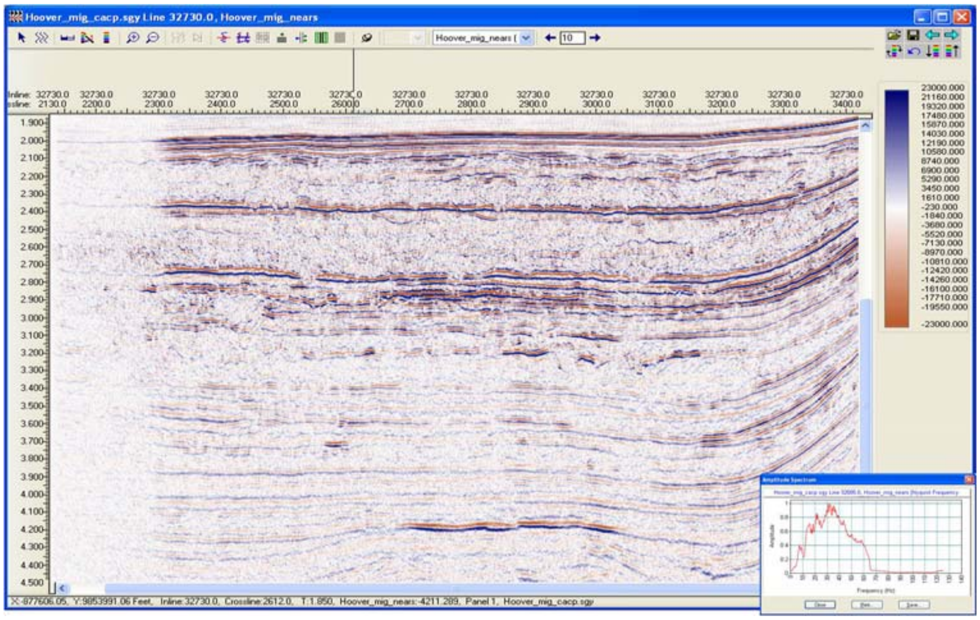

Figure 1.7: Near-stacked seismic section (0^o-15^o) with frequency spectrum of 0-65 Hz and dominant frequency of about 32 Hz (bottom right).

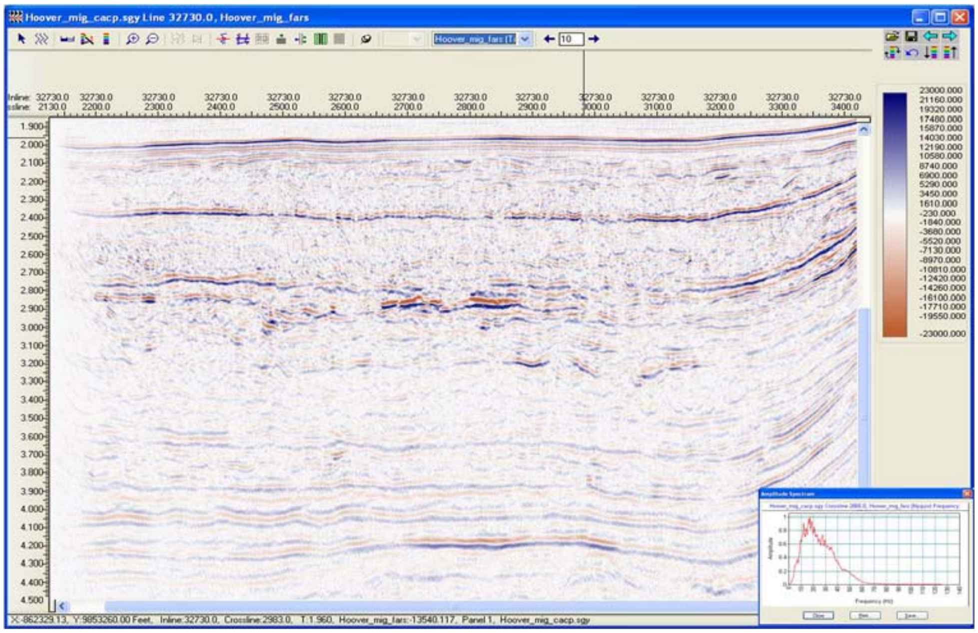

Figure 1.8: Far-stacked seismic section (30-42^{o}) with frequency spectrum of 0-65 Hz and dominant frequency of about 18 Hz (bottom right).

1.4 Software used

In the course of carrying out this research, the software packages used include: Schlumberger's Geoframe and SMT's Kingdom for three-dimensional (3D) seismic data interpretation, Fusion's ThinMAN for high-resolution band-limited impedance inversion, Halliburton's ProMAX for generating gathers from angle stacks, and Hampson-Russell's Elog, AVO, and STRATA for log analysis, AVO modeling, and analysis and impedance inversion respectively.

1.5 Research methodology

The first part of this research focuses on 3D interpretation of seismic data to understand the structure and stratigraphy of the study area, and to identify potential hydrocarbon-saturated areas in the reservoir from interpreted horizons and time slices by the identification of anomalies, as well as geologically or geomorphologically meaningful patterns in plan and/or cross-section view (Posamentier, et al., 2007).

This is followed by well-log correlation with seismic and log interpretation for identification of anomalous zones, to determine lithology, fluid content, porosity, water saturation, and depositional environment in the study area. Elog, used for this purpose, enables creation of new logs using empirical and theoretical transforms, as well as well-log correlation with seismic and crossplotting.

AVO modeling using synthetic seismic data to investigate the effect of fluid on seismic signature is also carried out. This is carried out through the creation of synthetic seismics from logs after fluid substitution, the creation of AVO curves for different fluids, and the extraction and crossplotting of conventional AVO attributes. AVO analysis is also carried out on gathers generated from the near- and far-stacked seismics.

Model-based, band-limited and sparse-spike Acoustic Impedance (AI) inversion using STRATA is carried out to identify impedance contrasts, and determine possible fluid saturated zones and the lateral extent of the reservoir in the field. These inversions are carried out with the aid of sonic and density logs, interpreted horizons, extracted wavelet and near stacked seismic volume. High-resolution band-limited impedance inversion is also carried out on the near- and far-stacked seismics with the help of ThinMAN, a commercial spectral inversion tool.

The last phase is the integration and interpretation of results from seismic, logs, horizons, time slices, and inversion. The research workflow is as shown in fig 1.9.

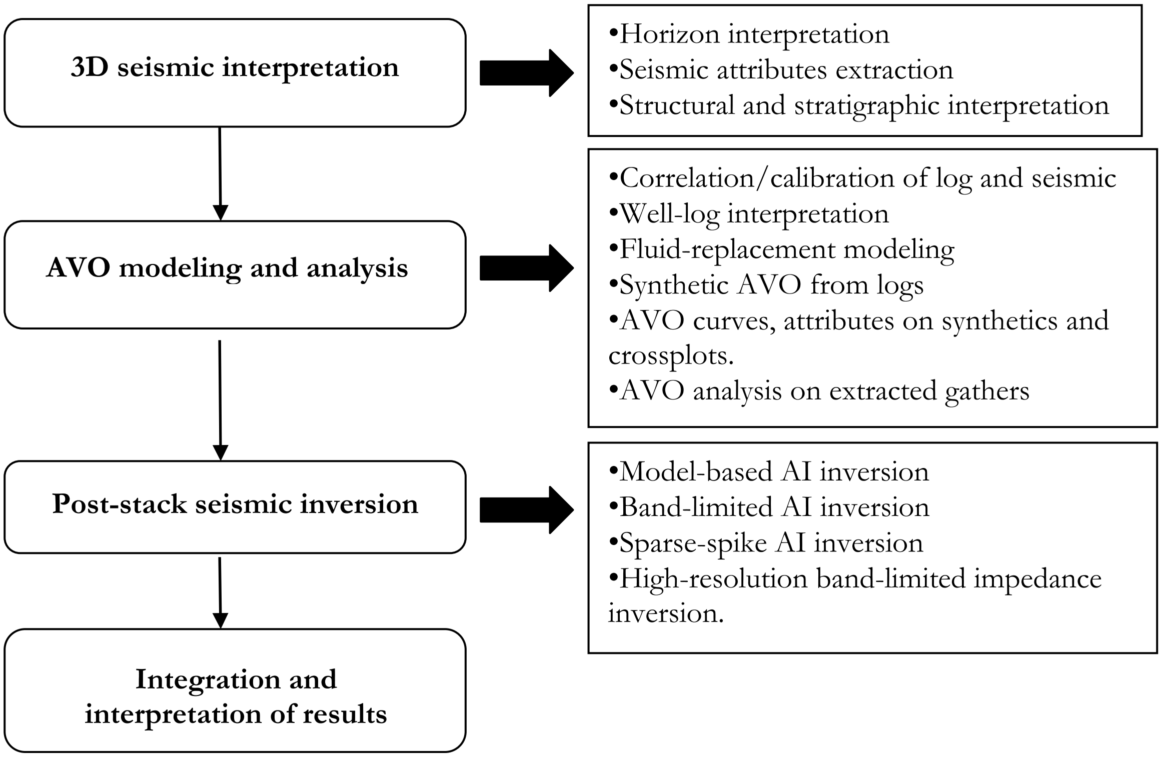

Figure 1.9 Research work flow

Chapter 2: Three-dimensional (3D) seismic data interpretations

2.1 Introduction

The Hoover Field is made of reservoir sands which are unconsolidated turbidites (Cogswell, 2001). A typical deep-water physiography is shown in figure 2.1. This chapter looks at stratigraphic, structural, and fluid information that can be obtained from 3D interpretation of seismic volumes. For this purpose, attributes extracted from the near-, far-, and full-stacked seismic volumes are analyzed. The base map of the survey area is shown in figure 2.2.

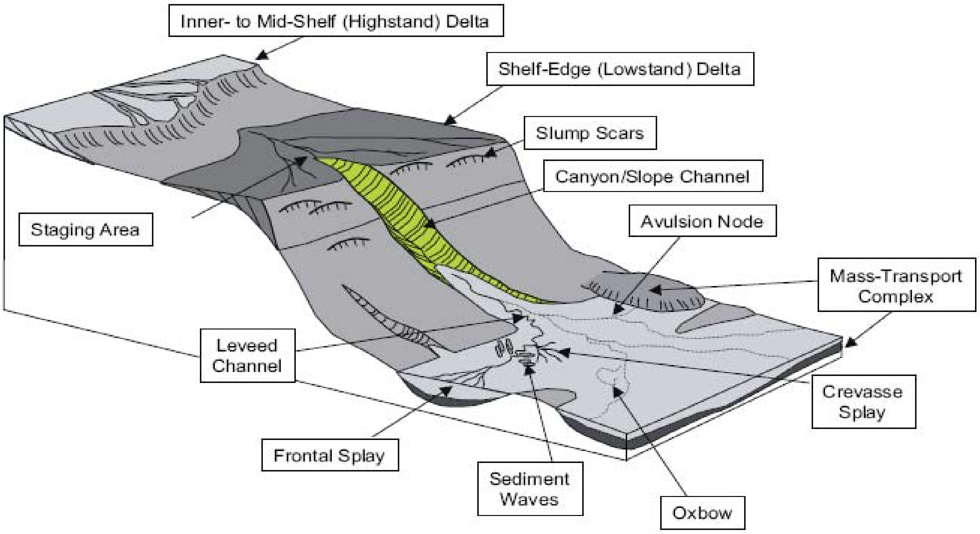

Figure 2.1: Deep-water physiography (from Posamentier and Walker, 2006)

Brown (2004) noted that a study of horizontal sections and horizon slices can provide information on ancient stratigraphy, which is comparable to present-day stratigraphy. Posamentier et al. (2007) provided an outline of the steps that may be followed in analyzing these depositional sequences. A summary of the steps used in this research is shown below (not necessarily in the order listed):

- Horizon picking
- Contouring and time-structure map on horizon
- Interval-based attributes analysis, whereby attributes such as: root-mean-square (RMS) amplitude, and maximum/minimum amplitude, are extracted from an interval above and below an interpreted horizon
- Horizon-based attributes extraction such as amplitude, dip magnitude, and dip azimuth.

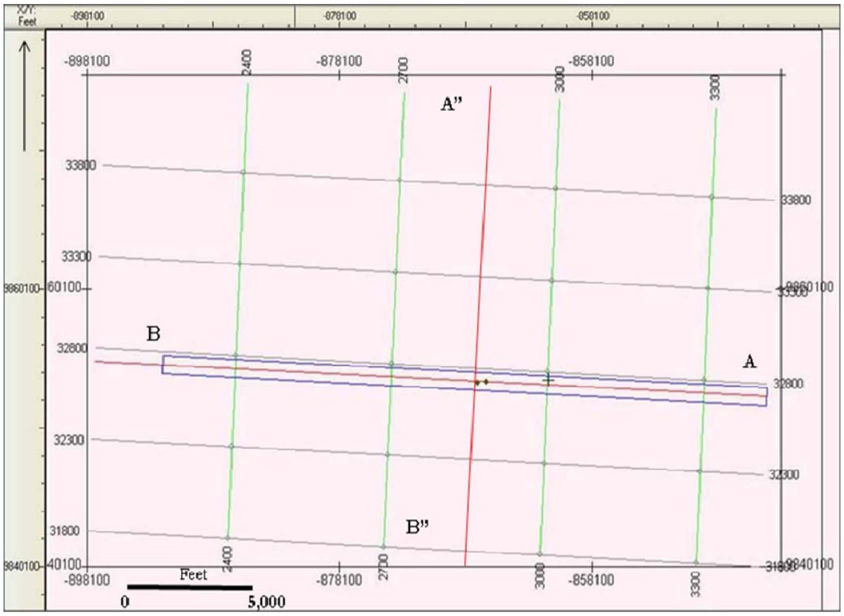

Figure 2.2: Base map of survey area, showing an inline, B-A, crossline, A"-B" and location of two wells (green dots).

2.2 Horizon interpretation

Sheriff (2002, p.178) described a horizon as "the surface separating two different rock layers". Gao (2007) described it as "an interpretational concept that separates different geological units such as: water from shallow sediments, sedimentary rock from salt diapirs or Tertiary clastics from Mesozoic carbonates". Six (6) horizons were manually picked on the near-stacked seismic from the water bottom at about 2000 ms to the reservoir at about 4200 ms (Figs. 2.3 and 2.4), and three (3) horizons on the far-stacked seismic. These were based on strong and continuous reflections on seismic volume peaks, observed at the bottom of sand units and mass-transport complexes in log HA-1, after which they were interpolated. However, only three (3) of these interpreted horizons (hor_1b, 4 and 5) are discussed, based on the clarity and uniqueness of their features. These were selected to reflect the general stratigraphic and structural features observed in the survey area. It is observed that reflection strength on the seismic reduces with depth as a result of the loss of high frequencies. However, a bright spot (strong reflection) is observed at about 4200 ms (Fig. 2.5). It should also be noted that these picked horizons will also be used to guide the interpolation of the initial model during seismic inversion.

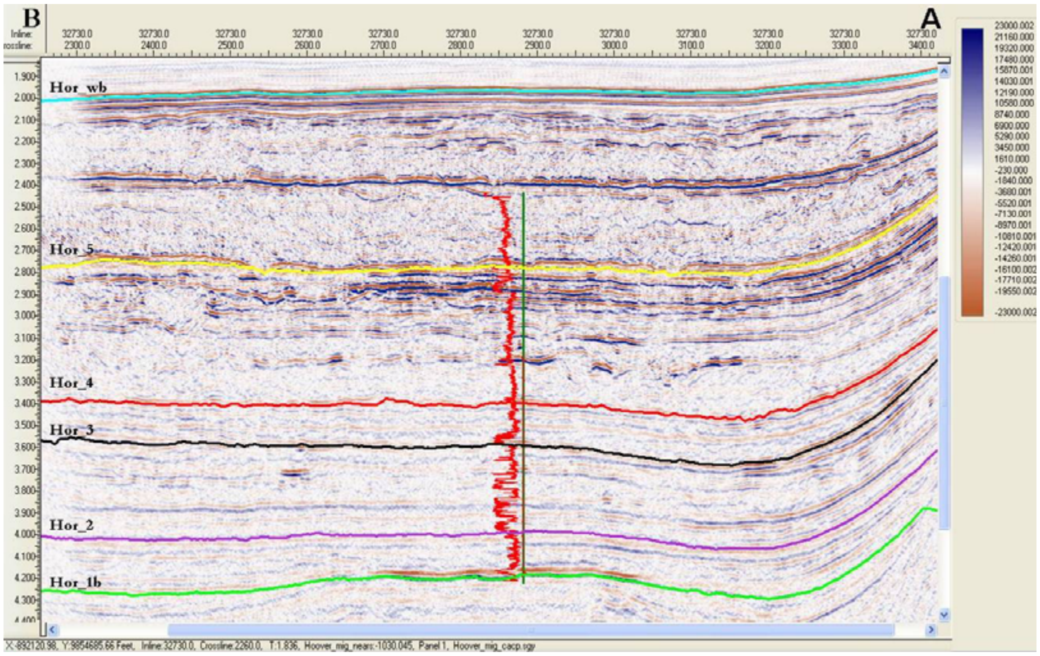

Figure 2.3: Inline view of interpreted horizons on near-stacked volume.

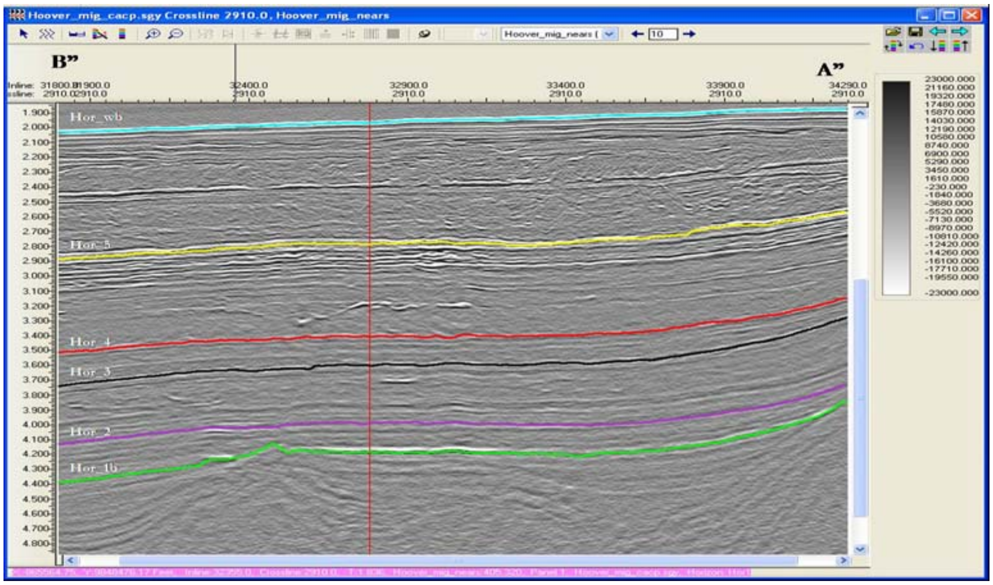

Figure 2.4: Crossline view of interpreted horizons on near-stacked volume.

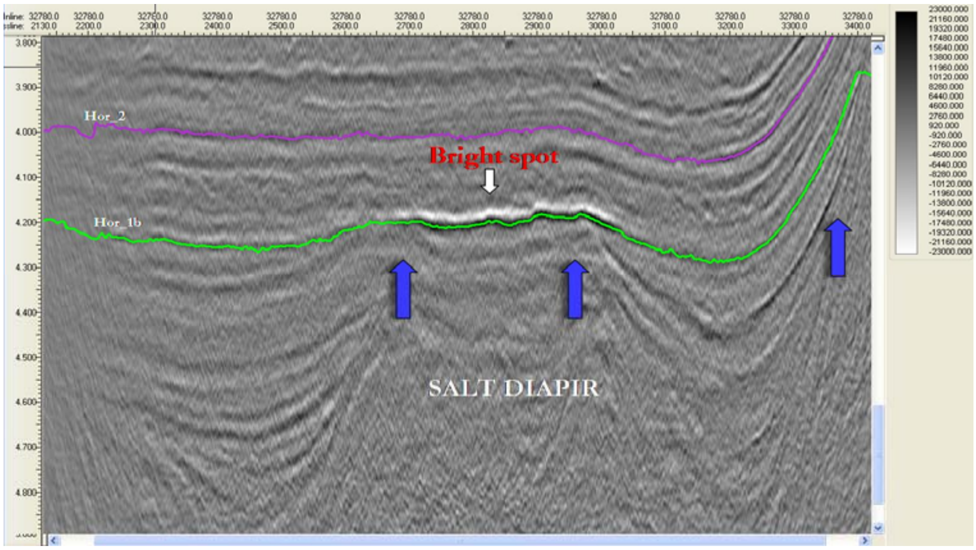

Figure 2.5: Close-up on the near-stacked volume showing bright spot at about 4200 ms.

2.3 Seismic attributes

An attribute literally means a quality, property, or characteristic of somebody or something (Encarta, 2009). Sheriff (2002, p.23) defines a seismic attribute as “a measurement derived from seismic data, usually based on measurements of time, amplitude, frequency and/or attenuation”. He also stated that they may be time-based (related to structure) or amplitude-based (related to stratigraphy and reservoir characterization). To aid my interpretation, I have used the following attributes: time structure, horizon amplitude (RMS), dip, azimuth, and coherence on the picked horizons and time slices (excluding the water bottom).

2.3.1. Time structure and contour

The time-structure map is a plot of the two-way-time of seismic signal to the surface of the horizon. A composite map of the contoured reservoir horizon (hor_1b) superimposed on the time-structure map is shown in figure 2.6. This gives a plan view of the structure of the reservoir horizon, where closely spaced contours indicate steep slopes and large separations of contours indicate gentle slopes. Also, the smaller the value assigned to the contour, the closer the area is to the surface and therefore of higher elevation.

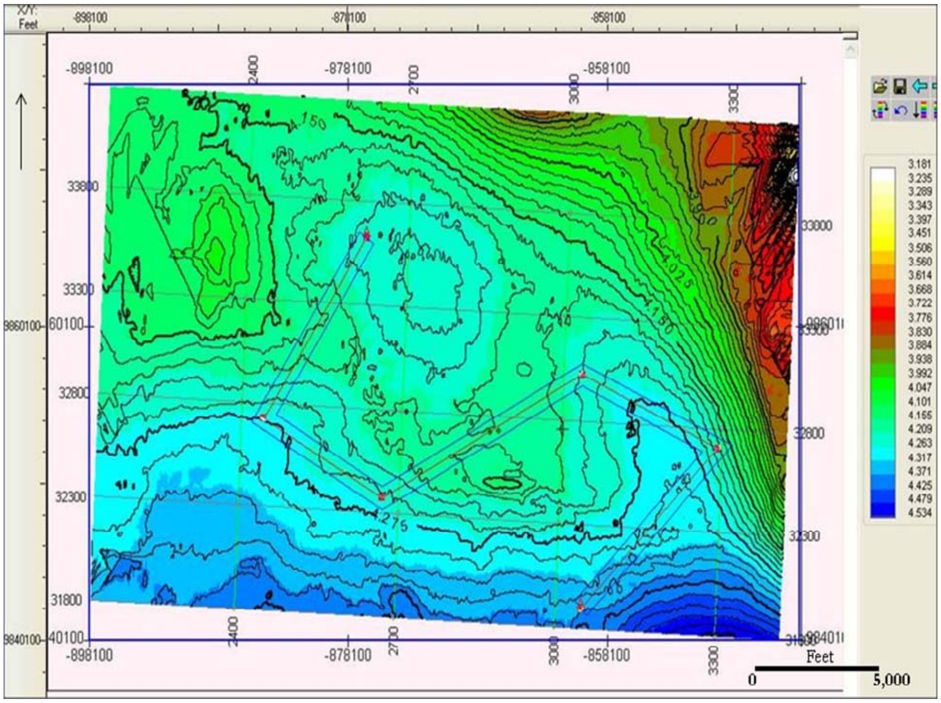

Figure 2.6: Time-structure and contour map of hor_1b through the reservoir sand. Color bar indicates two-way-time from the data-acquisition surface.

2.3.2 Amplitude extraction

Seismic amplitude variation plays a major role in identifying potential hydrocarbon reservoirs and sediment-travel paths from source. Results of amplitudes extraction on the interpreted horizons are as shown in figures 2.7, 2.9 and 2.10 for the near stack, figure 2.11 for the far stack and figure 2.12 for the full stack. Stratigraphic features observed are shown and discussed below.

Erosional grooves which diverge from northeast (NE) to southwest (SW), observed on hor_5 and hor_4 (Figs. 2.7 and 2.9), are indicative of internal deformation characteristic of a sediment flow or slide down the slope (Posamentier and Walker, 2006). On hor_4 however, two distinct groove directions imply two sediment transport/flow directions, NE-SW and NW-SE. This feature characterizes the base of mass-transport deposits (MTDs), described as sediments that have been moved from their original point of deposition which include but are not limited to mass-transport complexes and slumps (Weimer, 1989 in Weimer and Slatt, 2007).

As a result of the absence of grooves and large channels on hor_1b, which is the base of the reservoir sands, these sediments may have been transported purely by turbidity currents in which sediments were maintained in suspension within the fluid (Posamentier and Walker, 2006). Hor_2 and hor_3 also lack grooves and may have also been deposited by turbidity currents. The reservoir horizons (Figs. 2.10, 2.11 and 2.12) show a central bright-spot zone which is known to be oil saturated (Burtz et al., 2002; Cogswell, 2001). In figure 2.10, bright spots are also observed to the north and west of the survey area, which are less visible in the figure 2.11 and 2.12. Sand bodies with high porosities and saturated with hydrocarbon are usually characterized by high amplitude as a result of a decrease in density and velocity. On the other hand, non-hydrocarbon sands, outside the bright spot, show relatively low amplitudes.

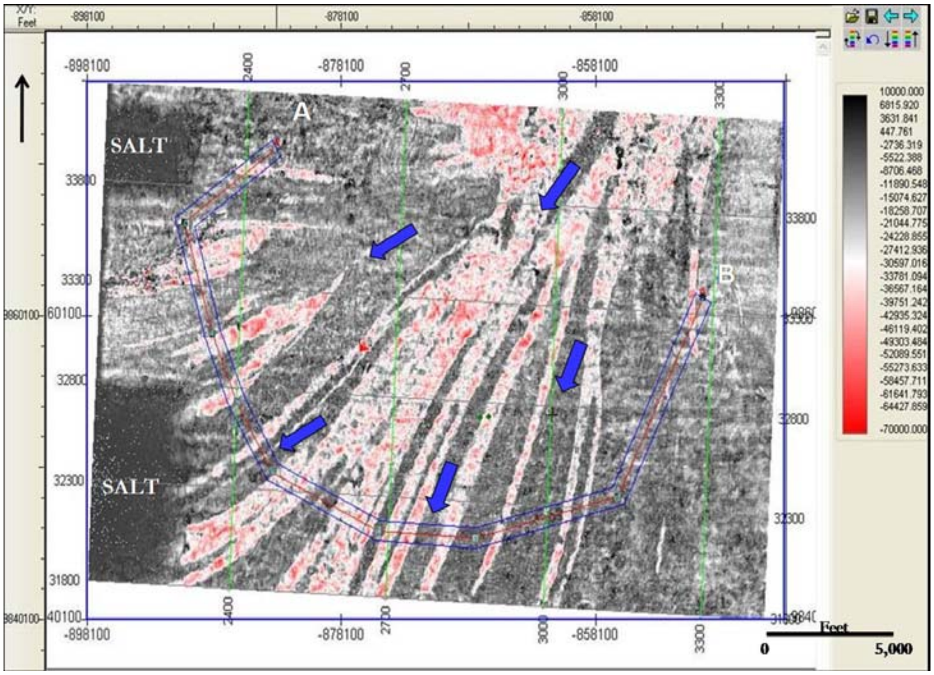

Figure 2.7: Minimum amplitude extraction on hor_5 showing NE-SW erosional grooves. Blue arrows indicate flow direction.

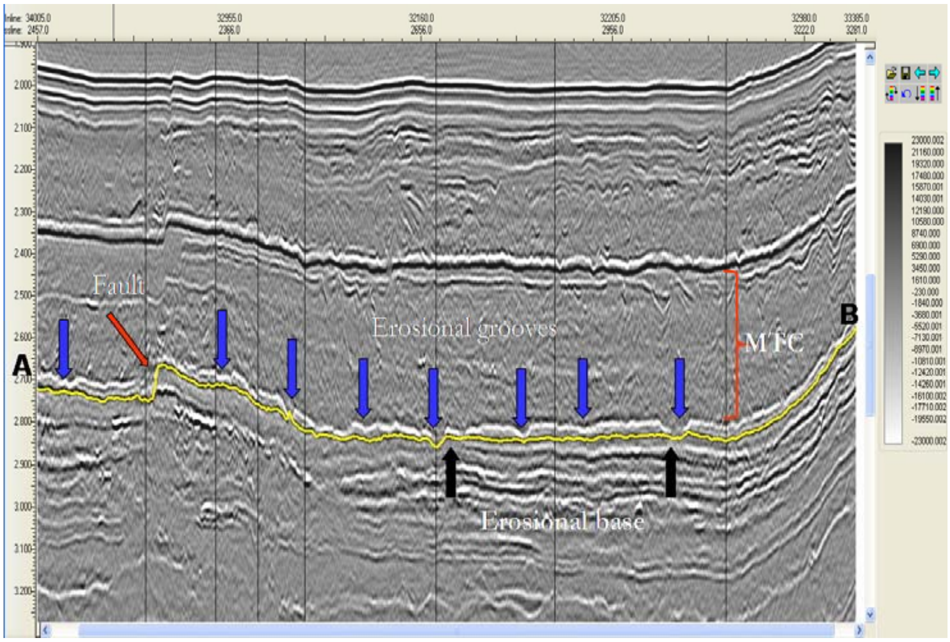

Figure 2.8: Arbitrary line A-B from figure 2.3.2 showing normal fault (red arrow) and erosional groove marks (blue arrows) due to sediment transport.

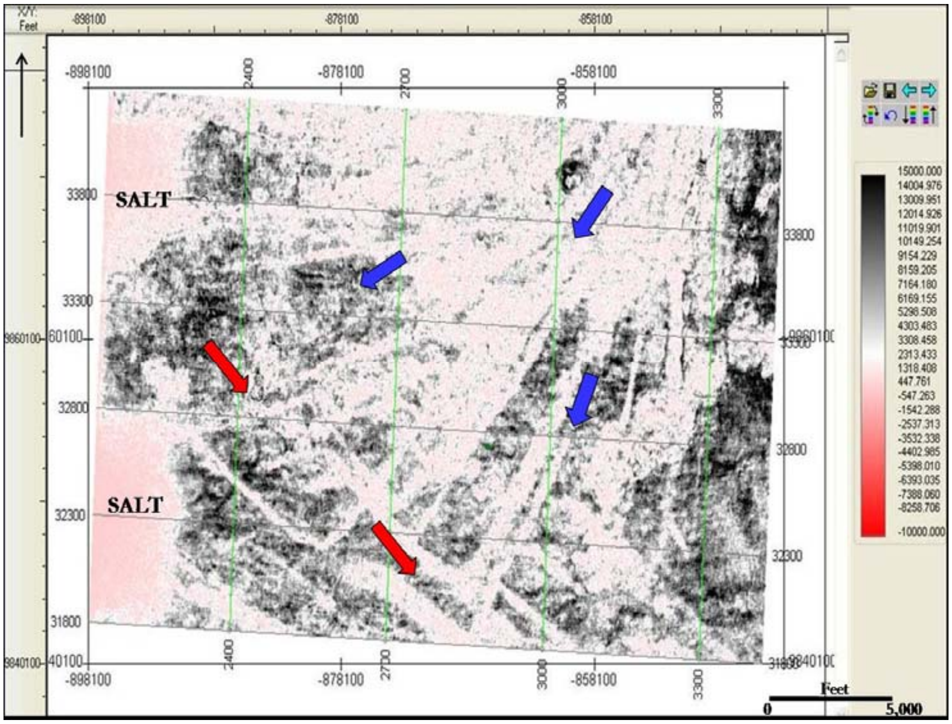

Figure 2.9: RMS amplitude extraction on hor_4 showing NE-SW and NW-SE erosional grooves.

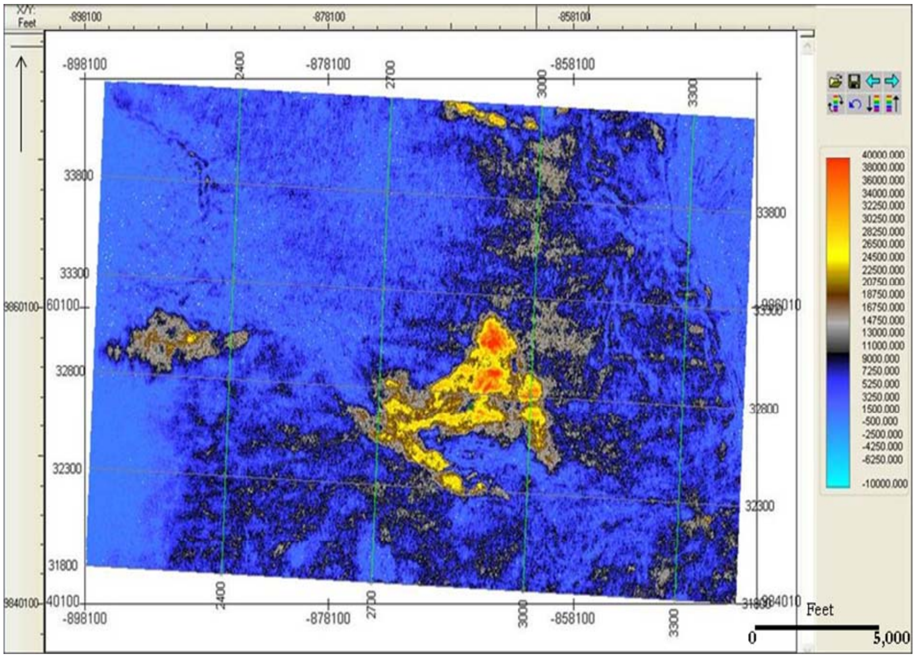

Figure 2.10: RMS amplitude extraction on hor_1b from near-stacked seismic. Note the presence of channels at the NE and absence of grooves.

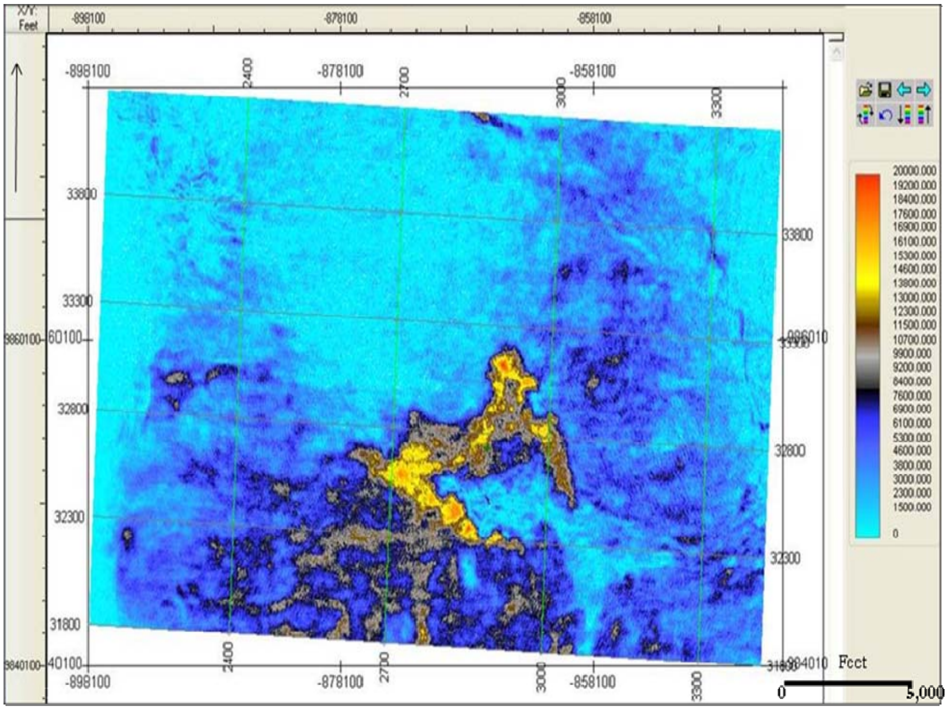

Figure 2.11 RMS amplitude extraction on hor_1b from far-stacked seismic. Note the channels at the NE and absence of grooves.

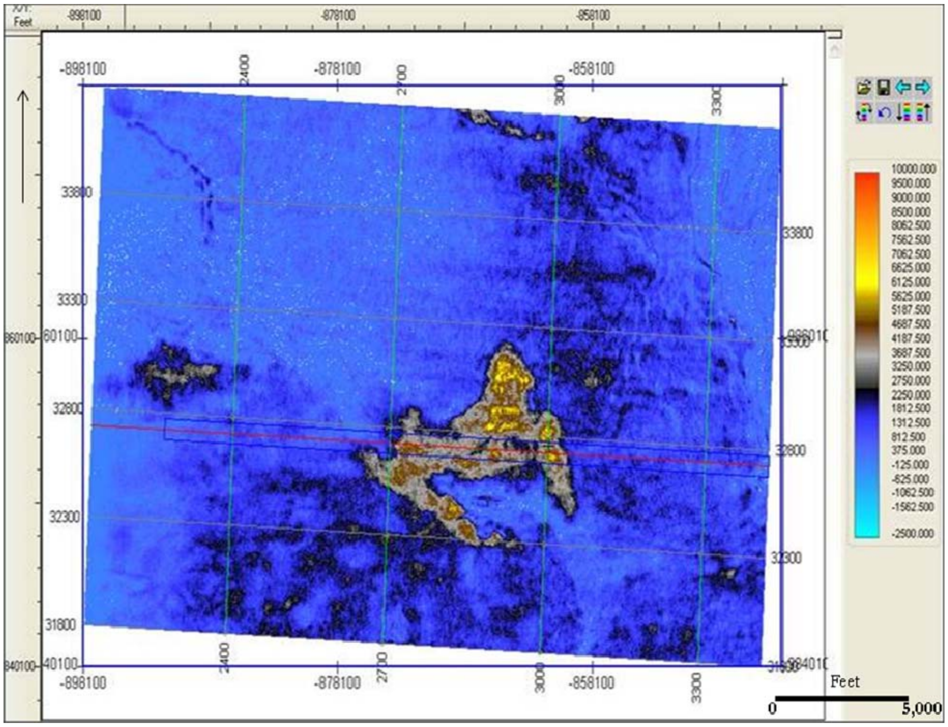

Figure 2.12: RMS amplitude extraction on hor_1b from full-stacked seismic. Note the channels at the NE and absence of grooves.

2.3.3 Dip magnitude and azimuth

Sheriff (2002) described dip as the angle a plane surface, bedding or reflector makes with the horizontal, whereas the azimuth is "the horizontal angle measured clockwise from the true north" (p.29). The dip map (Fig. 2.13) and dip azimuth map (Fig. 2.14) of hor_1b were extracted to further enhance the structural interpretation by identifying structural elements which indicate hydrocarbon-trapping potential.

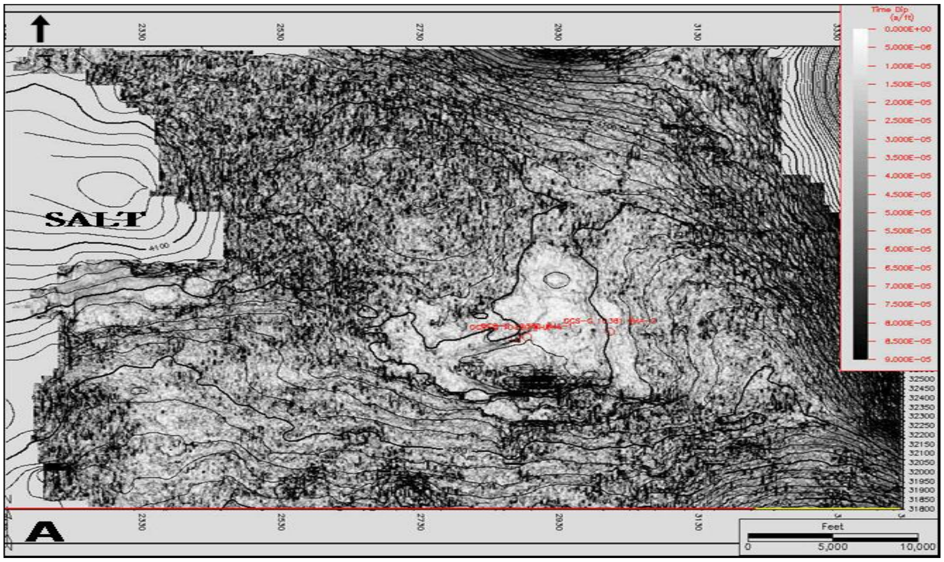

Figure 2.13: Dip magnitude map of hor_1b showing dip direction of the horizon and hydrocarbon-trapping mechanism.

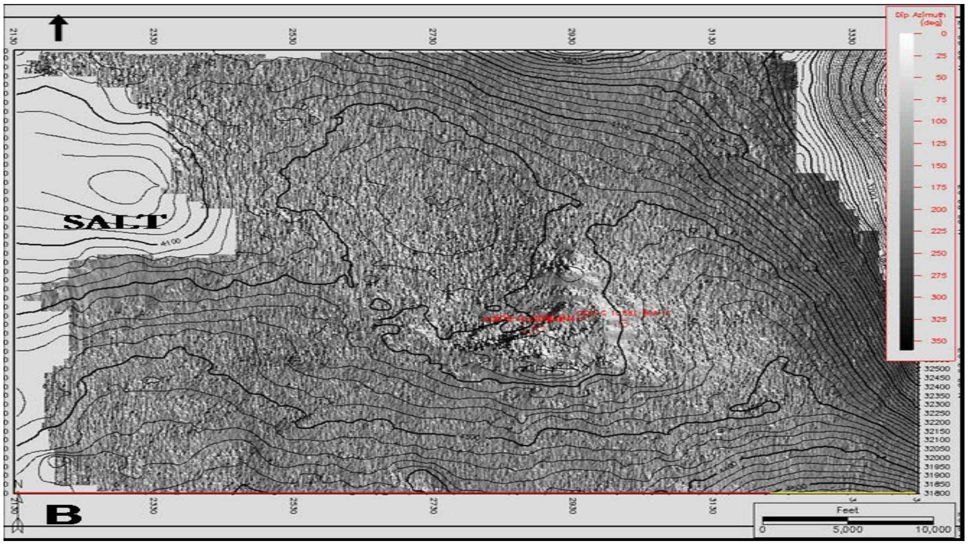

Figure 2.14: Dip azimuth map of hor_1b showing its geometry.

2.4 Time slices

These were also taken to identify features not observed on interpreted horizons, such as seen on figure 2.15 (e.g. deep-water turbidite channels at 2100 ms), and to better understand some features that are observed on horizons, such as the erosional grooves seen on figure 2.16, which had been observed on the interpreted horizons above.

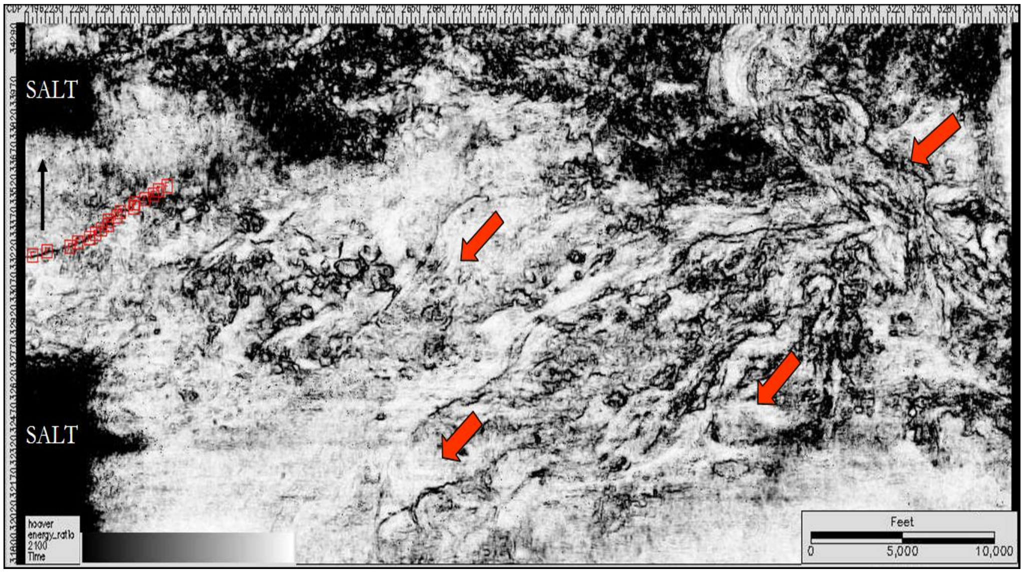

Figure 2.15: Coherence time slice at 2100 ms showing NE-SW-trending deep-water channels.

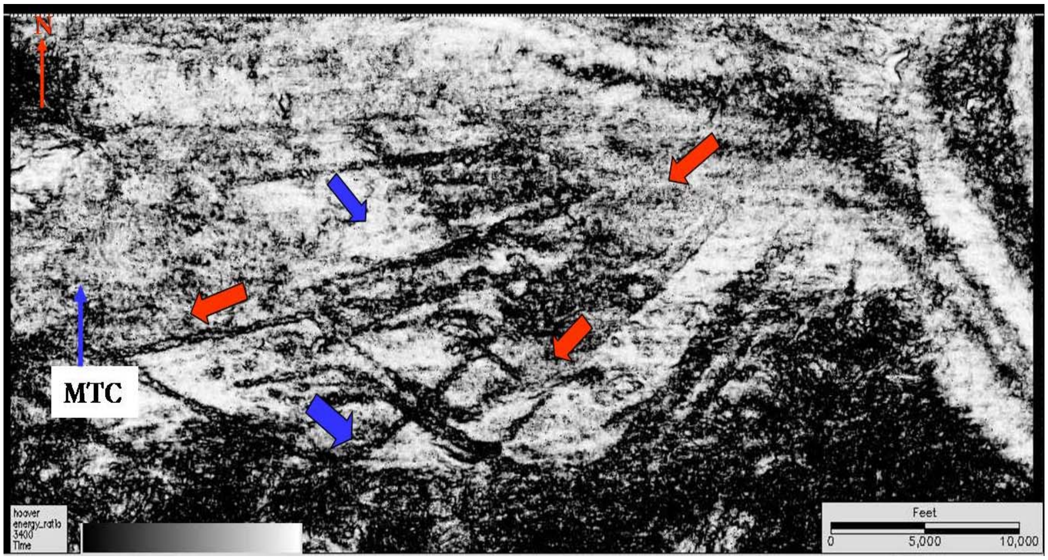

Figure 2.16: Coherence time slice at 3400 ms showing NW-SE- and NE-SW-trending grooves and mass-transport complex.

2.5 Stratigraphic and structural interpretation

Seismic sections and interpreted time and horizon slices, have shown that the Hoover field is characterized by mass-transport complexes (MTCs) and deep-water turbidites. Evidence of MTCs are erosional grooves on hor_4 and hor_5 formed as a result of sediment transport whose dominant interpreted paleotransport direction broadens from NE to SW in the downstream direction indicating a sediment-source point from the NE, as well as their chaotic and structureless internal architecture (Posamentier and Walker, 2006; Weimer and Slatt, 2007). At a point in the depositional history, sediments were also introduced from the NW, as indicated by the erosional grooves cutting across the NE-SW grooves. Posamentier and Walker (2006) stated that grooves which broaden downstream, imply internal deformation characteristic of the flow, rather than slide processes. On the reservoir horizon (hor_1b), grooves are not observed but small channels in the NE are observed. These sediments may have been transported downslope by turbidity currents, probably due to large sediment slumps that accelerate and become turbulent, or due to the delivery of a river flow charged with sediments directly into the slope (Posamentier and Walker, 2006). Weimer and Slatt (2007) stated that in turbidity currents, sediment concentration is low enough such that particles are in suspension. This characteristic therefore results in the absence of grooves.

Horizons above the reservoir show similar structural pattern, with a general dip from N to S (Fig. 2.4) and NE to SW (Fig. 2.7). The central bright spot of the reservoir is slightly elevated by underlying salt body and close to flat-lying, with very gentle dip, characterized by broadly spaced contours (Fig. 2.6). This low-relief anticline, caused by salt diapirism, creates a structural trap. The seismic amplitude anomaly of the reservoir horizon is structurally consistent in that it conforms to the observed trapping structure (Brown, 2006), and shows the probable geometry of the hydrocarbon-water contact. The NE section is bounded by a structurally high area caused by salt withdrawal and upwelling due to sediment loading (Weimer and Slatt, 2007).

2.6 Amplitude analysis

For a quantitative comparison of the full-, near-, and far-stacked volumes amplitudes, they are normalized by a version of the A/B normalization technique described by Hilterman (2001), where A is the anomaly (the reservoir horizon) and B the background amplitude (zones away from the reservoir that are brine saturated). In this analysis, B is taken as the interval RMS amplitudes between two horizons (hor_2 and a second horizon taken 300ms below hor_2). Based on these assumptions, it is observed that the areas away from the bright spot have A/B ratios of between 1 and 3.5 and the bright spots have higher amplitudes ranging between 6.5 and 10 (Fig. 2.17). This answers a question raised by Brown (2004) on whether the amplitude anomaly is large relative to the background. The amplitude anomaly shows an apparent Class 4 response (Castagna et al., 1998), i.e. a bright amplitude which decreases with offset.

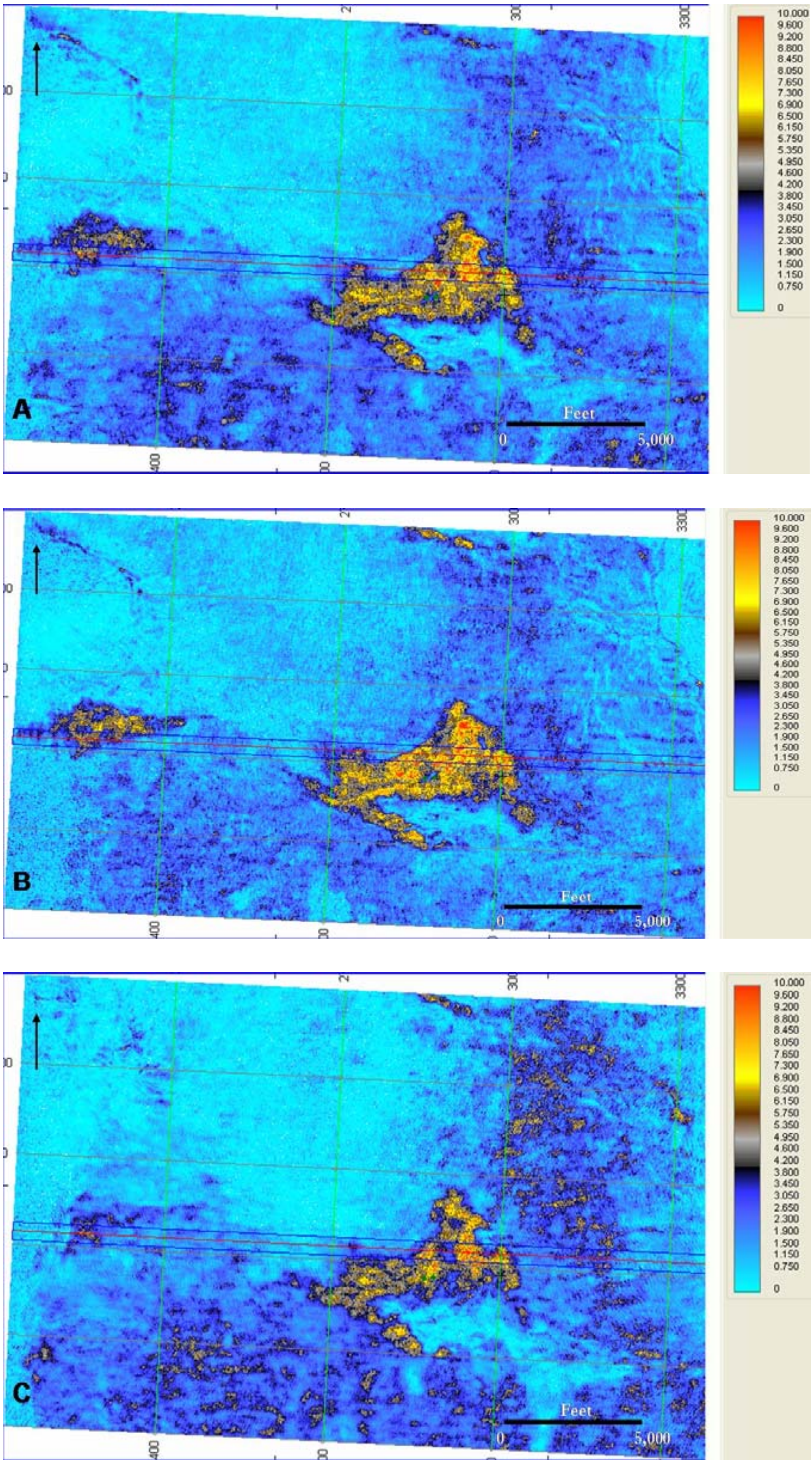

Figure 2.17: A/B amplitude ratio for full- (A), near- (B) and far- (C) stacks.

Chapter 3: AVO analysis from well logs

3.1 Seismic to log correlation

3.1.1 Introduction

Correlation is basically a measure of the similarity between a pair of traces. This involves aligning the synthetic seismic generated from logs with seismic trace(s) near the well location. In this research, correlation is carried out for near- and far-stacked seismic data with logs in wells HA-1 and HA-4 using Hampson-Russell's AVO and Kingdom's SynPAK. However, there are no deviation surveys to correct measured depths to true vertical depth. Two methods of wavelet extraction from the seismic are used. The first involves the extraction of wavelet after correlation, which represents the phase of the seismic and may not be zero phase. The second involves the calibration of the seismic to zero phase after correlation and subsequent extraction of a zero or close to zero-phase wavelet.

3.1.2 Synthetic seismogram generation (Forward modeling)

The correlation process begins with the convolution of reflectivity, r(t) derived from density, P-wave velocity, and S-wave velocity logs with a zero-phase wavelet, w(t) extracted from the seismic at the well location (Fig. 3.1) to generate a synthetic seismic, s(t) which is correlated with each stacked section.

$$s(t) = w(t) * r(t) \qquad (1)$$

Some assumptions involved in the generation of the synthetic include: the geologic dip is zero, the well bore is vertical, log readings are accurate, and velocity only varies with depth (Liner, 2004). Initial zero-phase wavelet-extraction parameters from the near-stacked seismic volume are as shown in table 3.1, while wavelet properties (frequency spectrum, dominant frequency, and phase) are as shown in figure 3.1.

Parameters	Near-stacked seismic volumes	
	Well 1	Well 4
Time window	3200 – 4200 ms	3200 – 4200 ms
Xline range	2858 - 2871	2874 - 2889
Inline range	32730	32720
Wavelet length	200 ms	
Taper length	25	
Phase rotation	0	
Phase type	Constant phase	

Table 3.1: Zero-phase wavelet-extraction parameters for near-stacked seismic.

Near-angle-stacked seismic correlation requires S-wave logs to generate offset synthetics with the use of the Zoeppritz equations. Because no S-wave logs are available, they are created for both wells using Castagna's equation (2), which is valid only for wet background rock.

$$V_s = 0.8619V_p + (-3845) \qquad \text{in ft/s} \qquad (2)$$

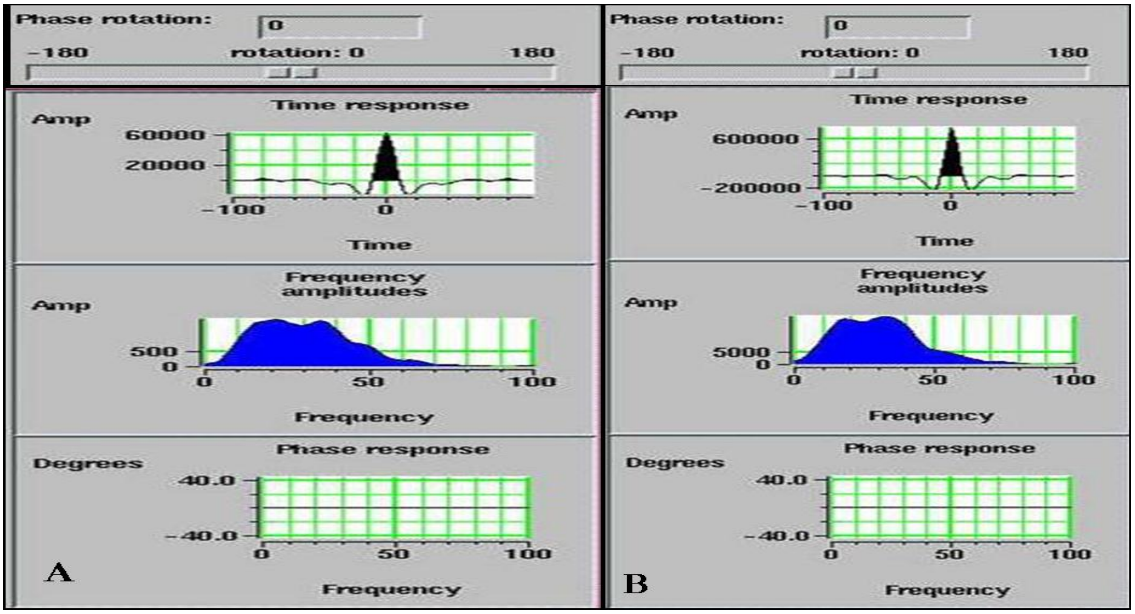

Figure 3.1: Zero-phase wavelet extracted from near-stacked seismic around well HA-1 (A) and HA-4 (B) showing time response, frequency content, and phase of wavelet.

3.1.3 Correlation, wavelet extraction and phase determination for model-based and sparse-spike inversions

Correlation is carried out with a composite trace (blue trace), which is an average of adjacent traces around the well location (Fig. 3.2). This is achieved by first carrying out a time shift to match the main event(s), where events do not match, and subsequent manual stretching and/or squeezing to fit major events on the synthetic with the seismic. Where correlation shows an asymmetric shape, as observed in figure 3.2, it indicates that the seismic is not zero phase. For this reason, one extracts a new wavelet using the wells and seismic data near the well in order to get the phase of the seismic (Russell, 2005). This wavelet is assumed to be constant in time and space. An improved correlation is observed after wavelet from the well is extracted and used in correlation (Fig. 3.3). The same process is repeated for well HA-4. The correlation, extracted wavelets and cross-correlation displays are as shown in figures 3.4 and 3.5.

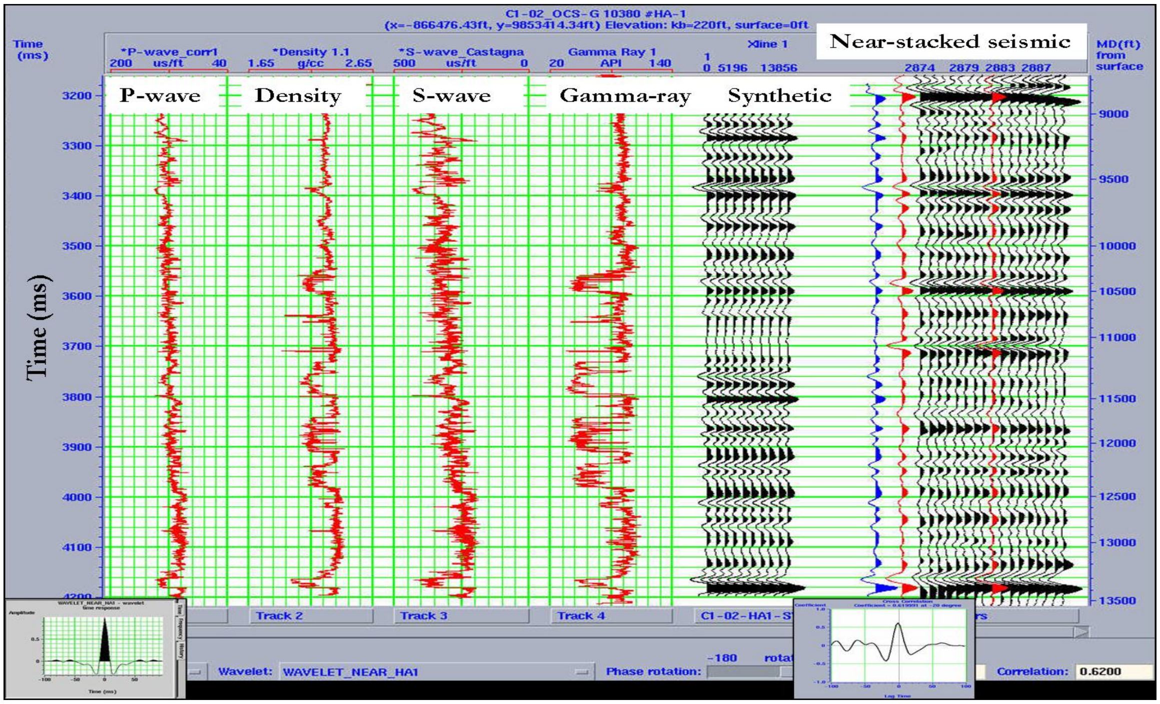

Figure 3.2: Correlation of near-stacked seismic with well HA-1 using wavelet from seismic. Inset: bottom left (zero-phase wavelet from seismic), bottom right (cross-correlation of seismic and synthetic, 0.62).

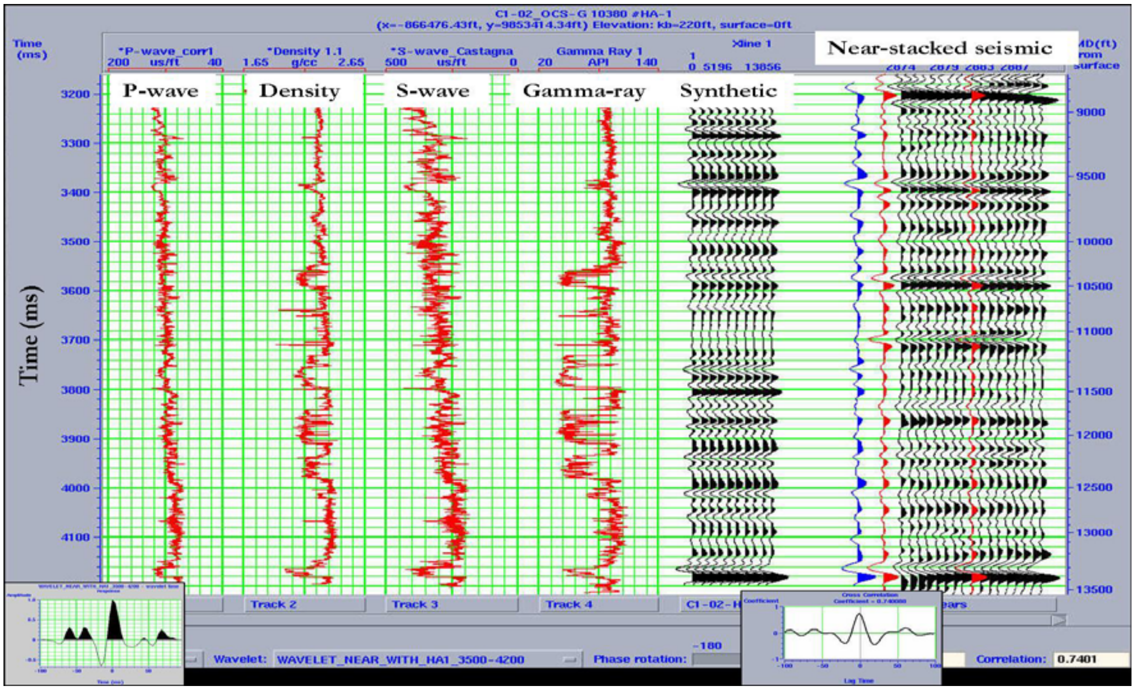

Figure 3.3.: Correlation of near-stacked seismic with well HA-1 using wavelet from well. Inset: Bottom left (non-zero-phase wavelet from well), bottom right (cross-correlation of seismic and synthetic, 0.7401).

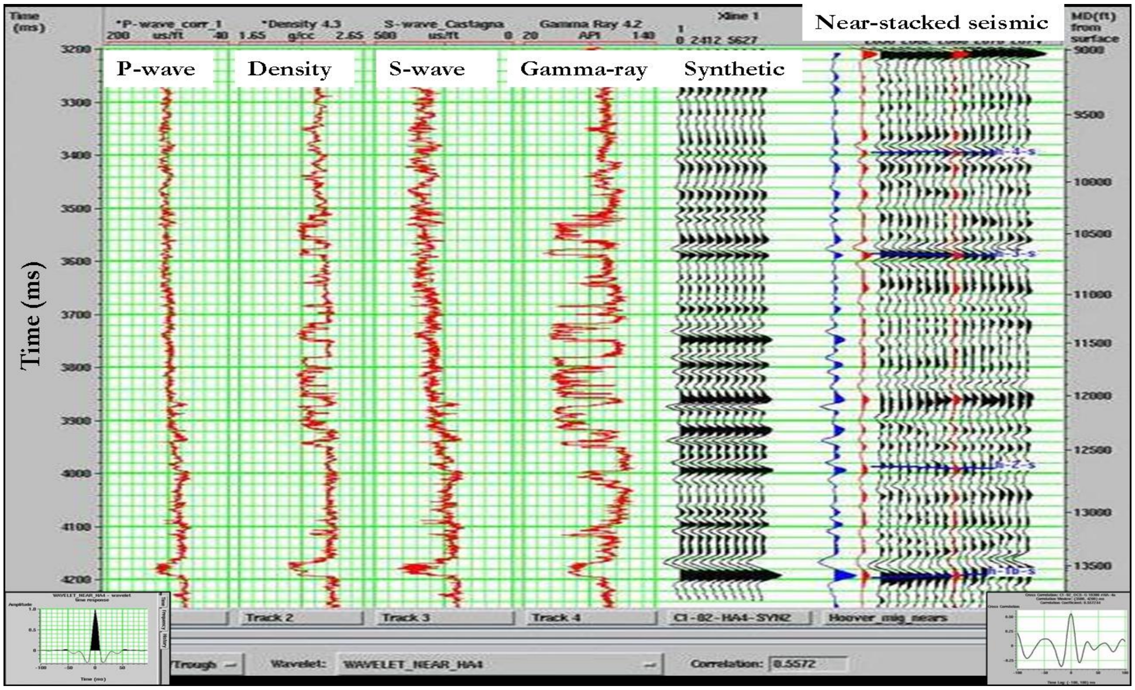

Figure 3.4: Correlation of near-stacked seismic with well HA-4 using wavelet from seismic. Inset: Bottom left (zero-phase wavelet from seismic), bottom right (cross-correlation of seismic and synthetic, 0.5572).

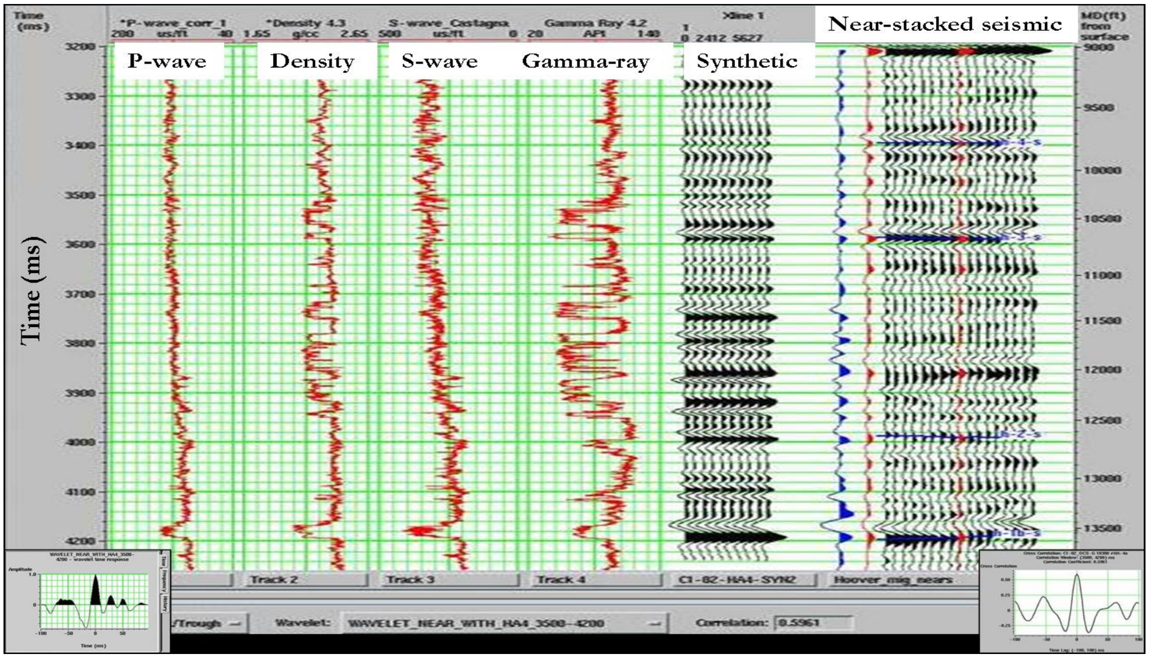

Figure 3.5: Correlation of near-stacked seismic with well HA-4 using wavelet from well. Inset: Bottom left (non-zero-phase wavelet from well), bottom right (cross-correlation of seismic and synthetic, 0.5961).

Because one needs a single wavelet to carry out inversion, an average wavelet is extracted from wells HA-1 and HA-4 after correlation with near-stacked seismic volumes (Fig. 3.6.) The resulting wavelet has smaller side lobes than the individual wavelets and also has a spike at the center. Multi-well analysis carried out to determine the quality of the ties using the average wavelet shows an average correlation coefficient of 0.63 (Fig. 3.6).

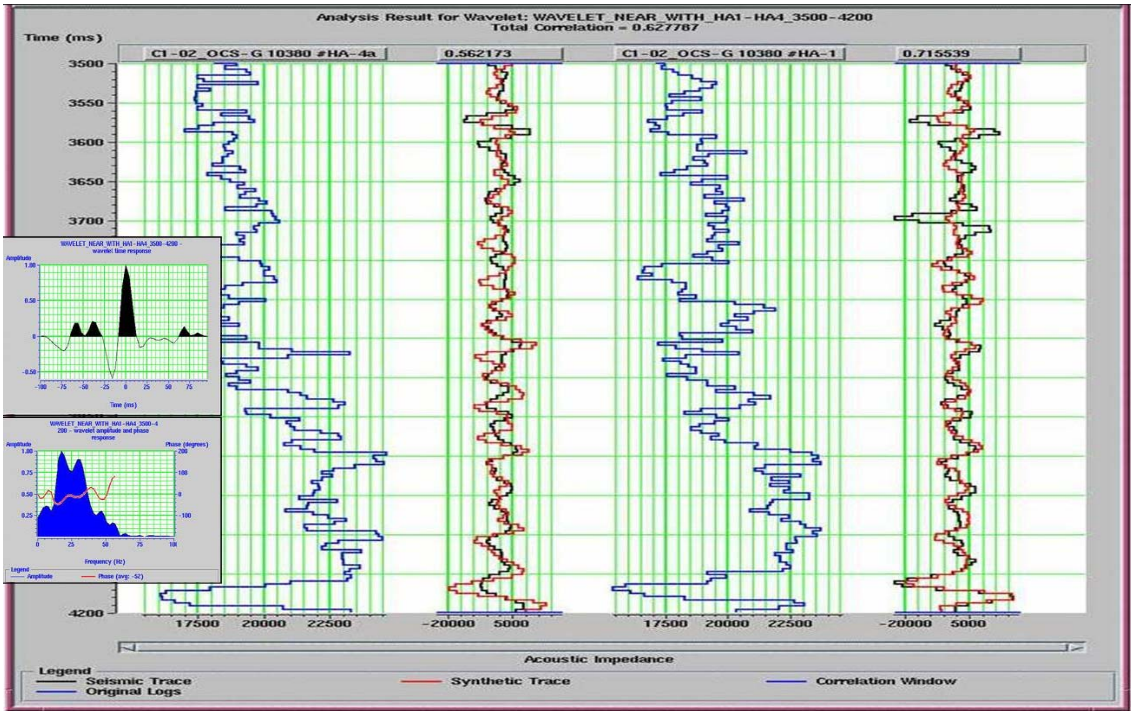

Figure 3.6: Multi-well analysis for near-stacked seismic with average wavelet extracted from both wells. Top left (non-zero-phase wavelet from both wells), bottom left (phase of the new wavelet, -52^0).

3.1.4 Correlation and phase calibration of seismic for high-resolution band-limited impedance inversion

This band-limited inversion method requires the calibration of seismic data to zero phase, and this is carried out for the near- and far-stacked seismic using logs in Kingdom's SynPAK. Calibration results for the near stack are as shown in figures 3.7, 3.8 and 3.9. This involves correlation and phase rotation of zero-phase synthetic to the phase of the seismic data (Fig. 3.8), after which the same amount of phase rotation but with opposite sign is applied to the seismic volume. In this case plus 44^0 and 32^0 phase rotation is applied respectively on the near- and far-stacked seismics. The zero-phase wavelet is preferred because its strong peak minimizes side lobes and it produces good vertical resolution, as it is symmetrical with its peak amplitude located at the center of the wavelet (Liner, 2004). Correlation results with wavelet extracted after initial correlation and location of the two wells on the near-stacked seismic are shown in figures 3.9, and 3.10. The same calibration process is applied to the far-stacked seismic and results are shown in figures 3.11 and 3.12.

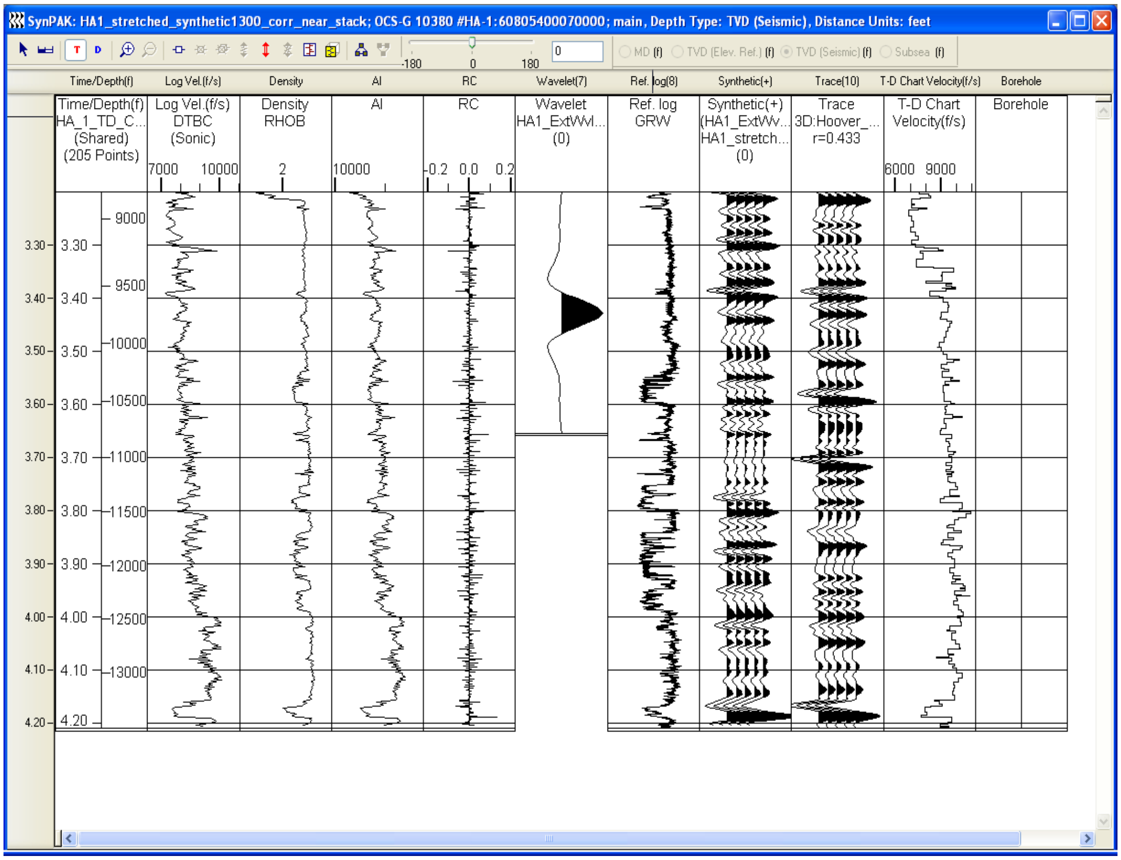

Figure 3.7: Correlation of synthetic from well HA-1 and near-stacked seismic data with zero-phase wavelet.

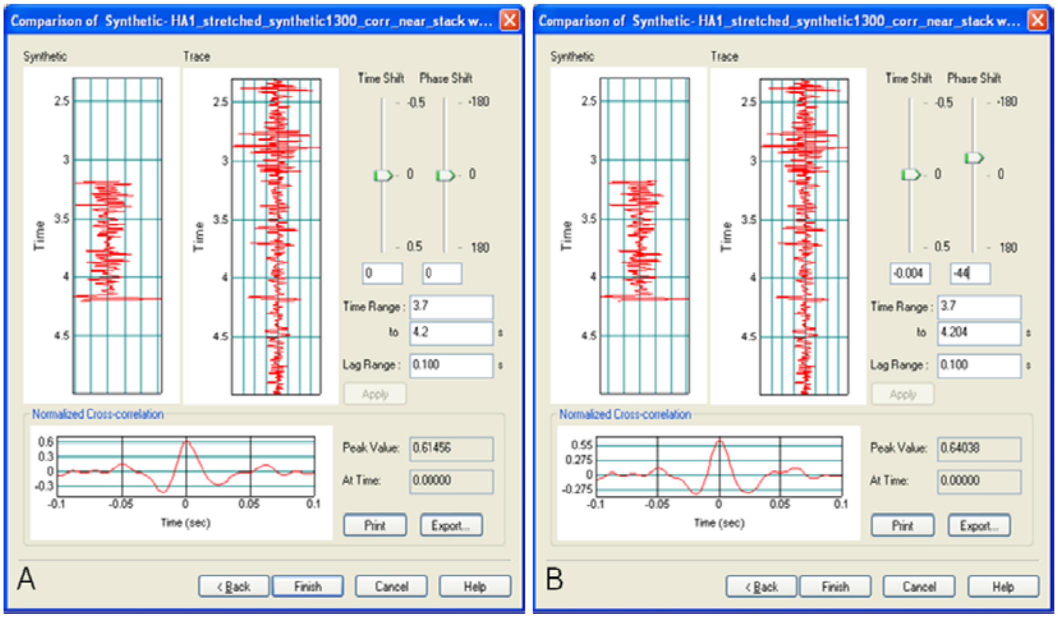
Comparison of Synthetic- HA1_stretched_synthetic1300_corr_near_stack w...

A: Time Shift: 0; Phase Shift: 0; Time Range: 3.7 to 4.2 s; Lag Range: 0.100 s; Peak Value: 0.61456; At Time: 0.00000

B: Time Shift: -0.004; Phase Shift: -44; Time Range: 3.7 to 4.204 s; Lag Range: 0.100 s; Peak Value: 0.64038; At Time: 0.00000

Figure 3.8: Phase calibration of seismic, showing correlation and phase before (A) and after (B) phase calibration for a 3.7 s and 4.27 s window.

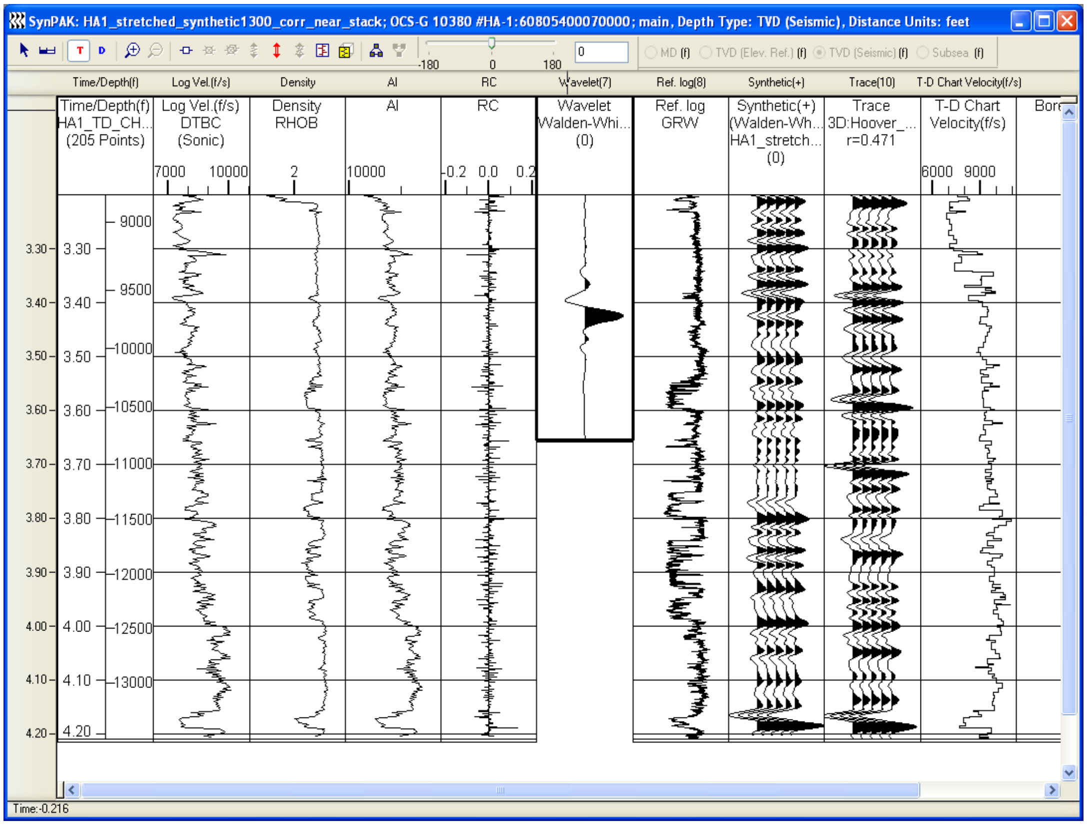
SynPAK: HA1_stretched_synthetic1300_corr_near_stack; OCS-G 10380 #HA-1:60805400070000; main, Depth Type: TVD (Seismic), Distance Units: feet

Figure 3.9: Correlation of synthetic from well HA-1 and near-stacked seismic data with wavelet extracted from seismic after correlation.

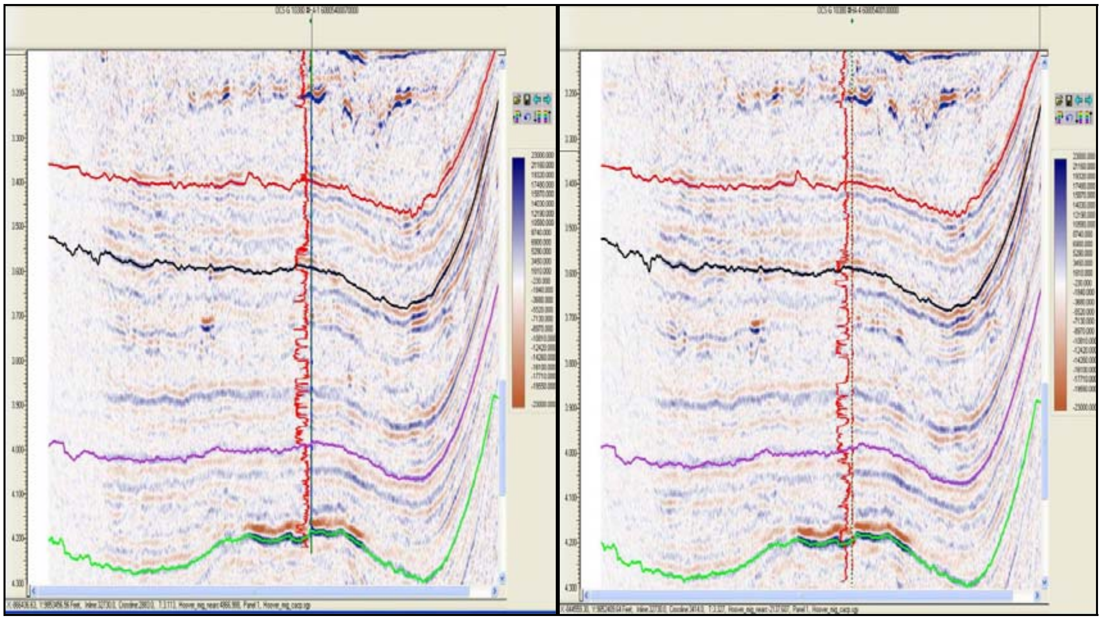

Figure 3.10: Near-stacked seismic with wells HA-1 and HA-4, showing gamma-ray logs.

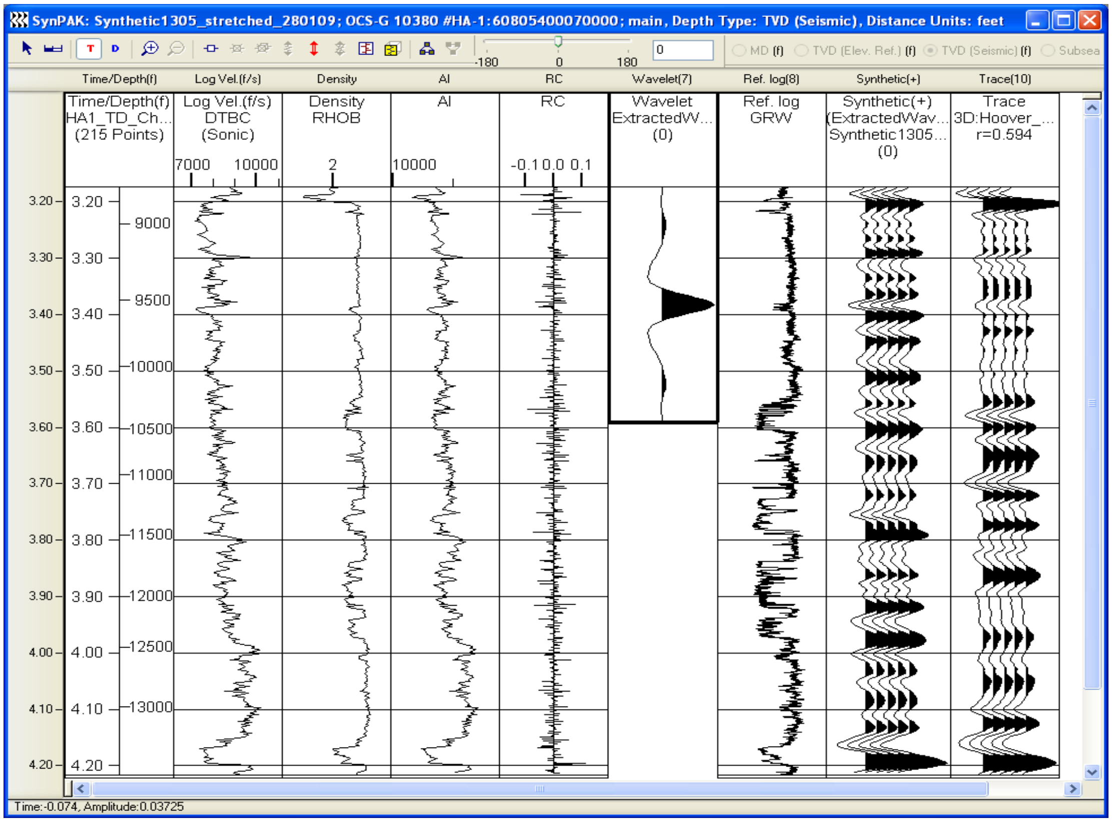

Figure 3.11: Correlation of synthetic from well HA-1 and far-stacked seismic data with zero-phase wavelet (3.2 s to 4.27 s).

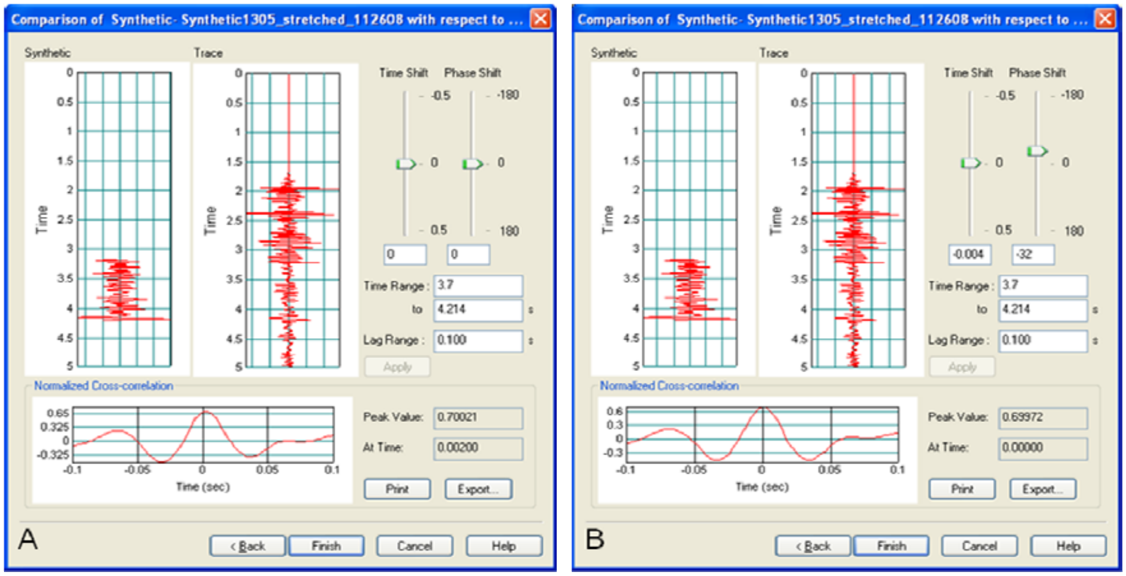
Comparison of Synthetic- Synthetic1305_stretched_112608 with respect to ...

Time Shift: 0
Phase Shift: 0
Time Range: 3.7 to 4.214 s
Lag Range: 0.100 s
Peak Value: 0.70021
At Time: 0.00200

Comparison of Synthetic- Synthetic1305_stretched_112608 with respect to ...

Time Shift: -0.004
Phase Shift: -32
Time Range: 3.7 to 4.214 s
Lag Range: 0.100 s
Peak Value: 0.69972
At Time: 0.00000

Figure 3.12: Phase calibration of seismic using well HA-1, showing correlation and phase before (A) and after (B) phase calibration for a 3.7 s to 4.27 s window.

In the course of carrying out the correlation exercises, one would notice that synthetic seismograms do not perfectly match the seismic data. Some of the reasons for this were enumerated by Liner, (2004). They include: frequency differences between log (high frequency, kHz) and seismic (low frequency); borehole problems such as wash outs which affects sonic logs; wavelet estimation problems; noise and data processing; and transmission loss, geometric spreading, and frequency-dependent absorption are ignored.

3.2 Well log interpretation

This section focuses on the interpretation of well logs for the intrinsic and induced properties of the rocks and their pore fluids. Two wells, HA-1 (Figs. 3.13 and 3.14) and HA-4 (Figs. 3.15 and 3.16) containing gamma-ray, density, resistivity, P-wave sonic, caliper, and neutron logs used in this research are described in subsequent pages.

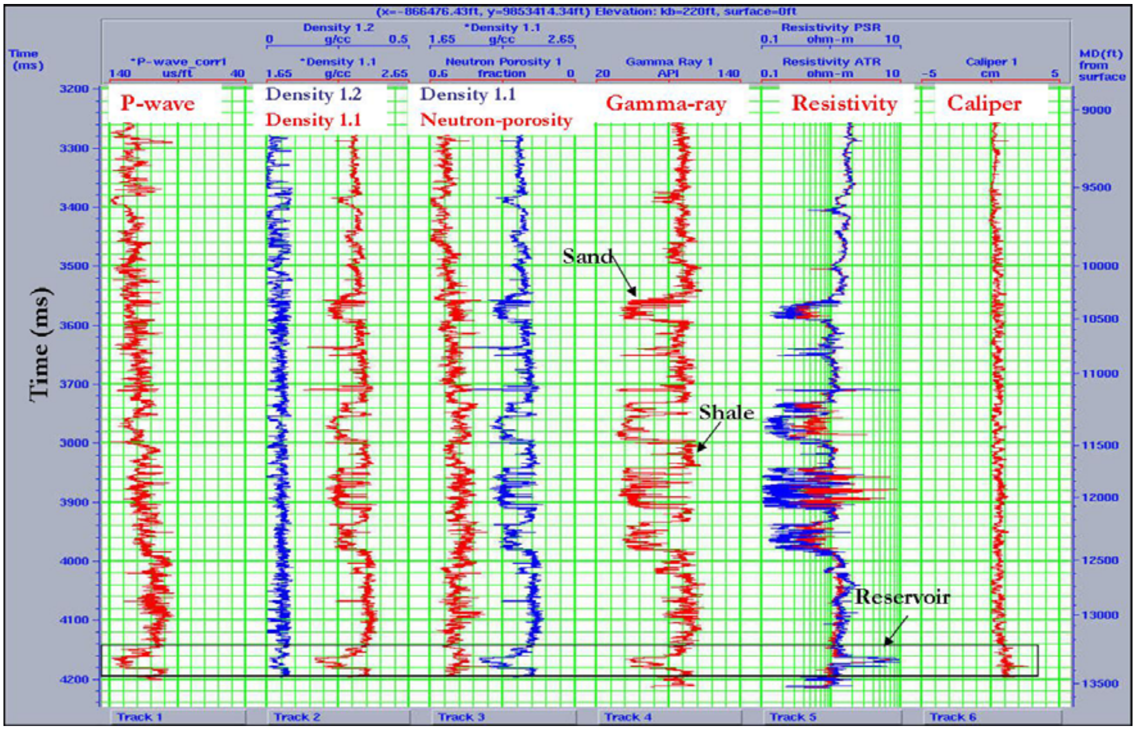

Figure 3.13: Well HA-1 logs

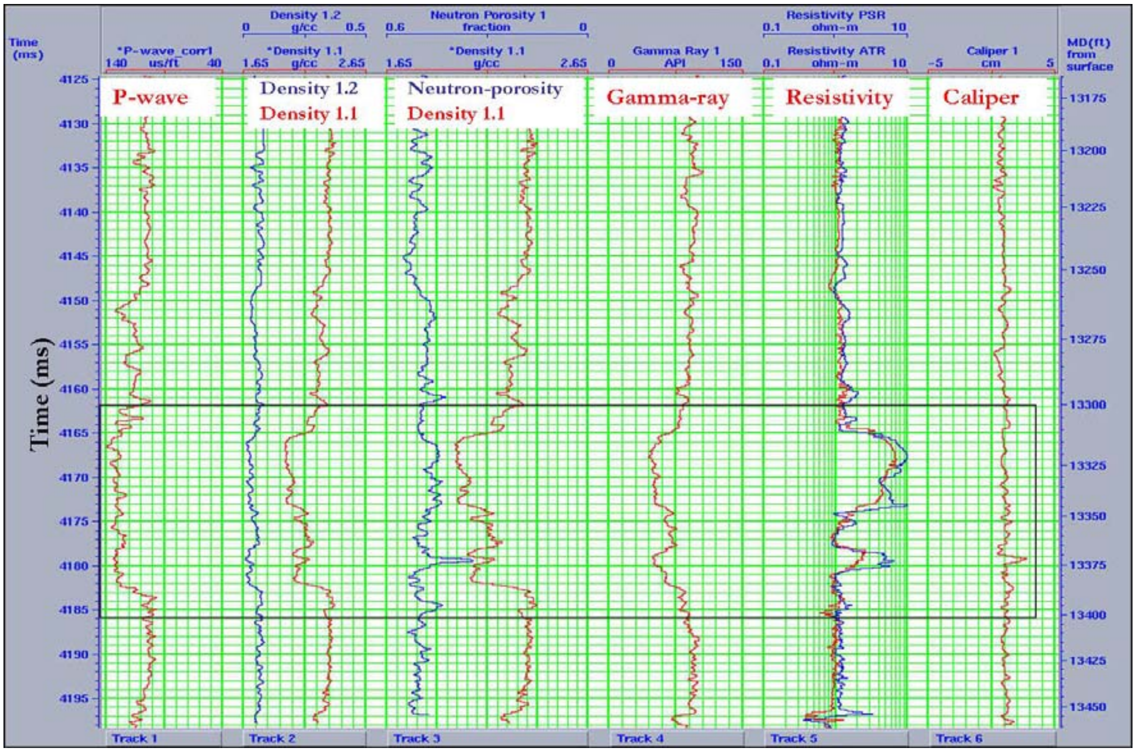

Figure 3.14: Close-up section of Well HA-1 logs showing the reservoir interval (in black box).

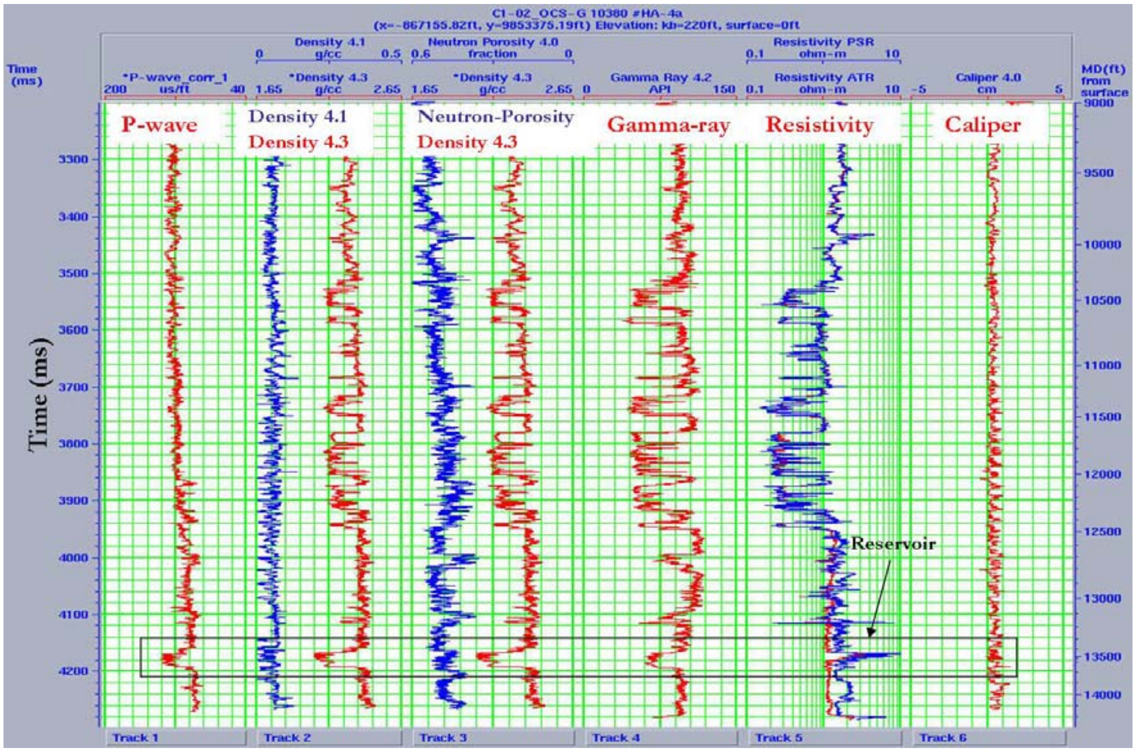

Figure 3.15: Well HA-4 log curves

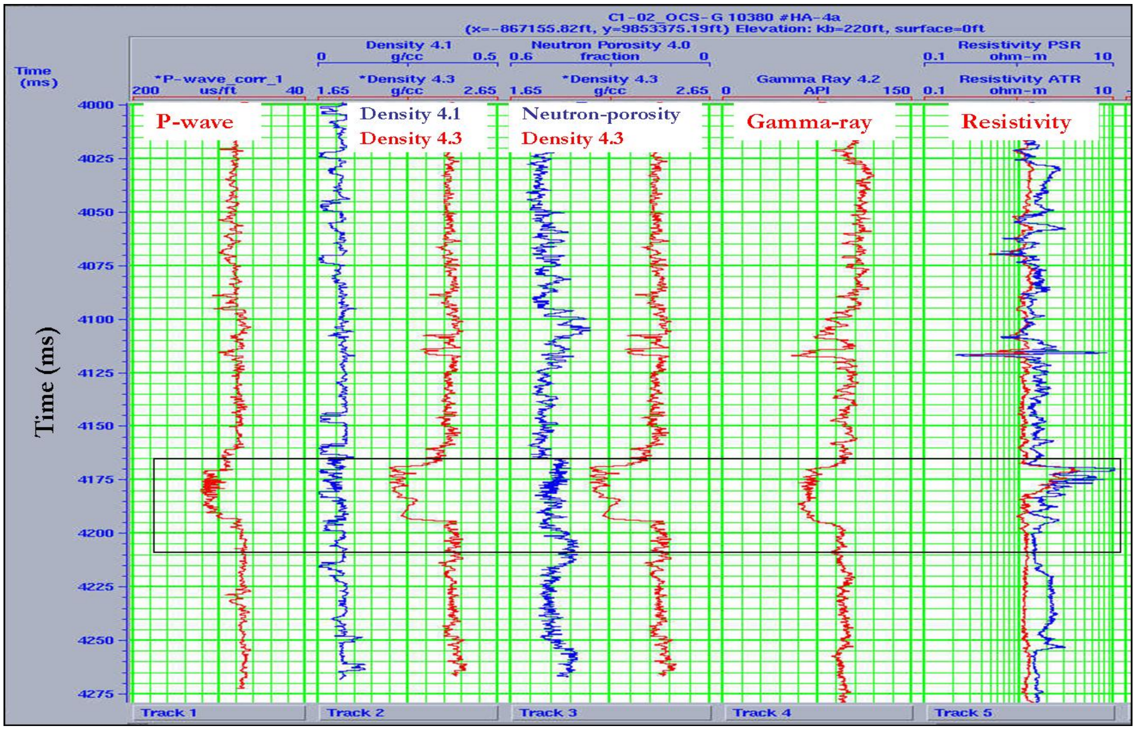

Figure 3.16: Close-up section of Well HA-4 showing the reservoir interval (in black box).

3.2.1 Gamma-ray log

The gamma-ray log measures the natural radioactivity of the formations (Gluyas and Swarbrick, 2004). Although shale-free sandstones and carbonates have low radioactivity, high values may be observed in clean sandstone if it contains potassium feldspars, micas, glauconite, or uranium-rich waters (Asquith and Krygowski, 2004). Both wells consist of sandstones (deflection to the left) and shales (deflection to the right) (Figs. 3.13 to 3.16).

Log pattern(s) can be used in interpreting grain-size variations and depositional environments of the reservoir, (Gluyas and Swarbrick, 2004). The log pattern in HA-1 varies from blocky to fining upwards between 3500 ms and 3600 ms, to blocky (with serrated surfaces produced by shale interbeds) between 3700 ms to 4000 ms, which may be amalgamated channels with sharp lower and upper contacts. At the reservoir between 4160 ms and 4190 ms, the sand unit coarsens upwards. Well HA-4, on the other hand, is characterized by a blocky gamma ray pattern at the reservoir, characteristic of turbidites. Other sand units above the reservoir are characterized by sharp bottom and top contacts. The reservoir is about 77 ft (≈23 m) thick.

3.2.2 Density log

Asquith and Krygowski (2004) described the density log as a record of the formation bulk density (RhoB) in g/cc; it is dependent on the matrix, porosity of the rock, and density of the fluid in the pores. Well HA-1 records a high density of about 2.4 g/cc in shale unit at 4144 ms and decreases to about 2.02 g/cc in the sand reservoir at 4174 ms. In well HA-4, similar variation is observed. Although all sand units have low densities, the reservoir records the lowest densities, probably caused by the presence of hydrocarbons (Fig. 3.17).

The density-correction curve, DRho (labeled density 1.2 and 4.1), indicates the amount of correction that has been added to the density log during processing due to borehole effects (Asquith and Krygowski, 2004). They advised that where the correction curve exceeds 0.20 g/cc, the density log reading should be considered suspect and possibly invalid. In both wells, density correction values are below 0.2 g/cc.

3.2.3 Neutron log

The neutron log measures hydrogen atom concentration present in formation pores (Gluyas and Swarbrick, 2004; Slatt, R.M., 2006). Asquith and Krygowski (2004) stated that a low hydrogen density indicates low liquid-filled porosity. They also added that when pores are filled with gas rather than oil or water, the reported neutron porosity is less (i.e. gas effect) than the actual formation porosity as a result of the lower concentration of hydrogen in gas compared to oil or water. Brine- and oil-saturated sands in both wells record about the same amount of neutron porosity as shown in figures 3.13 to 3.16 and 3.18, making it a poor discriminating property.

3.2.4 P-wave sonic log

The P-wave sonic log measures the transit time (Δt in μs/ft) of an acoustic waveform between a transmitter and a receiver (Veeken, 2007). Both logs show a general increase in velocity with depth, with a sudden decrease in the reservoir (Figs. 3.13 to 3.16). P-wave velocity in the overlying shale ranges between 2854 m/s (9365 ft/s) and 2943 m/s (9655 ft/s), however it drops to below 2377 m/s (7,800 ft/s) in the reservoir, probably due to the presence of hydrocarbons before increasing above 2957 m/s (9,700 ft/s) in the underlying shales.

3.2.5 Resistivity log

Resistivity is "the property of a material that resists the flow of an electric current" (Sheriff, 2002, p.298). A brine-saturated rock is expected to have a lower resistivity than hydrocarbon-saturated rock, as it is more conductive. Resistivity logs available in the survey area include phase-shift-derived resistivity (PSR) and attenuation-derived resistivity (ATR). The PSR log is equivalent to the spherically focused resistivity log on the wireline induction tool with average depth of investigation of 75 cm whereas ATR is equivalent to the dual induction-medium measurement with an average depth of investigation of 125 cm (Moore, et al., 1998). In this research, they would be considered as "deep" for ATR and "shallow" for PSR, although in the true sense of the word they are not. Drilling fluids used in HA-1 and HA-4 are sea water and polymer respectively. Although both wells have a pay zone with higher resistivity than the surrounding formations, this is relatively low for an oil reservoir, as it is less than 10 ohm-m. In HA-1, resistivity increases over 100 % from 1.19 ohm-m at about 4155 ms in the shale water-saturated unit, to approximately 3.5 ohm-m at about 4161ms in the sandstone reservoir with hydrocarbon. This decreases slowly towards the bottom of the reservoir with a value of 1.1 ohm-m at 4186 ms at the bottom of the reservoir. Similar readings are obtained in HA-4. At the reservoir, there is little separation between both logs. Where there is a separation as observed in the sand units above the reservoir in HA-1, it is as a result of invasion.

Some potential causes of low-resistivity reservoirs have been discussed by Hamada et al. (2000) and Boyd, et al. (1995). These include: microporosity, conductive minerals (clay minerals, metal sulfides, graphite and pyrites), and high level of irreducible water saturation.

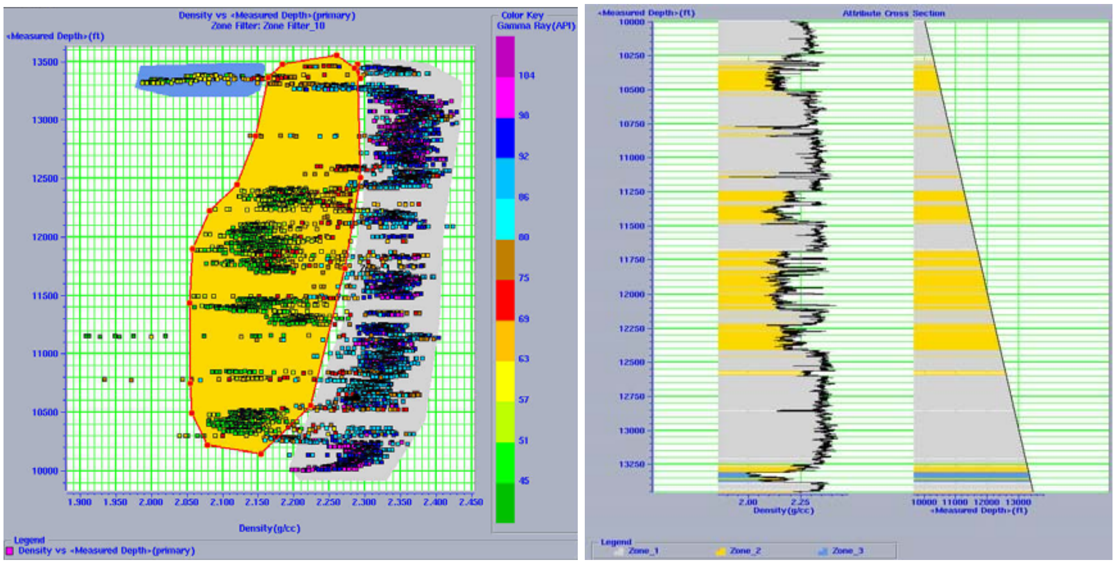

Figures 3.17: Crossplot (left) and cross-section (right) display of density against measured depth showing oil-saturated reservoir sands (least density, blue), non-reservoir sands (intermediate density, yellow), and shales (highest density, grey).

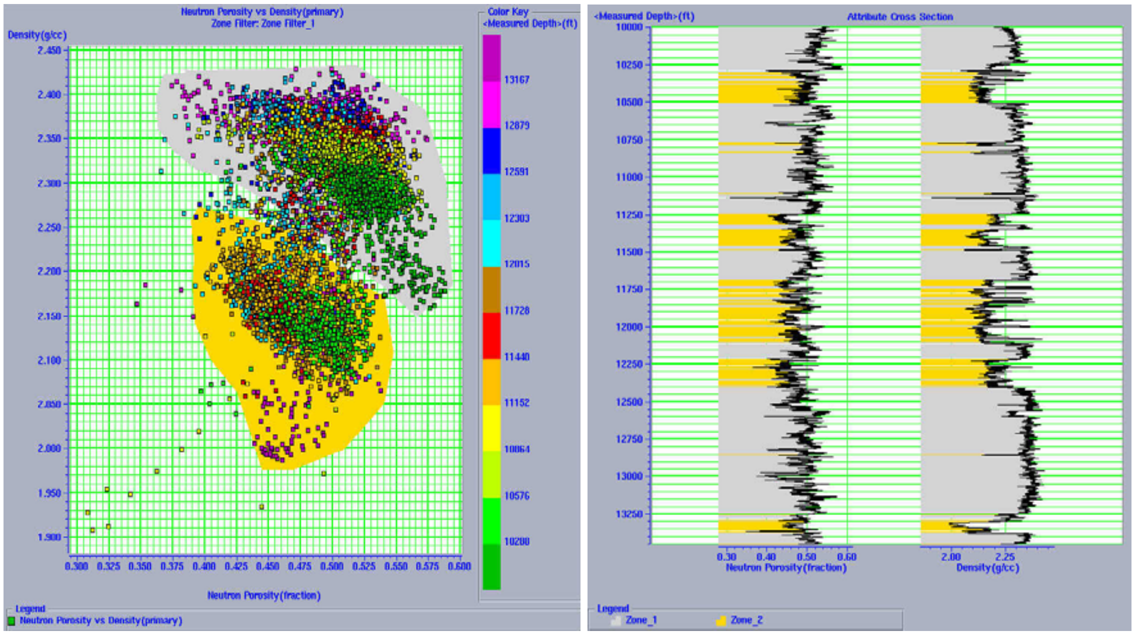

Figures 3.18: Crossplot (left) and cross-section (right) display of density against neutron porosity, showing sand (yellow), and shale (grey) units.

3.2.6 Density porosity (Φ)

This is the amount of pore or void spaces found in a rock which determines its capacity to store or hold fluids (Gluyas and Swarbrick, 2004). It is generally expressed as shown below:

Porosity (%) = (volume of pore spaces/total volume of rock) x 100

Because logging tools do not directly measure porosity, it is estimated using equation (1):

$$\Phi = (\rho_{ma} - \rho_b) \big/ (\rho_{ma} - \rho_{fl}) \quad (1)$$

where Φ is porosity, ρ_b is the bulk density of the rock, ρ_{ma} is the density of the matrix, ρ_{fl} is the density of the fluid. The density porosity, figure 3.19 is calculated by specifying ρ_b (observed on the log), ρ_{ma} (sandstone) and ρ_{fl} (oil). Where ρ_{ma} (quartz) = 2.65 g/cc, ρ_{fl} = 0.876 g/cc from oil API=30^0. Density porosity in the reservoir ranges from 25 % to 37 %.

3.2.7 Water saturation (Sw)

This is the fraction of the pore volume filled with formation water (Sheriff, 2002). It helps in quantifying the reservoir's hydrocarbon saturation and is calculated by using Archie's formula, equation (2):

$$S_w = \sqrt{a \big/ \Phi^m * R_w \big/ R_t} \quad (2)$$

where a is a constant, m is cementation factor, Φ is porosity, R_w is resistivity of formation water, and R_t is true resistivity of the formation. Selley (1985) pointed out that this method is valid for clean, clay-free formations. Because the Hoover field's "deep" resistivity logs records low resistivity, a larger S_w than should be the case would be obtained from the formula. Generally, a = 1 and m = 2; however, for unconsolidated sands (soft formations), a = 0.62 and m=2.15 from the Humble formula (Selley, 1985). From equation (2), the only unknown is R_w which has to be calculated from a brine-saturated portion of the log as shown below in equation (3):

$$S_w = \left(C * \left[R_w / R_t \right]^{1/2} \right) \Big/ \Phi \qquad (3)$$

Between 3560 ms and 3600 ms, HA-1 is assumed to be approximately 100 % water saturated in the sand unit; $R_t = R_o$ (Resistivity of rock with water) ≈ 0.27; Porosity ≈ 0.26; C = 0.9 for sands; $S_w = 1$; therefore, $R_w = 0.039$ ohm-m. By substituting the value of R_w in equation (2), one can calculate Sw (Fig. 3.19). Water saturation in the reservoir varies from 17 % to 67 % with an average value of 38 % for log HA-1, which means hydrocarbon saturation is 62 %.

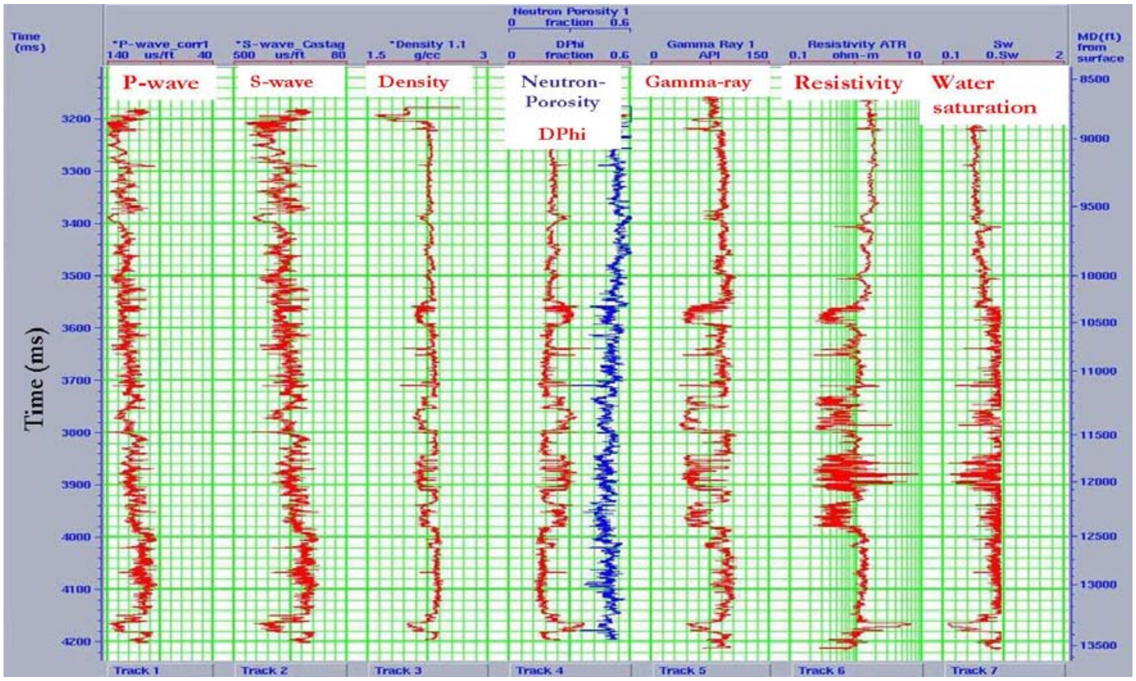

Figure 3.19: In-situ logs with calculated density porosity (DPhi) and water saturation for HA-1 prior to fluid substitution.

3.3 Fluid replacement modeling

3.3.1 Introduction

Fluid substitutions are an important part of seismic attribute studies because they provide the interpreter with a valuable tool for modeling various fluid scenarios, which might explain an observed amplitude variation with offset anomaly (Smith et al., 2003). In this research, fluid-replacement modeling (FRM) is carried out for oil- (in-situ), brine-, and gas-saturated reservoir sands. The Gassmann's equation, which relates the bulk modulus of the porous rock frame, mineral matrix, and the pore fluids, as well as the Batzle and Wang equations (Batzle and Wang, 1992), are used for this purpose.

The use of Gassmann's equation is based on the following assumptions, explained by Smith et al. (2003) and Wang (2001). The rock is homogeneous and isotropic, all pores are interconnected and communicating, pore pressure is equilibrated throughout the rock, the pore fluid does not interact with the solid in such a way that would soften or harden the frame, and the media is closed and no pore fluid leaves the rock volume.

3.3.2 Fluid-substitution equations

Smith et al. (2003) stated that the application of the Gassmann's equation is a two-part process, which involves the determination of the bulk modulus of the porous rock frame before calculating the bulk modulus of the rock saturated with any desired fluid (Smith et al., 2003). Important equations used in the FRM process include equations (4) to (10) listed below:

$$K_{sat} = K_{dry} + \frac{\left(1 - K_{dry}/K_{ma}\right)^2}{\Phi/K_{fl} + (1-\Phi)/K_{ma} - K_{dry}/K_{ma}^2} \tag{4}$$

$$K_{sat} = \rho_b \left(V_p^2 - \tfrac{4}{3} V_s^2\right) \tag{5}$$

$$\mu = \rho_b V_s^2 \tag{6}$$

$$V_p = \sqrt{\left(K_{sat} + \tfrac{4}{3}\mu\right)/\rho_b} \tag{7}$$

$$V_s = \sqrt{\mu/\rho_b} \tag{8}$$

$$\rho_b = \rho_{ma}(1 - \Phi) + \rho_{fl}\phi \tag{9}$$

where V_p is P-wave velocity (7), V_s is S-wave velocity (8), K_{dry} is bulk modulus of the dry frame (drained of any pore filling fluid), μ_{dry} is shear modulus of the dry frame, K_{ma} is the bulk modulus of the mineral matrix (grain), Φ is porosity, K_{fl} is the bulk modulus of the pore fluid, ρ_b is the bulk density of the formation (9), ρ_{ma} is the density of the matrix, ρ_{fl} is the density of the fluid, and K_{sat} is the bulk modulus of the rock saturated with pore fluid (4).

The bulk modulus or incompressibility of an isotropic rock, K, is the ratio of hydrostatic stress to volumetric strain, and is related to V_p, V_s, and ρ_b (5). Shear modulus or shear stiffness, μ is the ratio of shear stress to shear strain and is related to V_s and ρ_b (6). Smith et al. (2006) stated that while the K_{sat} of a rock may be sensitive to the composition of the pore fluid (4), the μ is insensitive and therefore does not vary in the course of fluid substitution (10).

$$\mu_{dry} = \mu_{wet} \tag{10}$$

3.3.3 Fluid-substitution

3.3.3.1 Case 1: In-situ fluid (Oil)

The background S-wave velocity was calculated with Castagna's mudrock equation, but this was for brine case and therefore not representative of the in-situ fluid in the reservoir (Fig. 3.20). To calculate the S-wave velocity for oil sand, the in-situ condition before fluid replacement is specified through parameters such as: V_p, ρ_b, Φ, and S_w. Fluid (oil, brine, and gas) properties listed in table 3.2 are calculated using the Batzle and Wang equations (Batzle and Wang, 1992) by specifying the reservoir pressure, gas gravity, temperature, oil gravity, GOR, and salinity. Reservoir pressure, temperature, and oil gravity were obtained from Cogswell (2001). Fluid properties, together with the matrix (sandstone) properties (K_{ma}, μ, and ρ_{ma}), are used in calculating the S-wave velocity at 38 % water saturation. Note that the density porosity and water saturation for the output remains the same as the input in order to modify only the S-wave. As a result, 4 new logs (Vp, Vs, ρ, and Poisson's ratio) are created (Fig. 3.21) and are used in creating a new AVO synthetic. Also calculated are other rock properties shown in table 3.2 and logs shown in figure 3.21. While both P-wave and density logs remain unchanged, the S-wave log increases and Poisson's ratio (PR) decreases.

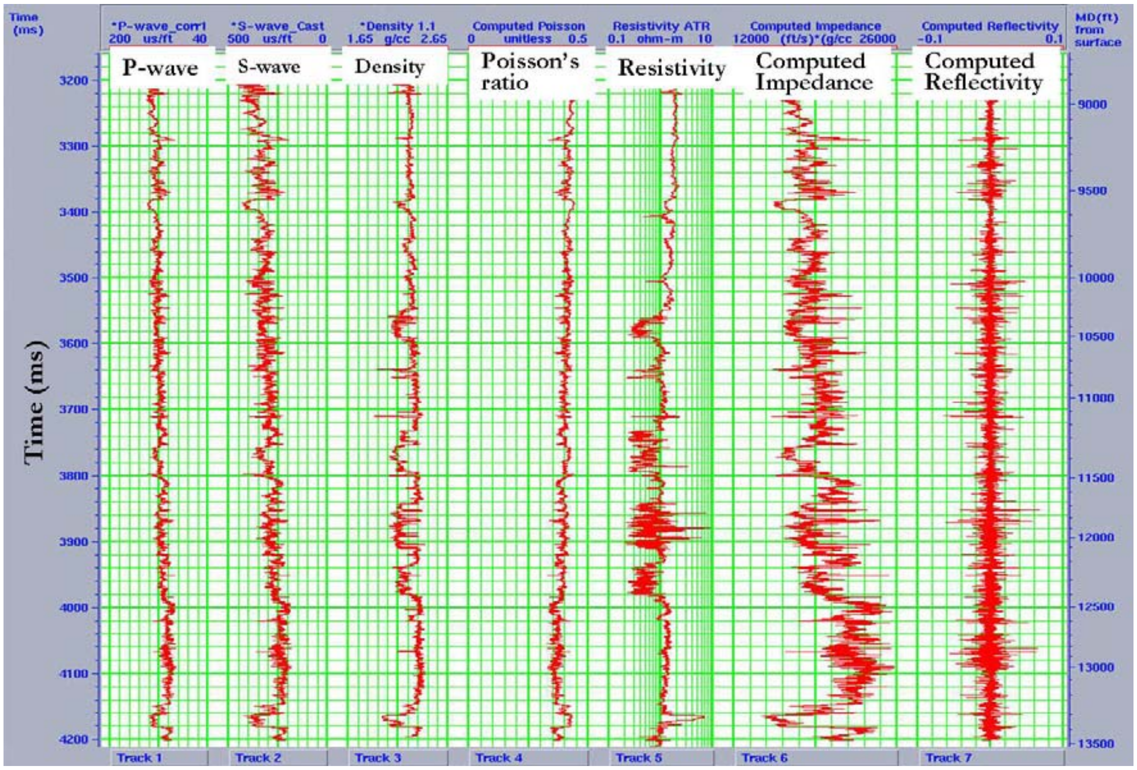

Figure 3.20: In-situ logs with calculated S-wave, Poisson's ratio, and impedance logs for HA-1 prior to fluid substitution.

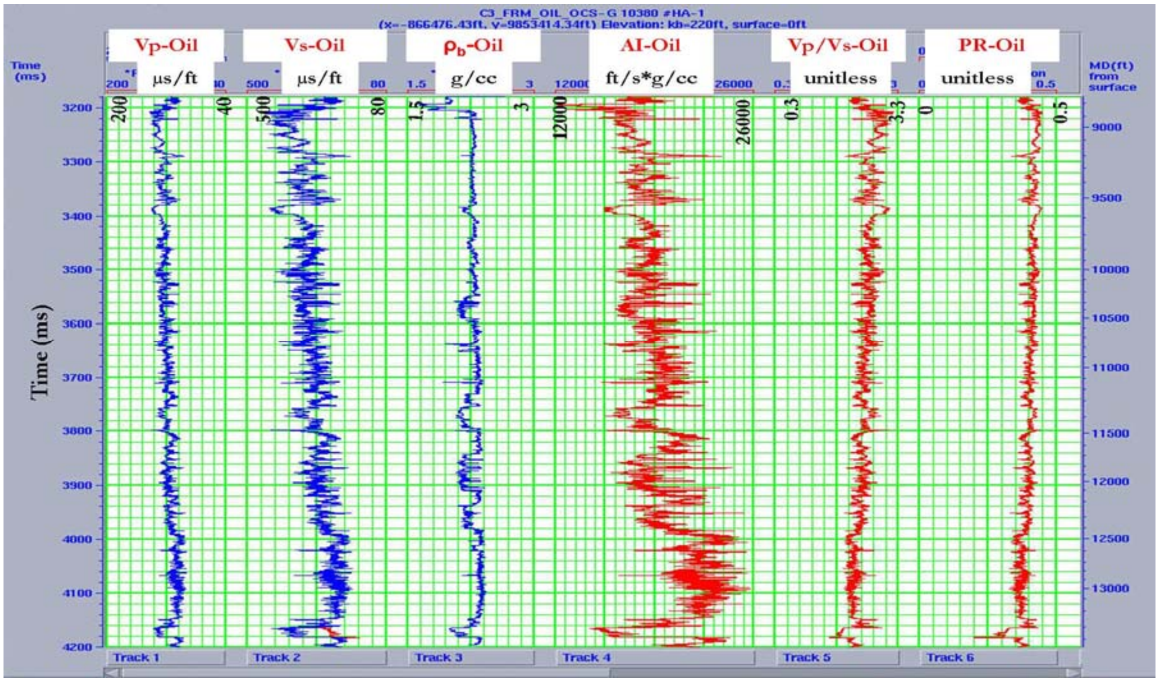

Figure 3.21: Result of fluid substitution for oil which creates a new S-wave log.

3.3.3.2 Case 2: Brine

The brine model is generated from the in-situ case with initial input parameters remaining the same as the input for oil. Other input parameters are as shown in table 3.2 and output, S_w is set at 100 % brine. After fluid substitution, V_p and ρ_b increases compared to original log, while Vs drops slightly (Fig. 3.22 and table 3.3). This results in a corresponding increase in acoustic impedance and Poisson's ratio above that of an oil-saturated reservoir.

3.3.3.3 Case 3: Gas

Using the 100 % brine model as the input, 62 % gas is introduced in the reservoir which results in sharp decrease in V_p, ρ_b, AI, PR, and an increase in V_s. Input parameters, as well as results of fluid substitution, are shown in table 3.2 and figure 3.23. Figure 3.24 shows the response of the reservoir properties to the different fluids. Synthetics generated for oil, brine, and gas from the models above are shown in figure 3.25.

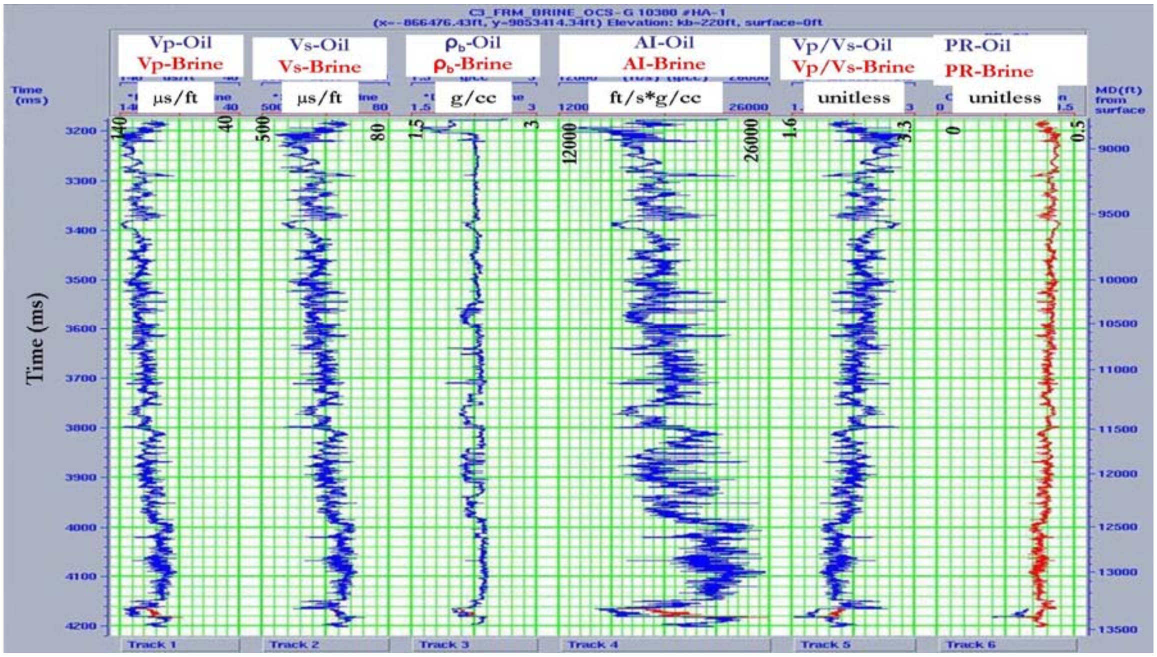

Figure 3.22: Results of fluid substitution for brine showing modified logs in red.

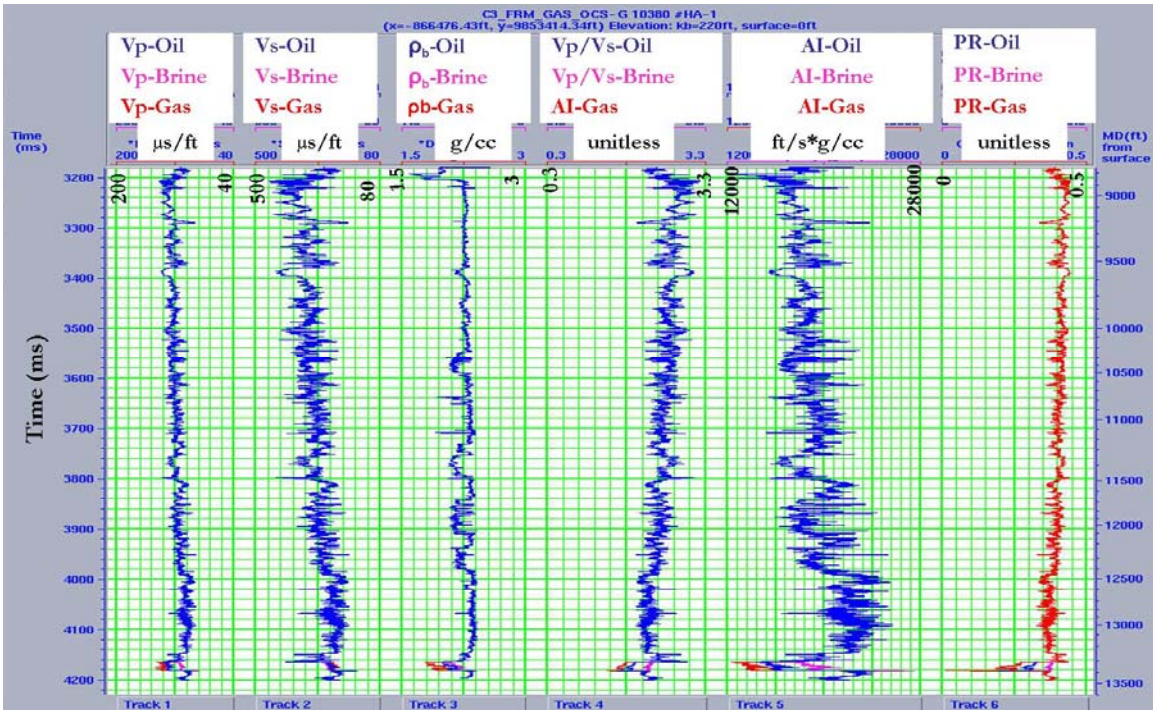

Figure 3.23: Results of fluid substitution for gas showing newly generated gas logs in red.

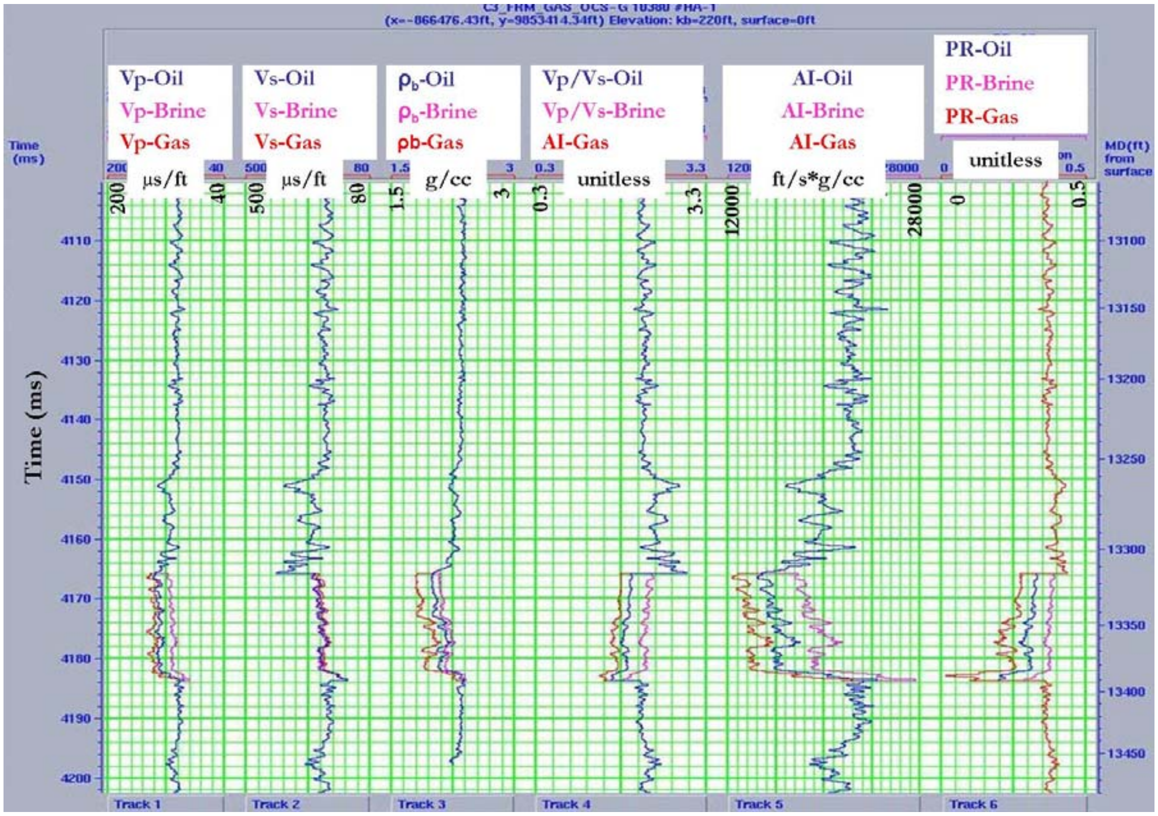

Figure 3.24: Close up on the fluid substitution results showing changes in the reservoir models for oil, brine, and gas.

3.3.4 Interpretation of results

3.3.4.1 Vp, Vs, ρ, Ksat, and PR

Results of fluid substitution in the reservoir show a general decrease in the Vp, ρ_b, and an increase in Vs (Fig. 3.24) as a result of the introduction of hydrocarbon for brine-saturated rock. An increase is observed when brine replaces hydrocarbons. Vp is also observed to be more sensitive to fluid changes than Vs. Going from oil to brine, Vp increases by 16 % whereas Vs drops by 2 %. The changes are greater in gas-saturated reservoirs. However, the most sensitive rock property is the saturated bulk modulus (Ksat), which changes by about 61 % from brine to oil and 120 % from brine to gas respectively (Table 3.3).

3.3.4.2 Vp/Vs ratio

Castagna et al. (1985) reported that the use of V_p/V_s ratio as a lithology indicator was popularized by Pickett (1963). They also reported the use of V_p, Vs, and V_p/V_s in seismic exploration for estimation of lithology and saturating fluids in particular stratigraphic intervals. Because the P-wave velocity is more sensitive to fluid changes than the S-wave velocity, changes in fluid type result in changes in V_p/V_s, as shown in figures 3.24. Here, it is observed that V_p/V_s, ratio for hydrocarbons is generally lower than brine (Fig. 3.25).

3.3.4.3 Impedance and amplitude contrasts

It can be seen from fluid substitution that the effect of gas saturation in the reservoir is more significant than oil of the same volume. The gas-filled reservoir sands have the lowest impedance and highest reflection amplitudes, whereas brine sands have the highest impedance and smallest reflection amplitudes. Oil sands, on the other hand, have properties lying between gas and brine properties (Fig. 3.26).

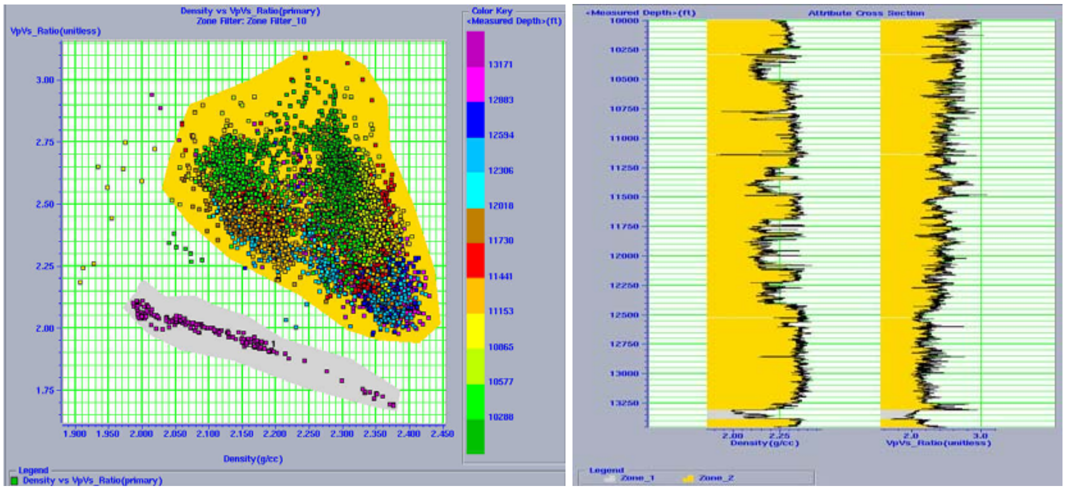

Figure 3.25: Crossplot (left) and cross section (right) display of density against Vp/Vs ratio, showing oil-saturated reservoir sands (grey) with low Vp/Vs ratio compared to shales and non-reservoir sands (yellow).

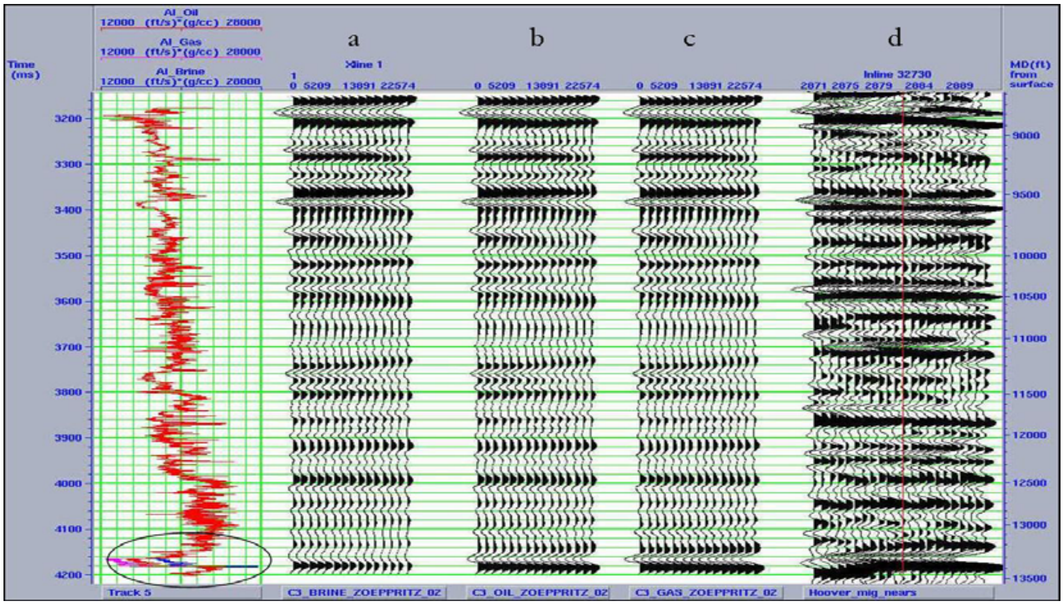

Figure 3.26: Synthetics generated for brine (a), oil (b) and gas (c) models after fluid substitution as well as near-angle stacked seismic (d).

Fluid Substitution Parameters	**Fluid**		
	Oil FRM	**Brine FRM**	**Gas FRM**
Input from logs			
Input P-wave (us/ft)	136	136	118
Vp (ft/s)	7355	7355	8509
Input S-wave (us/ft)	401	401	273
Vs (ft/s)	2493	2493	3660
Input density (g/cc)	2.01	2.01	2.10
Input water saturation (fraction)	0.38	0.38	1
Input porosity (%)	36.18	36.18	36.18
Input dry rock Poisson's ratio (fraction)	0.25	0.25	0.25
Input to Batzle and Wang			
Pore Pressure (psi)	6750	6750	6750
Temperature (F)	130F/54C	130F/54C	130F/54C
Gas-Oil ratio (cft/stb)	1500	1500	150000
Gas-Oil ratio (L/L)	267.14	267.14	26714.2
Saturation Gas-Oil ratio (L/L)	321.04	321.04	321.04
Oil Gravity (API)	30	30	30
Gas Gravity	0.7	0.7	0.7
Salinity (PPM)	10,000	10,000	10,000

Output from Batzle and Wang			
Brine Bulk Modulus (Gpa)	3.15	3.15	3.15
Brine Density (g/cc)	1.07	1.07	1.07
Hydrocarbon bulk modulus (Gpa)	0.73	0.73	0.17
Hydrocarbon density (g/cc)	0.68	0.68	0.30
Input fluid bulk modulus (Gpa)	1.03	1.03	3.15
Input fluid density (g/cc)	0.83	0.83	1.07
Output fluid bulk modulus (Gpa)	1.03	3.15	0.17
Output fluid density (g/cc)	0.83	1.07	0.31
Matrix bulk modulus (Gpa)	40	40	40
Matrix shear modulus (Gpa)	44	44	44
Matrix density (g/cc)	2.65	2.65	2.65
Input k dry (Gpa)	4.45	4.45	4.45
Input K sat (Gpa)	6.61	6.61	10.62
Input mu (Gpa)	2.61	2.61	2.61
Output from Gassmann fluid substitution			
Output K dry (Gpa)	4.45	4.45	4.45
Output K sat (Gpa)	6.61	10.62	4.83
Output mu (Gpa)	2.61	2.61	2.61
Output P-wave (us/ft)	136	118	143
Vp (ft/s)	7355	8509	7011
Output S-wave (us/ft)	267	273	254
Vs (ft/s)	3740	3660	3930
Output density (g/cc)	2.01	2.10	1.82
Output water saturation (fraction)	0.38	1	0.38
Output porosity (fraction)	36.18	36.18	36.18
Output dry rock Poisson's ratio (unitless)	0.25	0.25	0.25
Poisson's Ratio of rock and fluid (unitless)	0.33	0.39	0.27

🟦	Increase
⬛	No change
🟥	Decrease

Table 3.2: Fluid-replacement modeling input and output parameters.

Output from Gassmann fluid substitution					
	Reservoir fluids				
Rock property	**Oil**	**% change**	**Brine**	**% change**	**Gas**
Output K sat (Gpa)	6.61	61	10.62	120	4.83
Output P-wave (us/ft)	136	16	118	21	143
Vp (ft/s)	7355	16	8509	21	7011
Output S-wave (us/ft)	267	2	273	7	254
Vs (ft/s)	3740	2	3660	7	3930
Output density (g/cc)	2.01	4	2.10	15	1.83
Poisson's Ratio of rock and fluid (unitless)	0.33	19	0.39	43	0.27

Table 3.3: Sensitivity of output parameters to fluid substitution.

3.4 AVO modeling and analysis

3.4.1 Introduction

Sheriff (2002, p.12) defined AVO as "the variation in the amplitude of a seismic reflection with angle of incidence or source-geophone distance". Castagna and Swan (1997) stated that depending on rock property contrasts (velocity, density, and Poisson's ratio) at any interface, hydrocarbon-related AVO anomalies may show increasing or decreasing amplitude variation with offset/angle of incidence. Although bright spots are potential hydrocarbon indicators, they are not unique to hydrocarbons (Chiburis et al., 1993; Sen, 2006). AVO modeling, the creation of non-normal incident synthetics from logs, helps one to understand and differentiate hydrocarbon-related AVO responses from applicable lithology (Ross, 2000). In this research, AVO modeling and analysis is carried out on synthetics generated from logs and gathers/traces extracted from near- and far-angle stacked seismics, due to the unavailability of CDP gathers.

Based on Rutherford and Williams' classification (1989), there are three main classes of AVO anomalies (Fig. 3.27). Class I sands have higher impedance than the encasing shale, with relatively large positive zero-offset reflection coefficient (Ro). Class II sands have nearly the same impedance as the encasing shale and are characterized by near-zero Ro. Class III sands have lower impedance than the encasing shale with large negative values for Ro. It was demonstrated by Castagna and Swan (1997) that the same gas sand produces very different AVO behavior depending on its overlying shale, and it would therefore be incorrect to classify a reflector based on the property of sand alone. They proposed Class IV, a low impedance gas sand with reflection coefficient, which decreases with offset (Fig. 3.28). These four responses were also classified based on the position of AVO anomalies on the A-B plane, as shown in figure 3.29 and described in figure 3.30. Because stacking of seismic data destroys AVO information, fluid information can be observed by comparing angle stacks (Chiburis et al., 1993). The normalized amplitudes from the full-, near- and far-angle stacks in Hoover field shown in figure 2.17 indicate an apparent Class IV AVO. Class IV varies from Class III at far offset because of its negative S-wave velocity contrast with the overlying rock, unlike Class III which has a positive contrast.

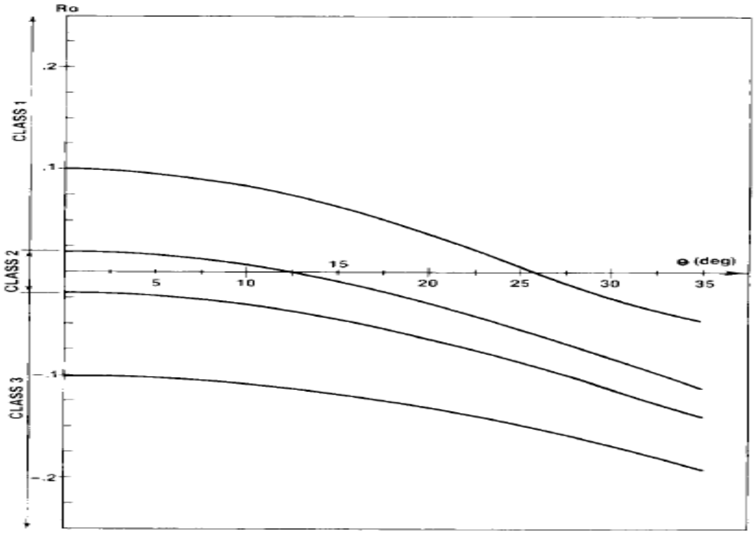

Figure 3.27: Zoeppritz P-wave reflection coefficients for a shale-gas sand interface for a range of reflection coefficients (from Rutherford and Williams, 1989).

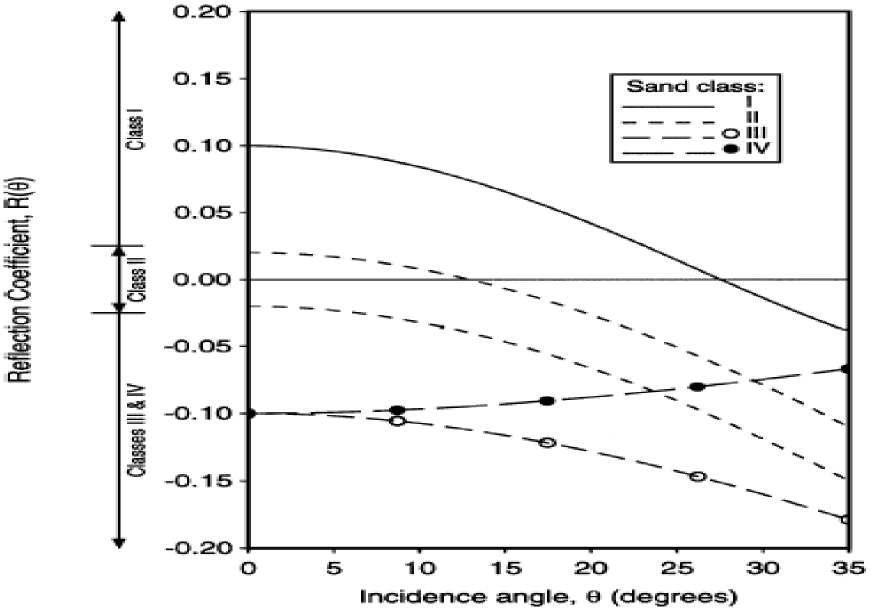

Figure 3.28: Classification of AVO response using P-wave reflection coefficient (from Castagna & Swan, 1997).

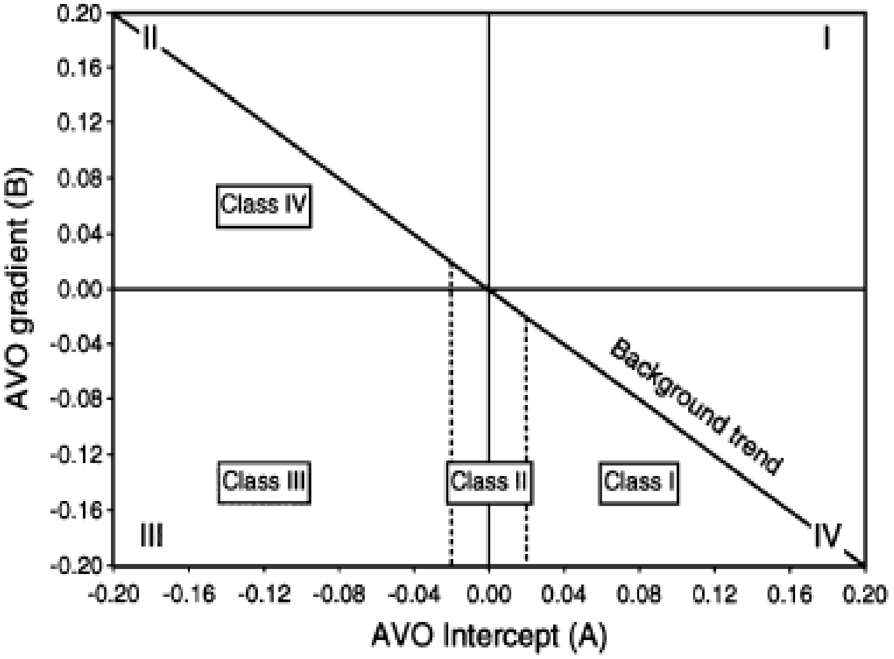

Figure 3.29: AVO intercept (A) and gradient (B) crossplot (from Castagna & Swan, 1997).

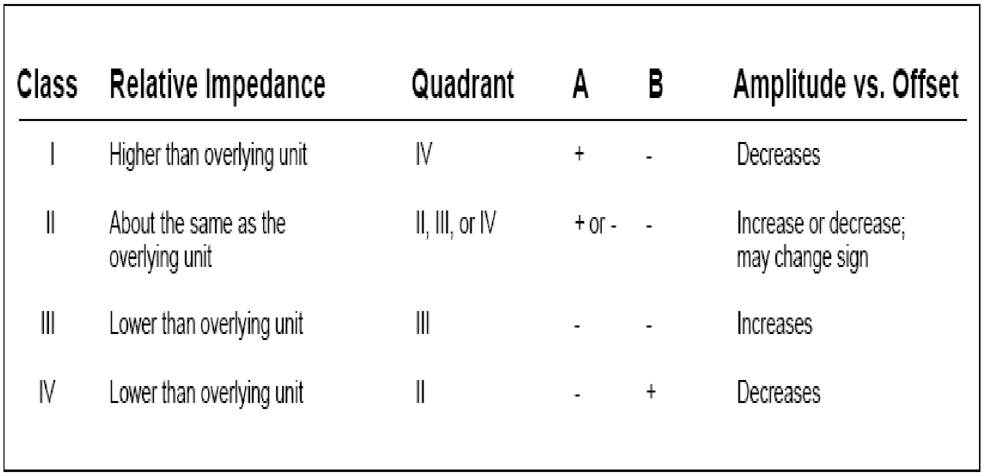

Class	Relative Impedance	Quadrant	A	B	Amplitude vs. Offset
I	Higher than overlying unit	IV	+	-	Decreases
II	About the same as the overlying unit	II, III, or IV	+ or -	-	Increase or decrease; may change sign
III	Lower than overlying unit	III	-	-	Increases
IV	Lower than overlying unit	II	-	+	Decreases

Figure 3.30: AVO behavior for gas sands (from Castagna and Swan, 1997)

3.4.2 Synthetic modeling of AVO from logs

Chiburis et al. (1993, p.44) stated that "the key to using AVO for fluid identification is comparison of real data with a synthetic seismogram". In this research, Hampson-Russell's AVO is used in the generation of AVO synthetic seismograms for fluid-saturated rocks (oil, brine and gas) with input density and velocity logs (P-wave and S-wave) coming from well HA-1. Synthetics are generated for angles 0^0 – 42^0 (0 – 24310 ft / 7409.69 m offset) with the use of Zoeppritz and elastic wave equations, and analysis results compared. Although both equations calculate the amplitudes of seismic waves, the Zoeppritz equations consider only plane-wave amplitudes of reflected P-waves and ignore interbed multiples and mode-converted waves (Hampson and Russell, 1999). The elastic wave algorithm, on the other hand, models both multiples and mode-converted waves. Using both algorithms, synthetics are created taking into account transmission losses and geometric spreading (Figs. 3.31 and 3.32). Ignoring these would result in a false Class III AVO (Fig. 3.33). The seismic event of interest is the high amplitude at about 4180 ms corresponding to the interface between reservoir sand and encasing shales. Although the three synthetic seismograms (oil, brine, and gas) all show large normal-incident amplitudes, the gas synthetics shows the largest amplitude, brine shows the smallest, and oil falls between brine and gas.

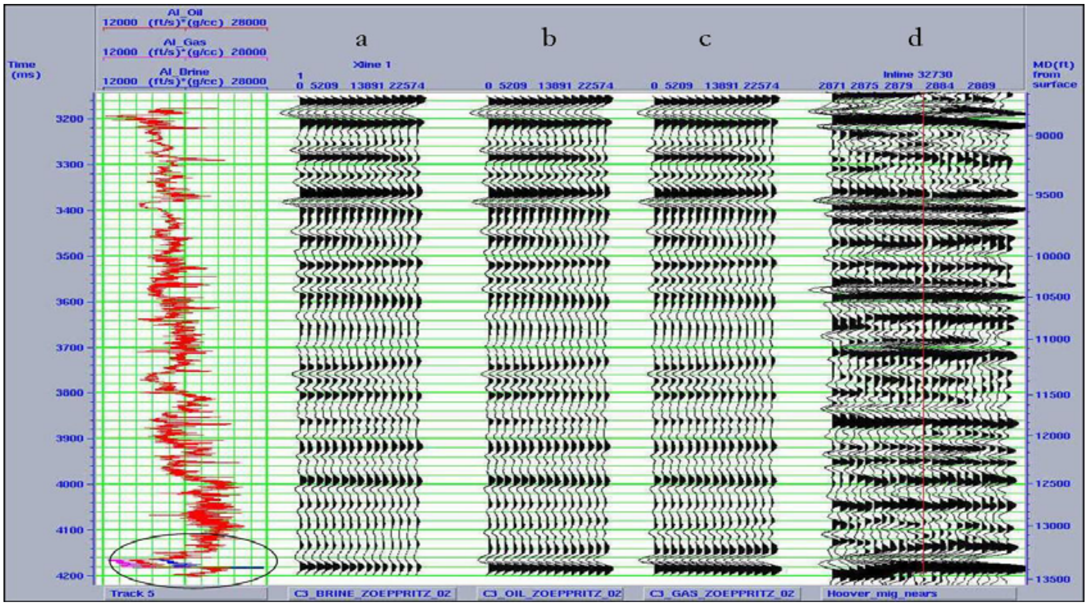

Figure 3.31: (a) Brine, (b) oil, and (c) gas AVO synthetics generated from the exact Zoeppritz equations taking into account geometric spreading and transmission losses, and (d) near-angle stacked seismic.

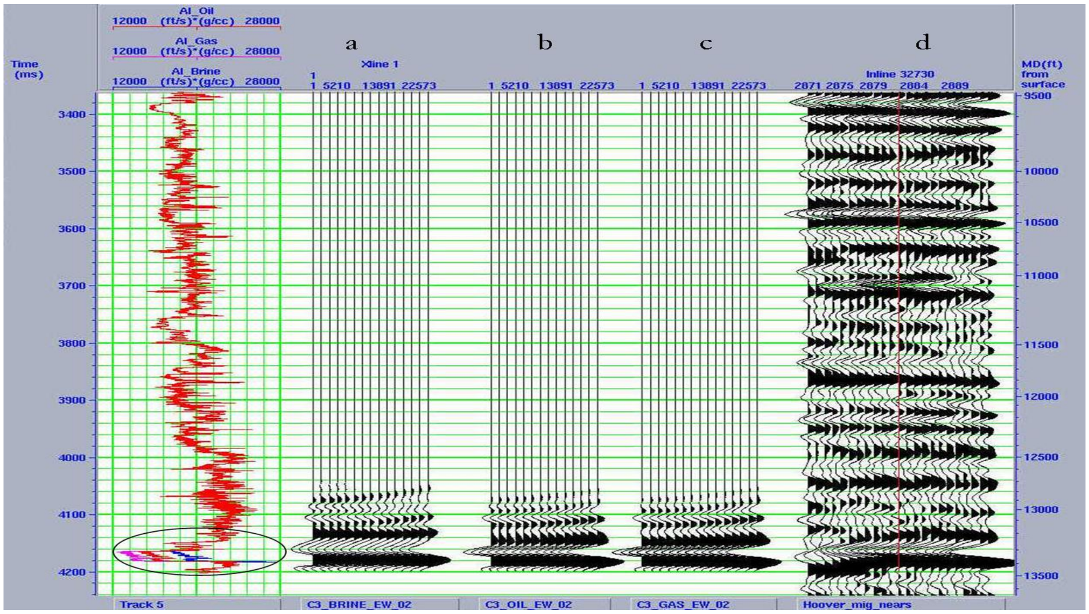

Figure 3.32: (a) Brine, (b) oil, and (c) gas AVO synthetics generated from the elastic wave equations taking into account geometric spreading and transmission losses, and (d) near-angle stacked seismic.

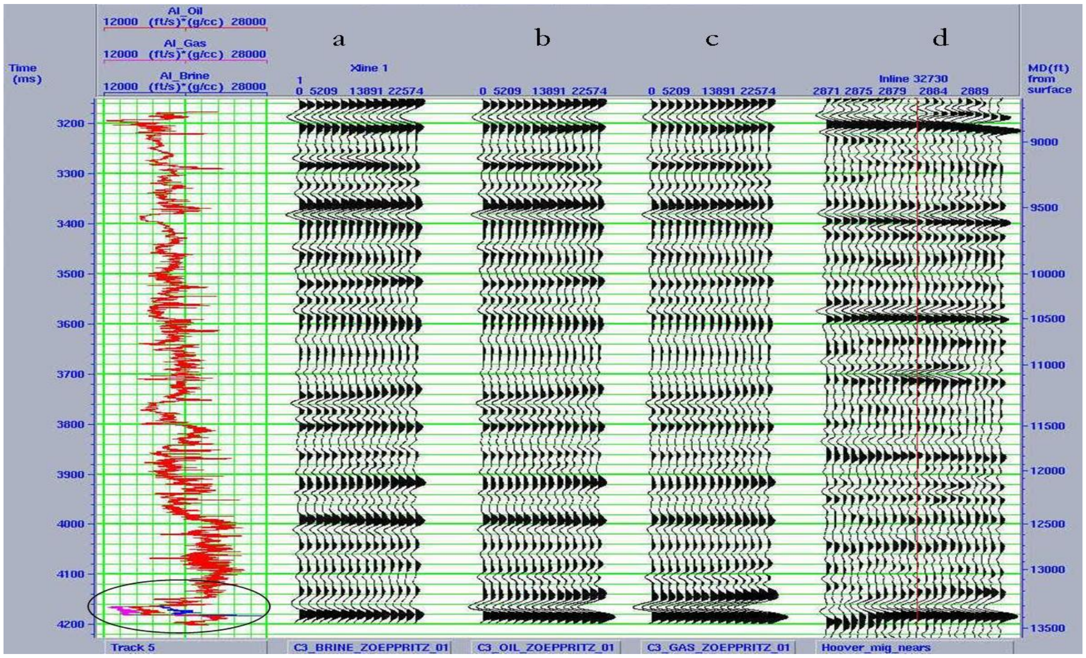

Figure 3.33: (a) Brine, (b) oil, and (c) gas AVO synthetics generated from the full Zoeppritz equations while ignoring transmission losses and geometric spreading, and (d) near-angle stacked seismic.

3.4.3 AVO-gradient analysis plot / curves

Using Shuey's three term approximation of the Zoeppritz equations (1) the AVO effects at the shale-sand interfaces for different fluids is quantified and displayed as curves.

$$R(\theta) = A + B \sin^2(\theta) + C \sin^2(\theta) \tan^2(\theta) \qquad (1)$$

where R is reflection coefficient, θ is angle of incidence, A is AVO intercept (a measure of normal incidence amplitude), B is AVO gradient (a measure of amplitude variation with offset), and C is AVO curvature which is often neglected (Castagna and Swan, 1997). Plots of AVO curves for troughs in blue (bottom of shale and top of sand interface) and peaks in red (bottom of sand and top of shale interface) are generated in order to display the variation in amplitudes between different fluids in reservoir sands and to compare hydrocarbon and non-hydrocarbon-saturated sands.

The trace recorded at zero offset starts with large negative reflection coefficient (large amplitude), it becomes less negative as offset increases for oil, brine, and gas synthetics generated from Zoeppritz equations (Figs. 3.34, 3.35 and 3.36). On the other hand, for synthetics generated with the elastic wave equations, only brine sands decrease in amplitude, whereas oil and gas amplitudes increase with offset (Figs. 3.37, 3.38 and 3.39). Although brine sands in the reservoir exhibit a negative zero-offset reflection coefficient (≈-0.045) at the top of the reservoir (Fig. 3.34), it has smaller amplitude which also decreases faster than oil (≈-0.1) and gas (≈-0.15) (Figs. 3.35 and 3.36 respectively). A comparison of synthetics generated from both equations shows positive gradient and negative intercept for oil and gas in synthetics created from Zoeppritz equations, whereas elastic wave equations generated oil and gas synthetics have negative intercepts and gradients. The first synthetics model the Hoover data; however the second case does not and would not be used in subsequent modeling.

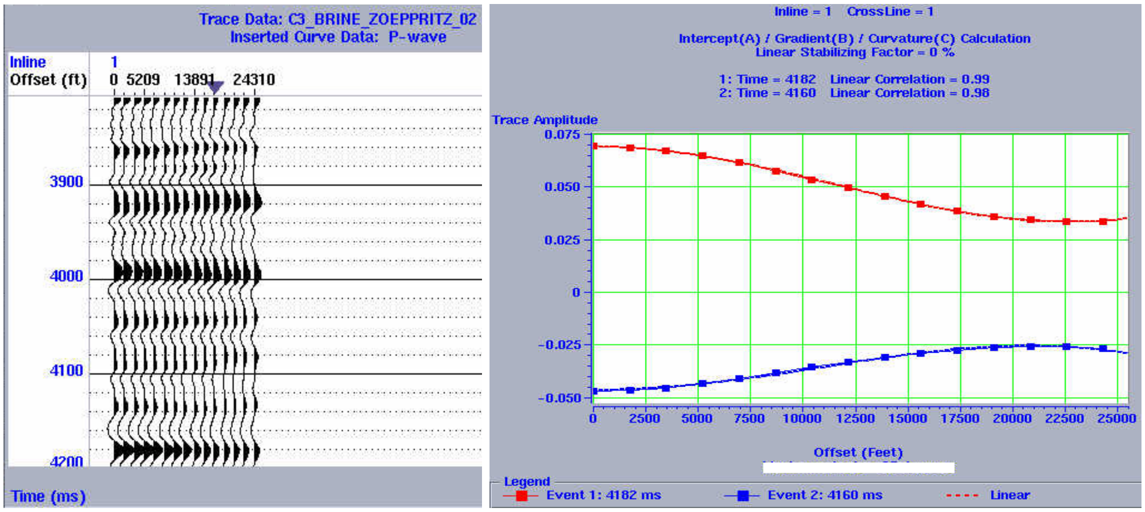

Figure 3.34: AVO synthetic (left) and gradient analysis plot (right) for brine-saturated reservoir sands using the exact Zoeppritz equations.

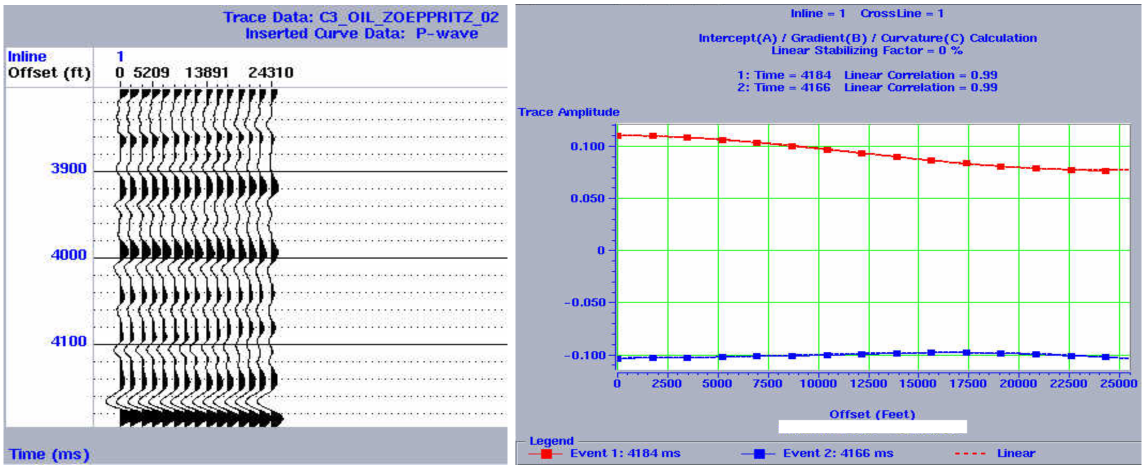

Figure 3.35: AVO synthetic (left) and gradient analysis plot (right) for oil-saturated reservoir sands using the exact Zoeppritz equations.

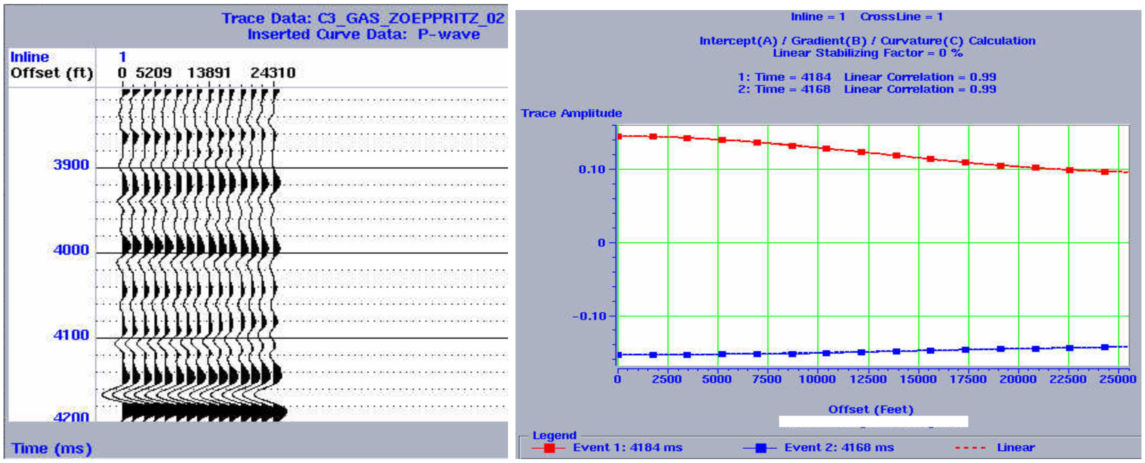

Figure 3.36: AVO synthetic (left) and gradient analysis plot (right) for gas-saturated reservoir sands using the exact Zoeppritz equations.

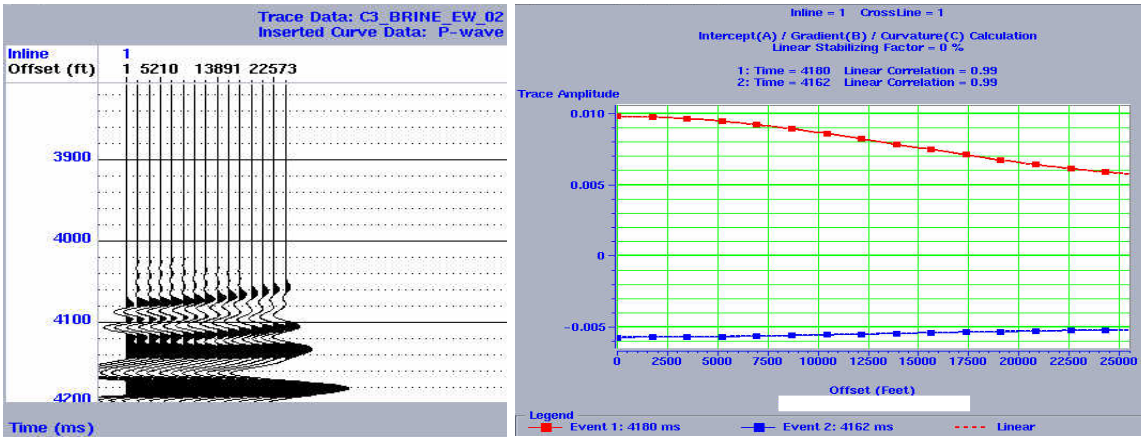

Figure 3.37: AVO synthetic (left) and gradient analysis plot (right) for brine-saturated reservoir sands using the elastic wave equations.

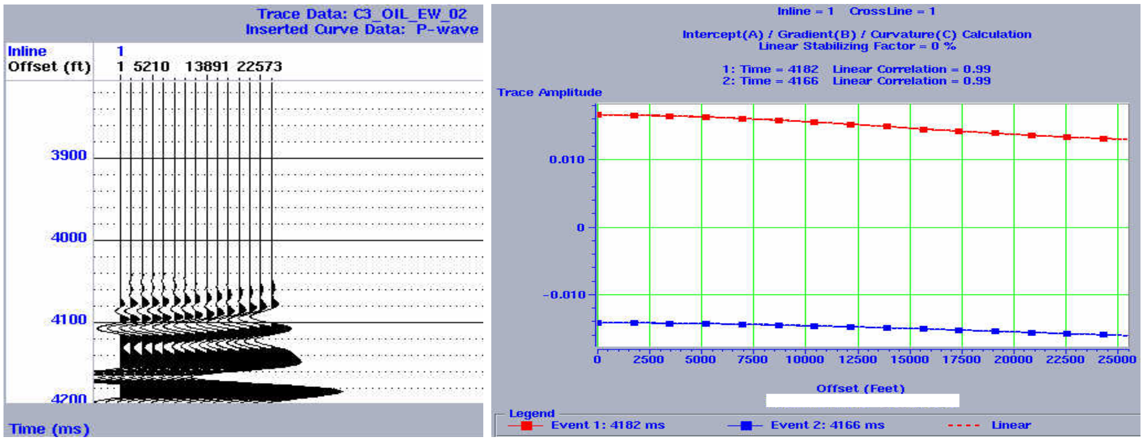

Figure 3.38: AVO synthetic (left) and gradient analysis plot (right) for oil-saturated reservoir sands using the elastic wave equations.

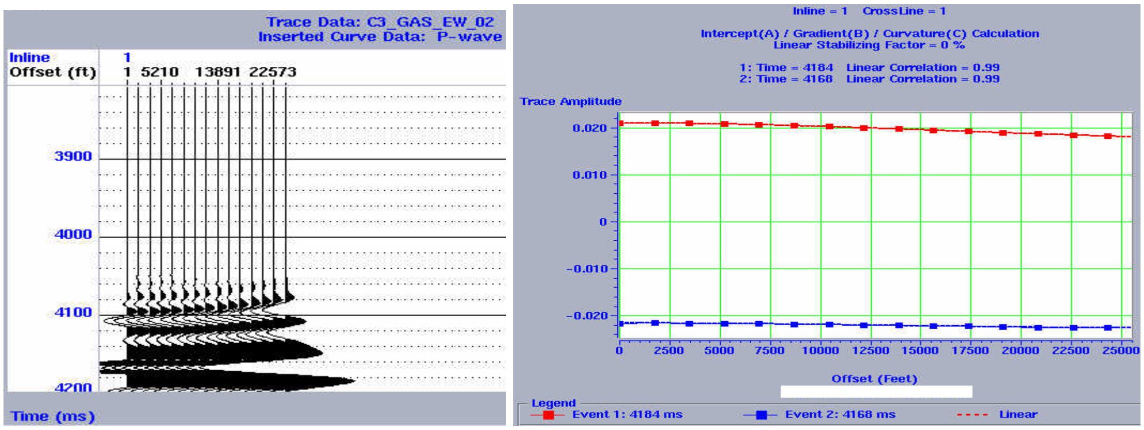

Figure 3.39: AVO synthetic (left) and gradient analysis plot (right) for gas-saturated reservoir sands using the elastic wave equations.

3.4.4 AVO attributes and crossplots

Two primary attributes, gradient and intercept, are extracted from the generated synthetics. These may be combined to form a single attribute such as AVO product (A x B) or scaled Poisson's ratio change ($\alpha A + \beta B$) where α and β are both scalars, whose values obtained for this analysis are 0.5 and 0.27 respectively, determined by equations provided by Ross, (2000). In figures 3.40 to 3.43, which compares brine-oil and brine-gas synthetics, A is shown as the wiggle trace and a combined AVO attribute term such as AVO product is the variable intensity color display respectively.

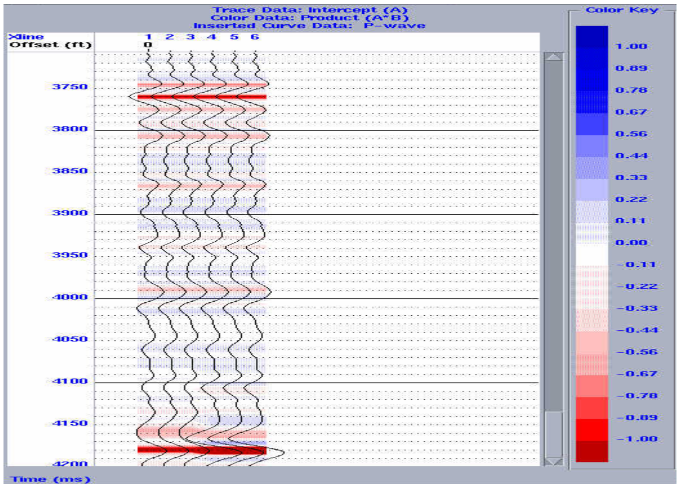

Figure 3.40: AVO product for brine and oil synthetics.

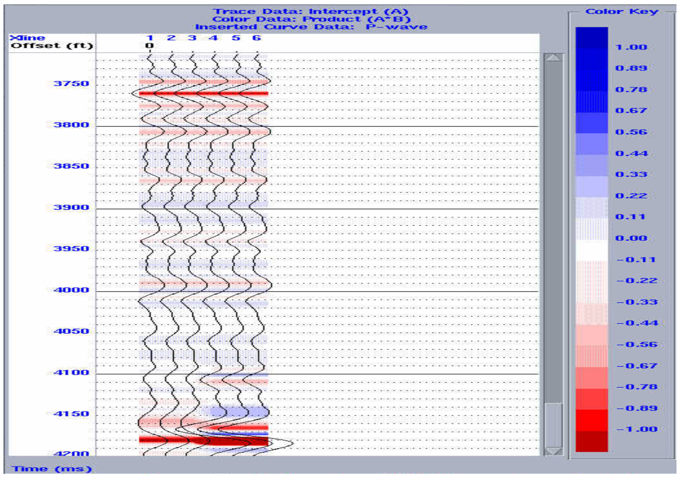

Figure 3.41: AVO product for brine and gas synthetics.

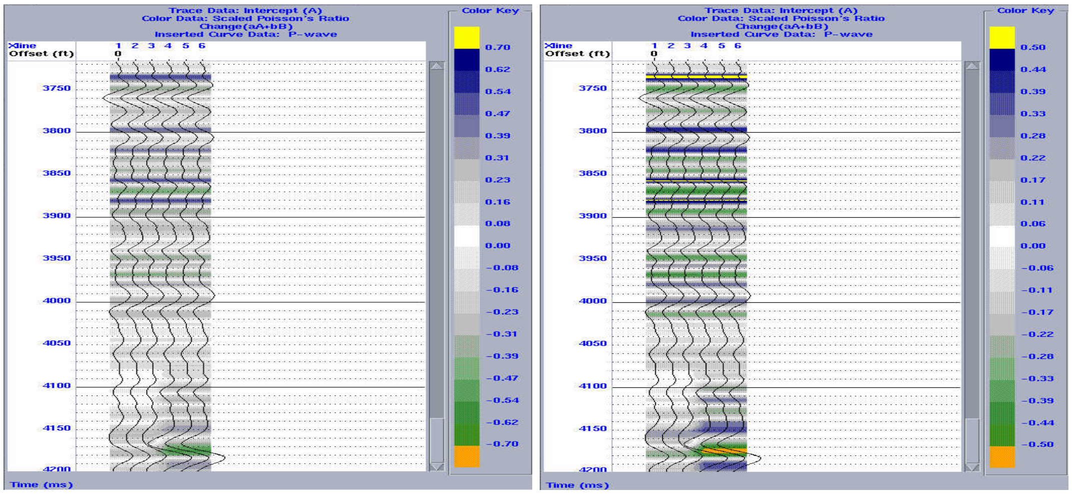

Figure 3.42: Scaled Poisson's ratio change for brine and oil synthetics.

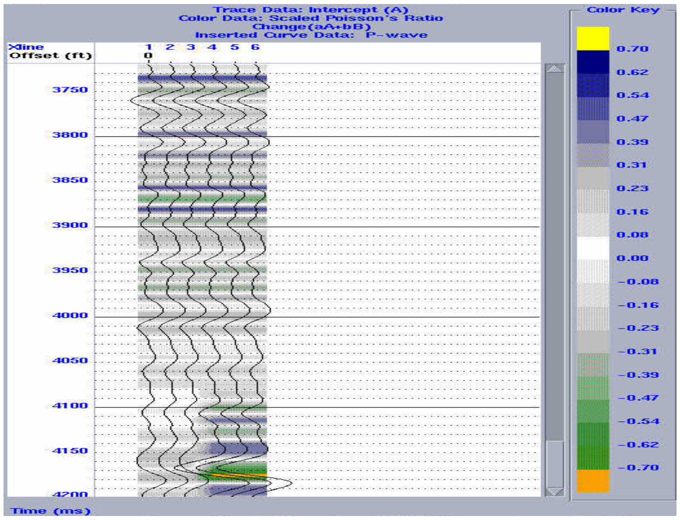

Figure 3.43: Scaled Poisson's ratio change for brine and gas synthetics.

Other attributes also explored are those based on the reflection coefficient of P-wave (Rp) and S-wave (Rs), which include: fluid factor (Figs. 3.44 and 3.45), sum of reflection coefficients, αRp + βRs (Figs. 3.46 and 3.47), and differences in reflection coefficients, αRp – βRs (Figs. 3.48 and 3.49).

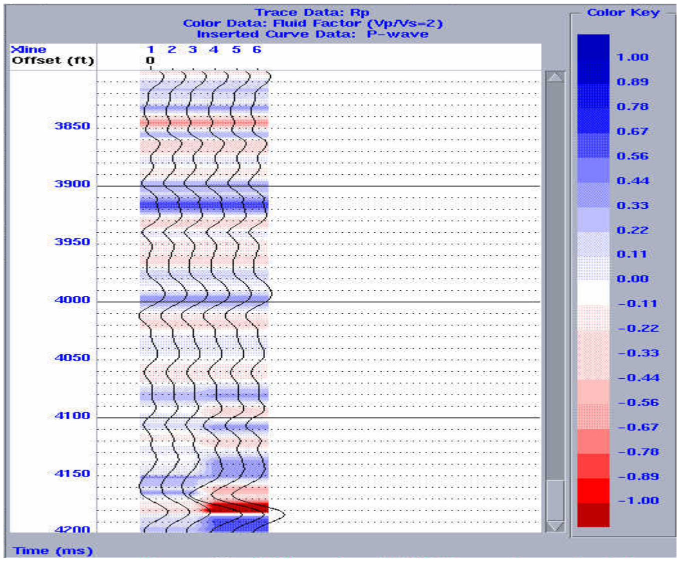

Figure 3.44: Fluid factor for brine and oil synthetics.

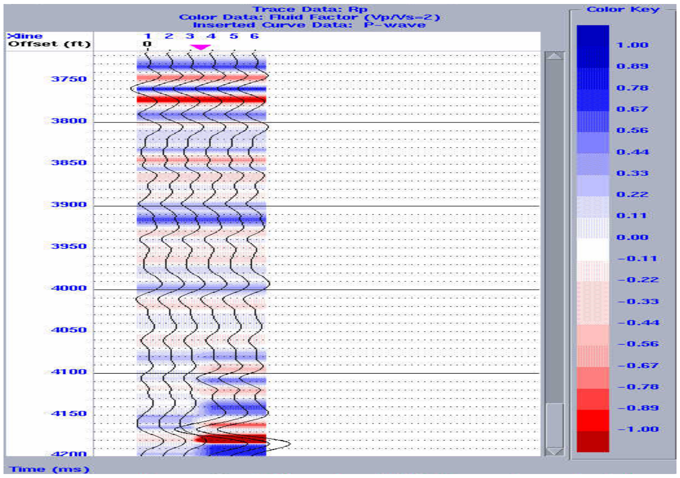

Figure 3.45: Fluid factor for brine and gas synthetics.

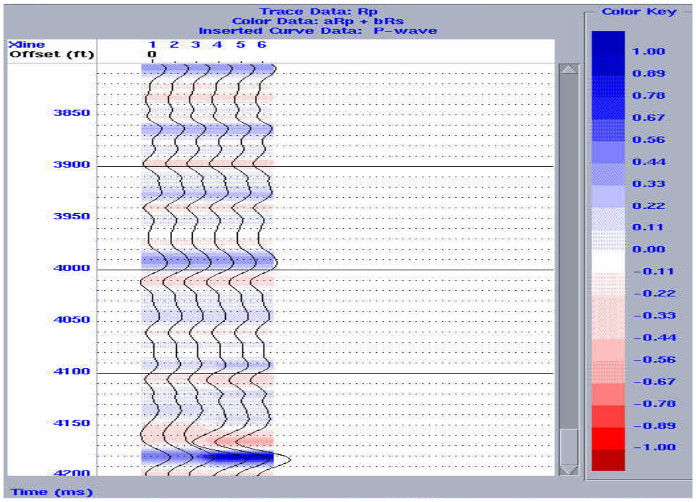

Figure 3.46: αRp + βRs for brine and oil synthetics.

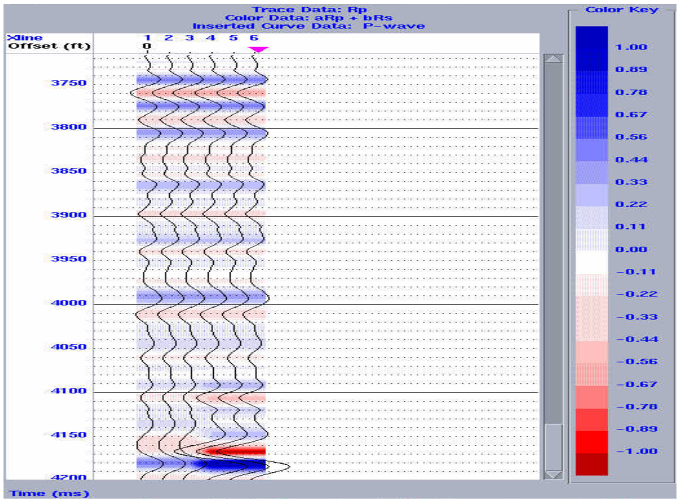

Figure 3.47: αRp + βRs for brine and gas synthetics.

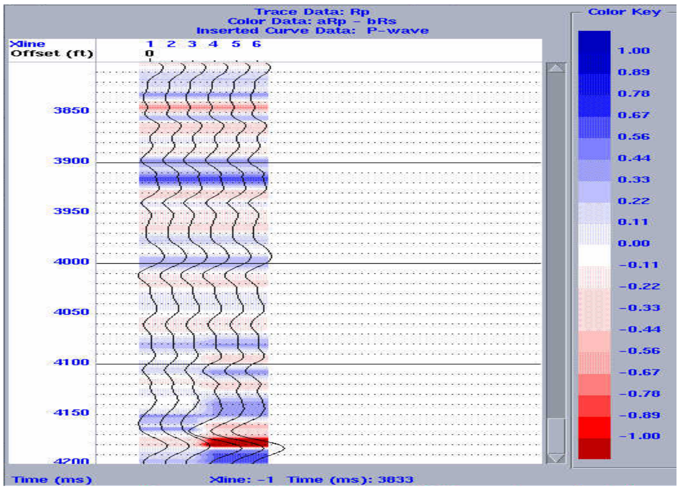

Figure 3.48: αRp - βRs for brine and oil synthetics.

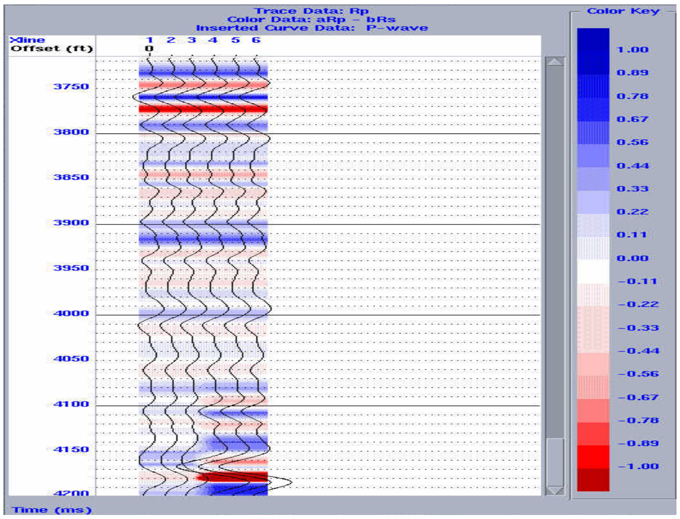

Figure 3.49: αRp - βRs for brine and gas synthetics.

It is observed from the above that the AVO product is not a good attribute to discriminate Class IV AVO oil/gas sands from brine sands because both synthetics have negative intercepts and positive gradients which results in negative products. However, scaled Poisson's ratio, fluid factor, reflection coefficient sum, and differences all show appreciable contrasts between brine-oil and brine-gas synthetics. Modeled attributes show a generally larger contrast for brine-gas synthetics than brine-oil synthetics.

Because a single attribute can be ambiguous, the use of crossplots of these AVO attributes is explored. Ross (2000, p.700) stated that "the need for seismic crossplotting arises from the complexities of the subsurface, the non-uniqueness of elastic seismic responses, and the desire to display multiple attributes simultaneously". Castagna and Swan (1997) and Castagna et al. (1998) pointed out that crossplotting facilitates AVO interpretation. They also observed that while non-hydrocarbon-bearing clastic rocks often exhibit a well defined background trend in a given time window, deviations from this trend indicates hydrocarbons or unusual lithologies. Crossplots generated from modeled seismic data (brine-oil and brine-gas synthetics) for an 80 ms window centered on 4175 ms are shown in figures 3.50 and 3.52 respectively, where the background brine and anomalous hydrocarbon zones clusters are projected back to the synthetic (Figs. 3.51 and 3.53). The top of oil and gas sand reflections plot below the background values, whereas the bottom reflections plot above the background.

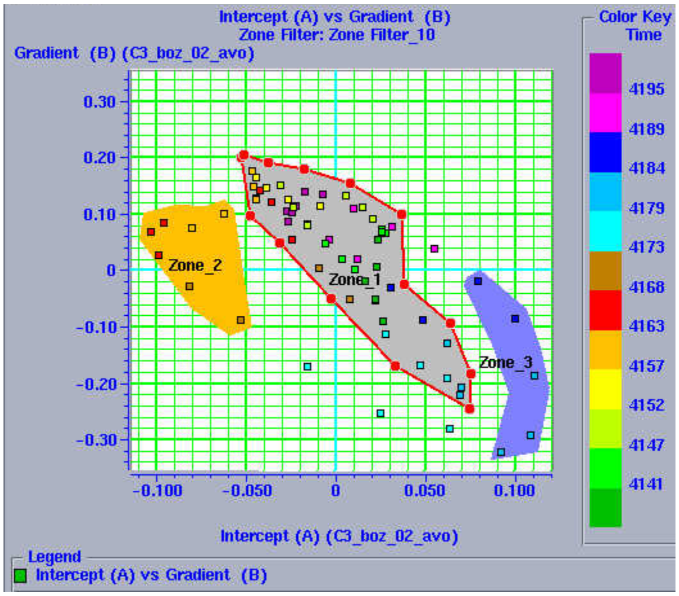

Figure 3.50: AVO attributes crossplot for brine and oil synthetics.

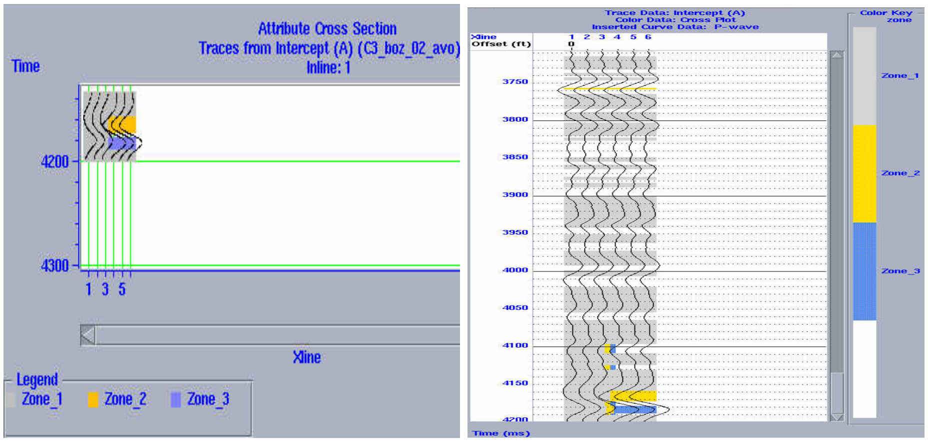

Figure 3.51: Crossplots transferred to brine-oil synthetics cross-sections.

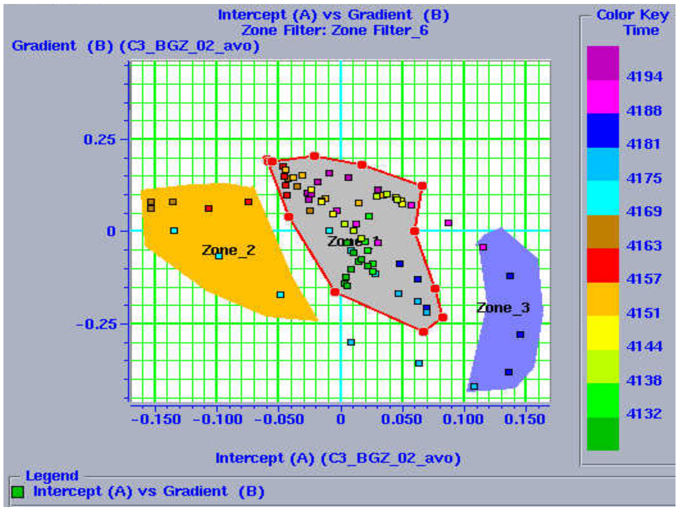

Figure 3.52: AVO attributes crossplot for brine and gas synthetics.

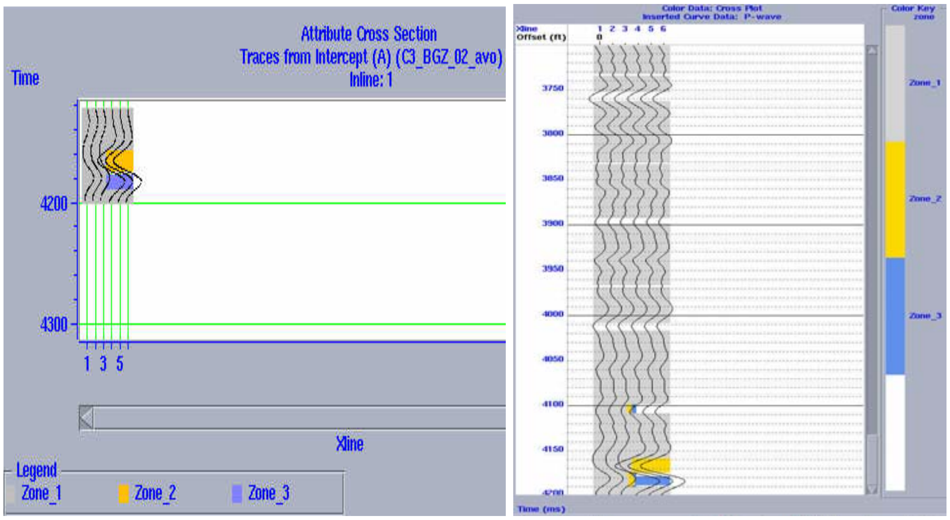

Figure 3.53: Crossplots transferred to brine-gas synthetics cross-sections.

3.4.5 AVO-attributes extraction from gathers

As a result of the absence of CDP gathers for AVO analysis, near (1) and far (2) traces have been extracted from each stacked volume (Figs. 3.54 and 3.55). Results of AVO analysis are shown in figures 3.56 to 3.60. Hydrocarbon zones are identified by AVO attributes, scaled Poisson's ratio change, AVO intercept, and sum of reflection coefficients. Cross plotting could not be applied on the gathers because only two traces are available.

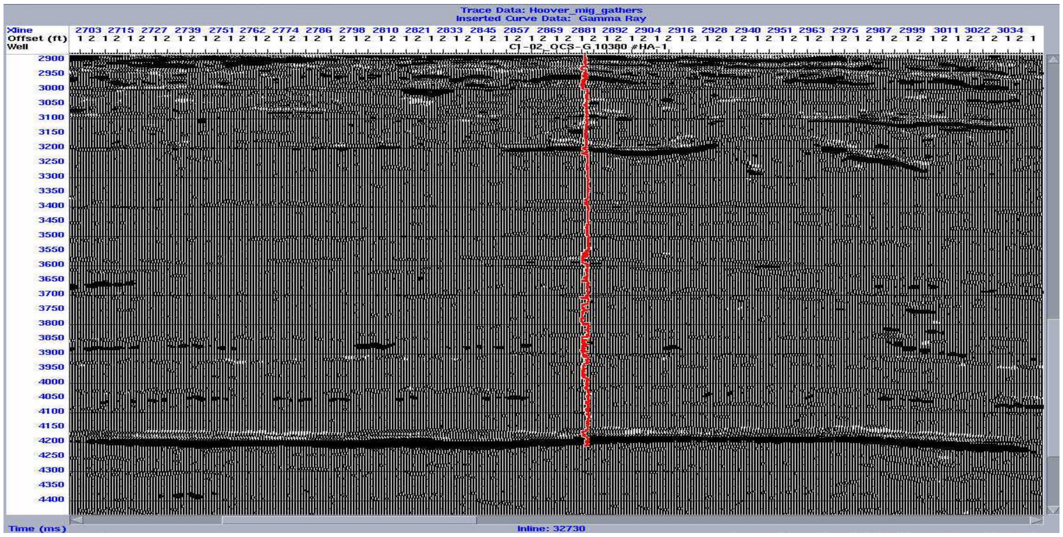

Figure 3.54: A section showing gathers generated by extracting traces from near- and far-angle stacked seismic volume shown as 1 and 2 offsets respectively.

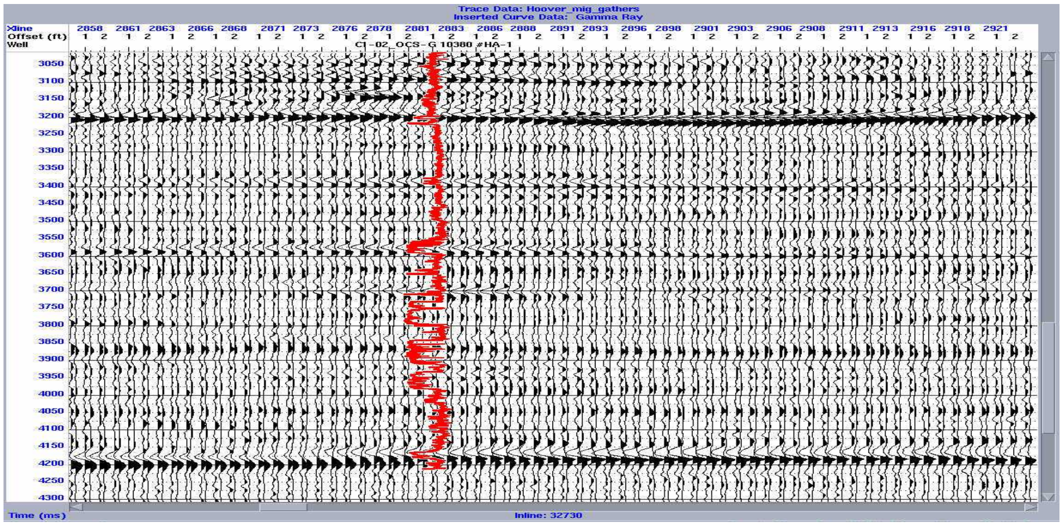

Figure 3.55: A close up section of extracted traces in figure 3.54 with inserted gamma-ray log showing each pair of near and far traces.

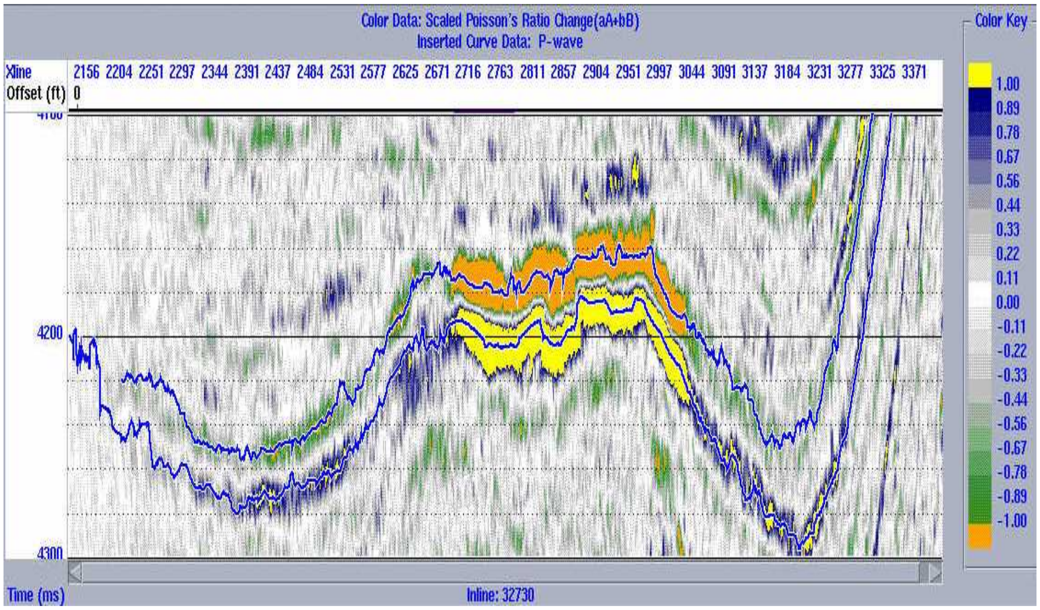

Figure 3.56: Scaled Poisson's ratio change extracted from gathers showing reservoir zone with strongest contrast, where the top of the reservoir shows a decrease as a result of the introduction of hydrocarbon.

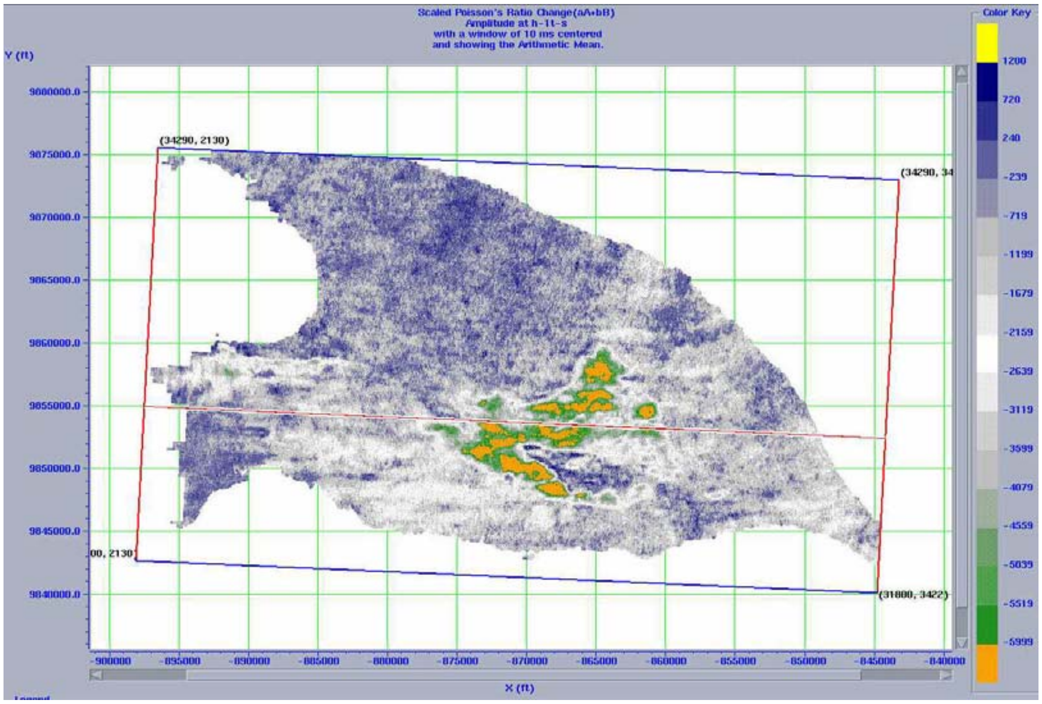

Figure 3.57: Scaled Poisson's ratio change on horizon slice through the top of the reservoir in figure 3.56 with a 10 ms window showing the hydrocarbon sands with large negative amplitude.

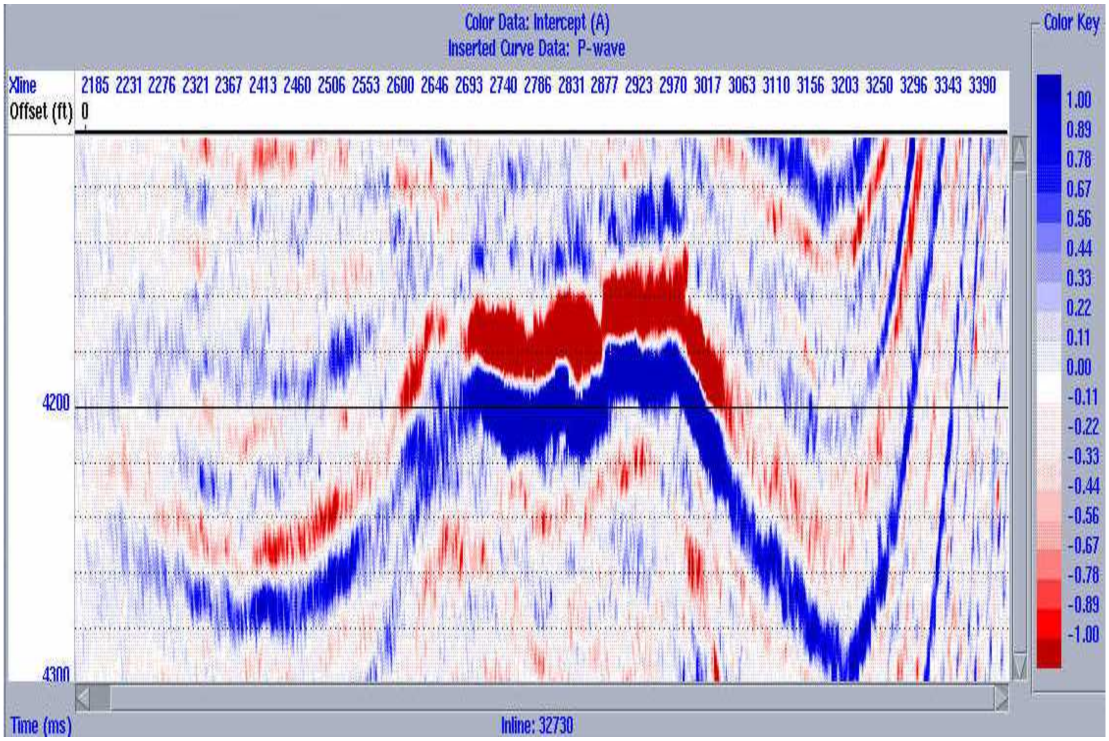

Figure 3.58: AVO intercept, (A) on gathers showing anomalously low intercept at the top of the reservoir.

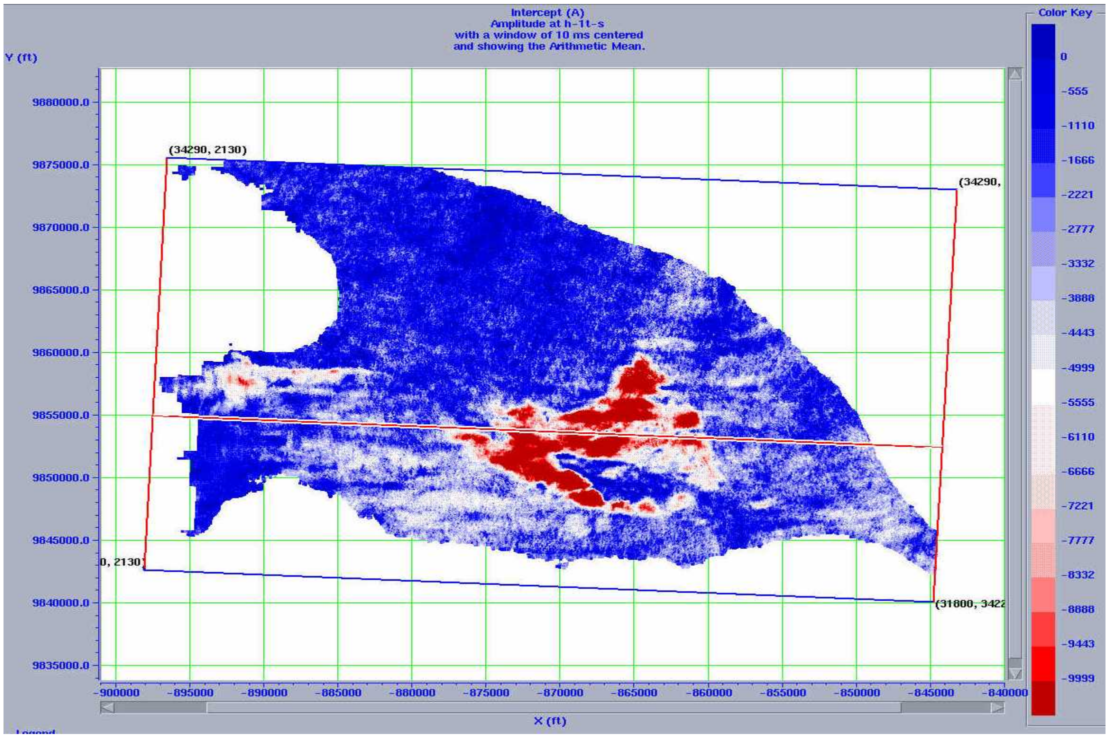

Figure 3.59: AVO intercept on horizon slice through the top of the reservoir in figure 3.58 with a 10 ms window showing the hydrocarbon sands with large negative amplitude.

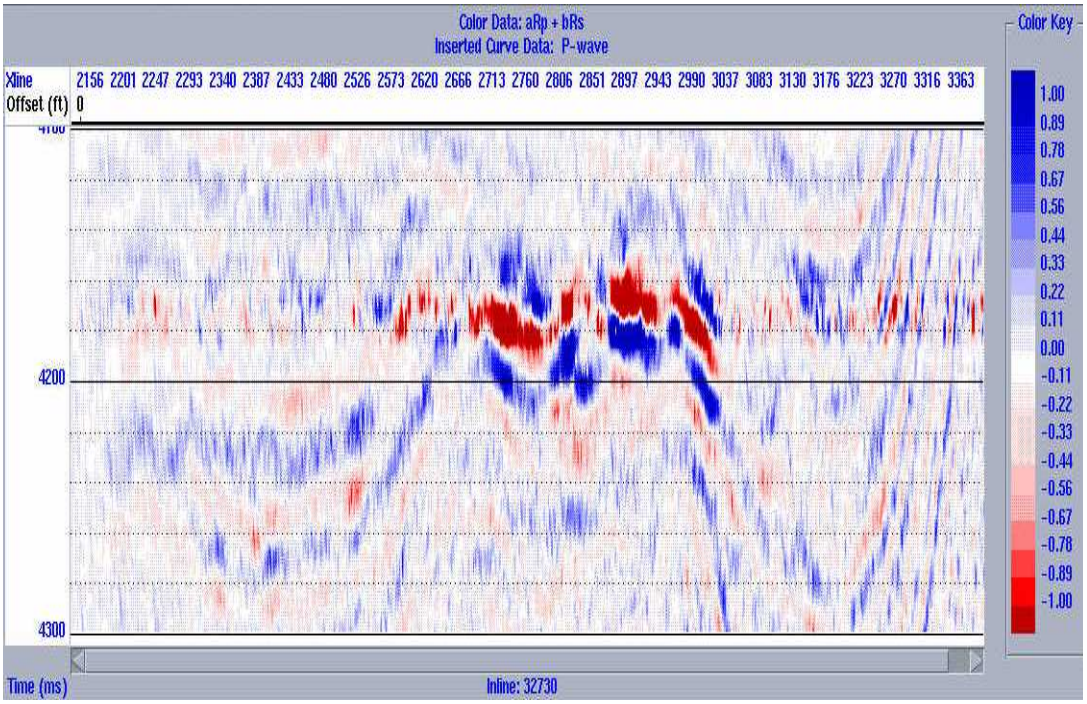

Figure 3.60: Sum of reflection coefficients, (aRp+bRs) on gathers showing reservoir zone with large contrast.

Chapter 4: Inversion of seismic data

4.1 Introduction

Inversion literally means to undo an operation (Veeken, 2007). Russell (2005, p.3) defined it as "the process of extracting from the seismic data, the underlying geology which

gave rise to that seismic". This process aims at reconstructing subsurface features from geophysical measurements such that the model response "fits" the observation with some measure of error (Treitel and Lines, 2001).

Acoustic Impedance (AI) is the product of density (ρ) and P-wave velocity (Vp) of a rock, equation (1):

$$AI = \rho * V_p \tag{1}$$

AI inversion methods transform seismic data into pseudo-acoustic impedance logs (Latimer et al., 2003). Other than P-wave and density information, seismic data also consist of S-wave data, but conventional seismic inversion does not account for Vp/Vs changes in AVO data (Russell, 2005). Failure to account for these may result in inaccurate impedance estimation, especially in reservoirs (Savic et al., 2002).

Elastic Impedance (EI) is the generalization of AI for variable incidence angles (Connolly, 1999, p.438). Connolly added that it also enables one to calibrate and invert non-zero-offset seismic data similar to AI inversion of zero offset data, and that it is a function of P-wave velocity, S-wave velocity, density, and incident angle (θ), equation (2):

$$EI_{(\theta)} = V_p^{(1+\sin^2\theta)} * V_s^{(-8K\sin^2\theta)} * \rho^{(1-4K\sin^2\theta)} \tag{2}$$

where K is a constant that is taken equal to average of $(V_s/V_p)^2$

EI decreases with increasing angle, compared to AI at normal incidence as shown in figure 4.1. Veeken (2007) pointed out that EI inversion exploits AVO effects on angle stacks and that the far offsets often gives more details on the fluid content compared to the near stack.

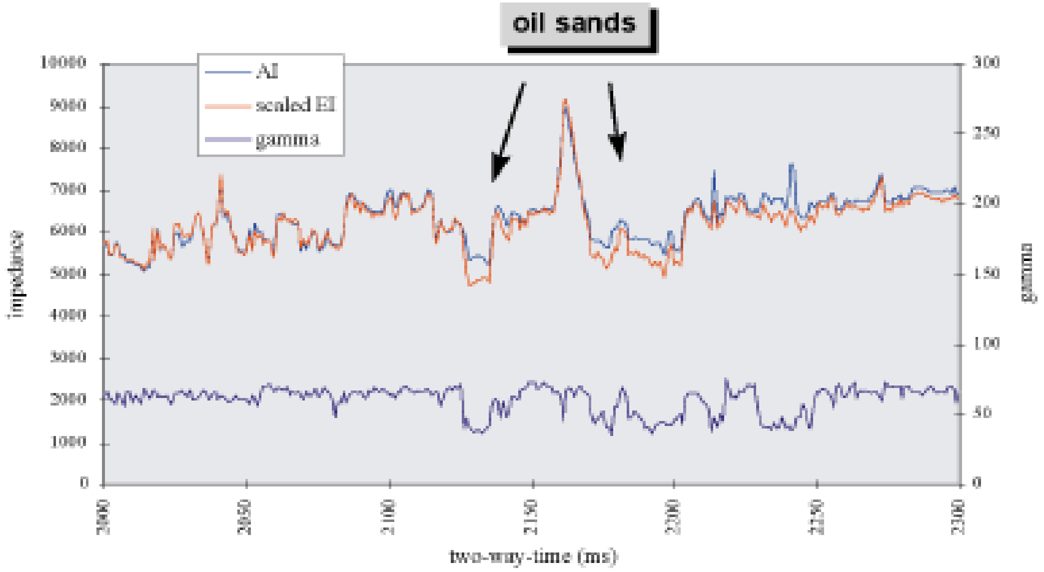

Figure 4.1: Comparison of AI (0°) and EI (30°) curves from a well. The EI shows anomalously low values at areas with hydrocarbon (from Connolly, 1999).

Most inversion process involves the integration of low-frequency model information from well data with higher frequencies from the seismic (Fig. 4.2), aimed at obtaining a high-resolution impedance profile from band-limited seismic data, where the low frequencies provide a correct geological setting and are also necessary to calibrate the seismic information (Li, 2001; Pendrel and van Riel, 2000). To obtain absolute impedance, one requires low-frequency *a prior* information, whereas the relative impedance inversion does not require an initial model (Francis, 2002; Pendrel and van Riel, 2000).

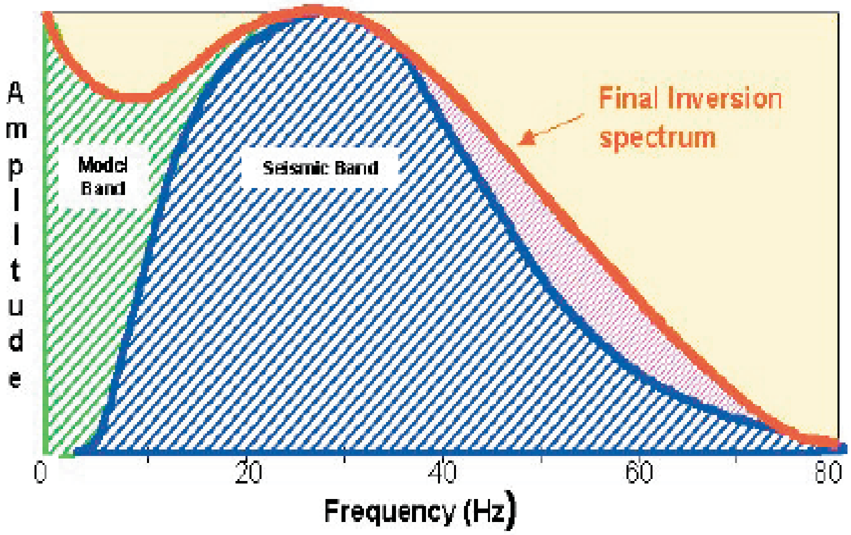

Figure 4.2: Final inversion spectrum composed of the model and seismic band (from Pendrel and van Riel, 2000).

4.1.1 Benefits of impedance data

As discussed by Veeken (2007), Latimer et al. (2003), Pendrel and van Riel (2000), and Savic et al. (2000), the benefits of impedance data are listed below:

- Unlike seismic data, which is an interface property, AI is a rock property and it is presented as geologic layers.
- It contains essential data from the log (not applicable to relative impedance inversion) and all information from the seismic. It also gets rid of the complexities such as false stratigraphy caused by wavelet side lobes.
- It is closely related to lithology and reservoir characteristics such as, porosity, pore fluid, and hydrocarbon saturation.
- As a result of the broader bandwidth of the impedance data, vertical resolution is maximized, while wavelet tuning effect is reduced.

4.2 Acoustic impedance inversion methods

Francis (2002) stated that most impedance inversion methods are deterministic, as they are based on minimizing the difference between the seismic trace and the convolution of the solution of the inversion with the estimated wavelet. In this research, four inversion methods: model-based AI, sparse-spike AI, band-limited AI and high-resolution band-limited AI inversion are applied on the near-angle stack. Comparisons of these are made to ascertain the sensitivity of each method to reservoir fluid, dependence of inversion results on the initial model, and reliability of inversion results.

4.2.1 Model-based inversion

Model-based inversion makes use of an initial geologic model, based on the impedance data (derived for example from interpolation of P-wave sonic and density logs), structural information (interpreted seismic horizons to guide the interpolation of the initial model), and wavelet extracted from well location after correlation with near-angle stack (Fig. 4.3). The initial model (Fig. 4.4) is derived from wells HA-1 and HA-4. Using this model and the extracted average wavelet (Fig. 4.5), a synthetic trace is calculated and compared with the actual seismic data (Fig. 4.6) to calculate the error or misfit between them (objective function). The model is then modified iteratively to minimize the error until the inversion converges, i.e. a reasonable solution or an acceptable match is obtained (Russell, 2005; Sen, 2006; Shrestha, 2008). The inversion process described above is as shown in figure 4.7.

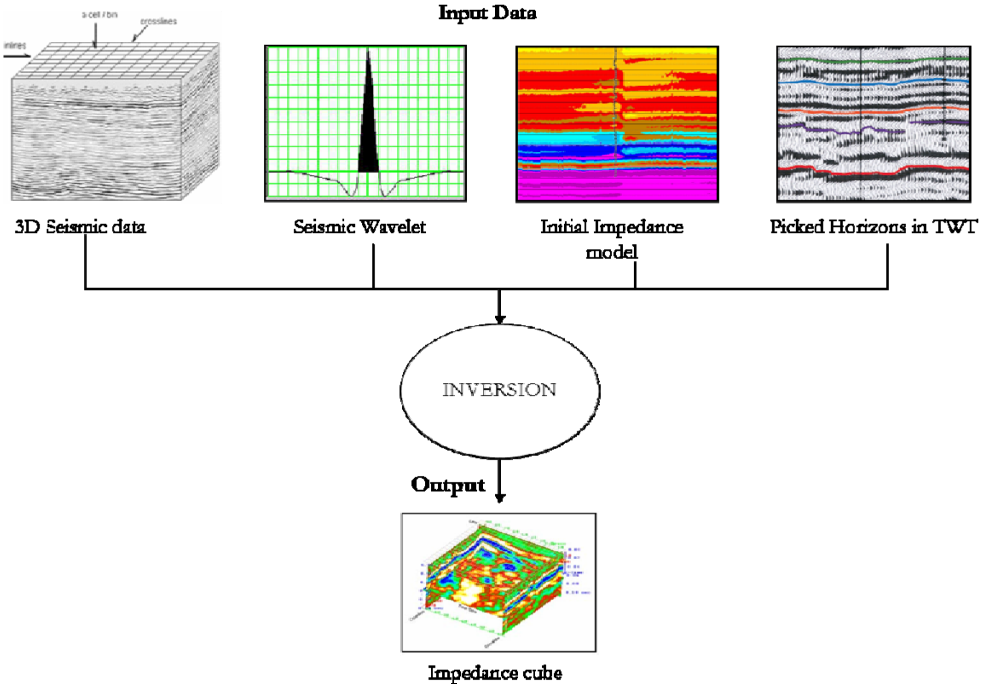

Figure 4.3: Input to inversion process (modified from Veeken, 2007)

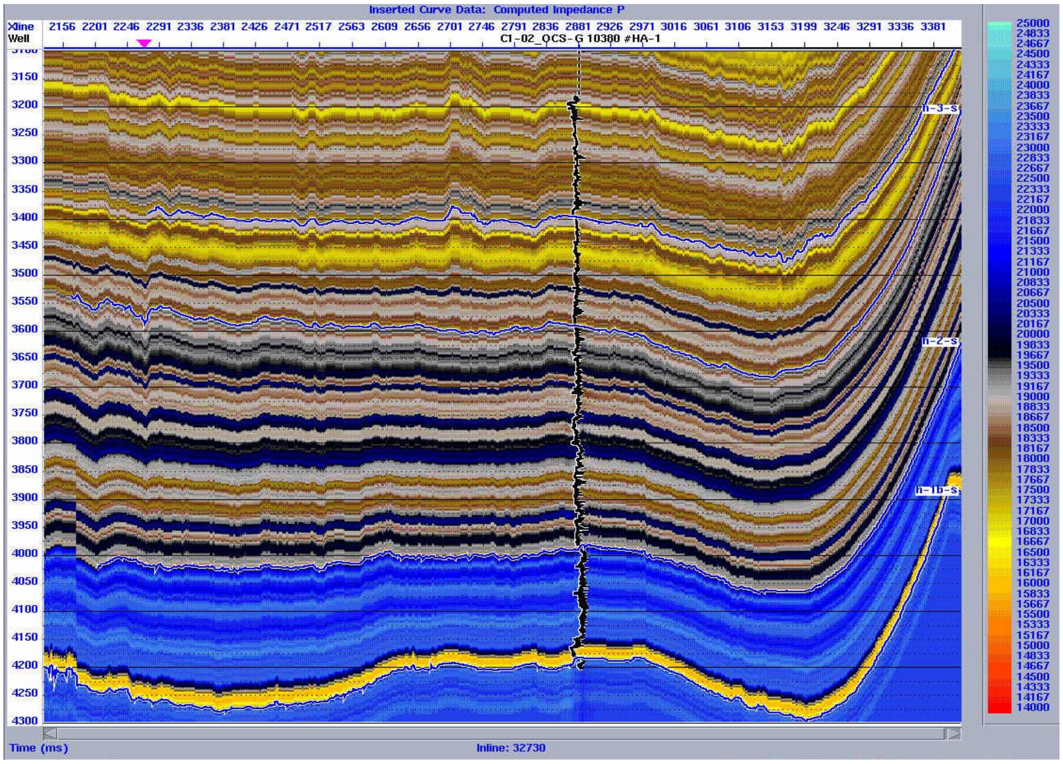

Figure 4.4: Unfiltered initial model derived from wells HA-1 and HA-4 containing all frequencies showing gamma-ray log from HA-1.

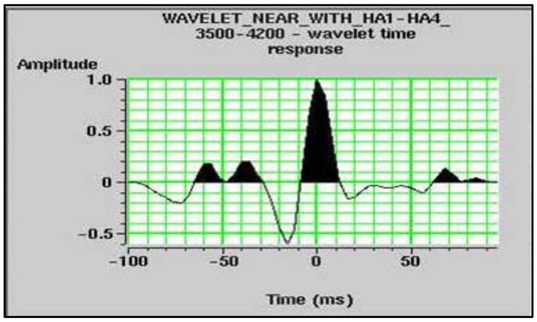

Figure 4.5: Extracted average wavelet from both wells used in inversion.

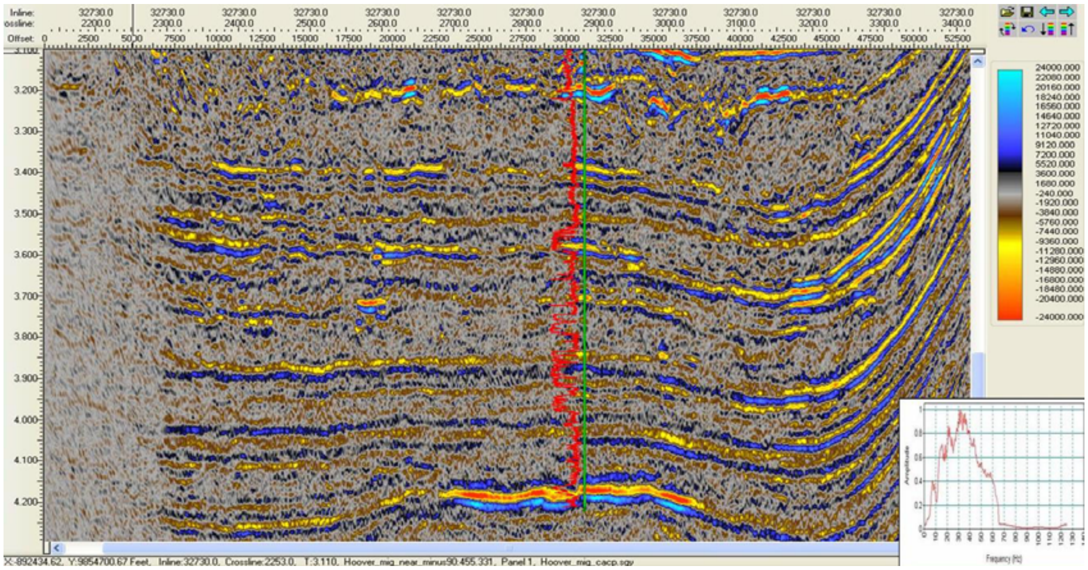

Figure 4.6: Near-angle stacked seismic data. Inset: bottom right (band-limited frequency spectrum of input seismic lacking low frequencies).

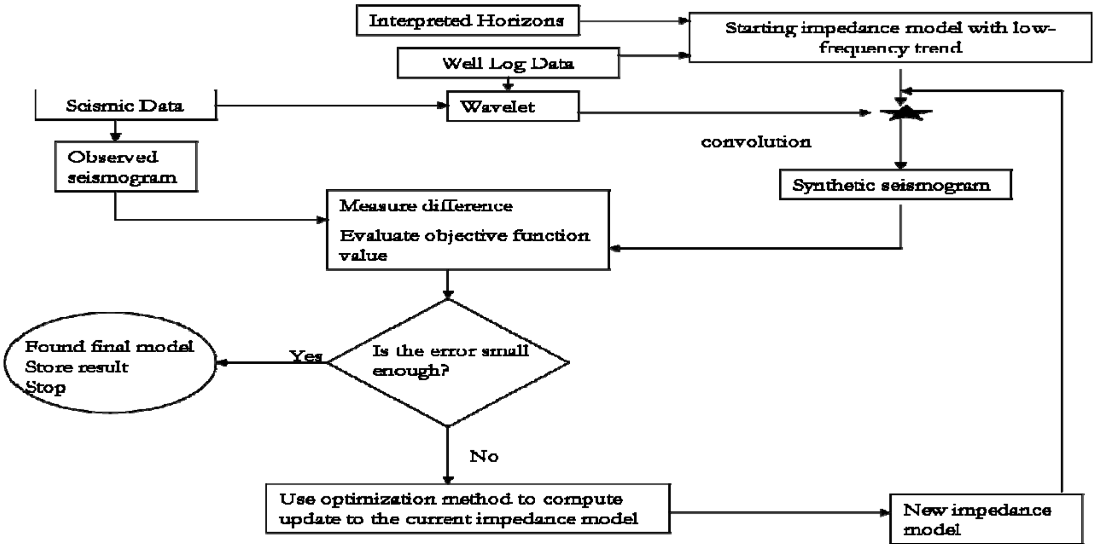

Figure 4.7: Impedance inversion flowchart (modified from Sen, 2006).

Russell (2005) had pointed out that in model-based inversion, the seismic does not have to be zero phase as long as the wavelet used in inversion is of the same phase as the seismic. He also adds that artifacts in the low-frequency model tend to appear in the inversion results. In order to avoid undue influence on the final inversion result by the initial model, a high-cut filtered initial model (10 Hz) (Fig. 4.8) is used for inversion.

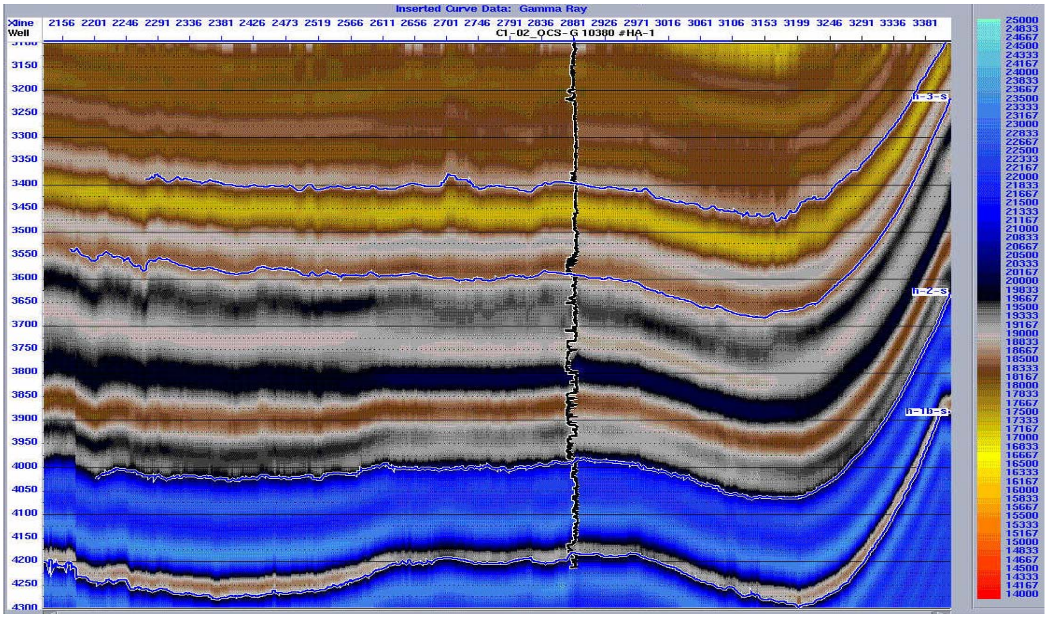

Figure 4.8: Filtered initial model for AI inversion, showing gamma-ray log from HA-1.

4.2.1.1 Inversion parameters and results for the Hoover Field

Hoover field inversion is carried out with the following parameters: sampling frequency, 10 Hz; number of iterations, 15; constraints, 25 % upper and lower limit (50 % change in impedance); and sample rate and block size, 4 ms. Inversion results show that the reservoir sands at about 4200 ms are indicated by low impedance relative to brine sands and encasing shales (Fig. 4.9). In figure 4.10, the post-inversion validation plot, track 1 shows the correlation between original impedance log and inverted result (0.7096); track 2 shows the error between the impedance logs and inverted result (1625); track 3 shows the correlation between the synthetic trace generated from inversion result and the original seismic (0.9961); and track 4 shows the error between the synthetic and seismic trace (0.0896).

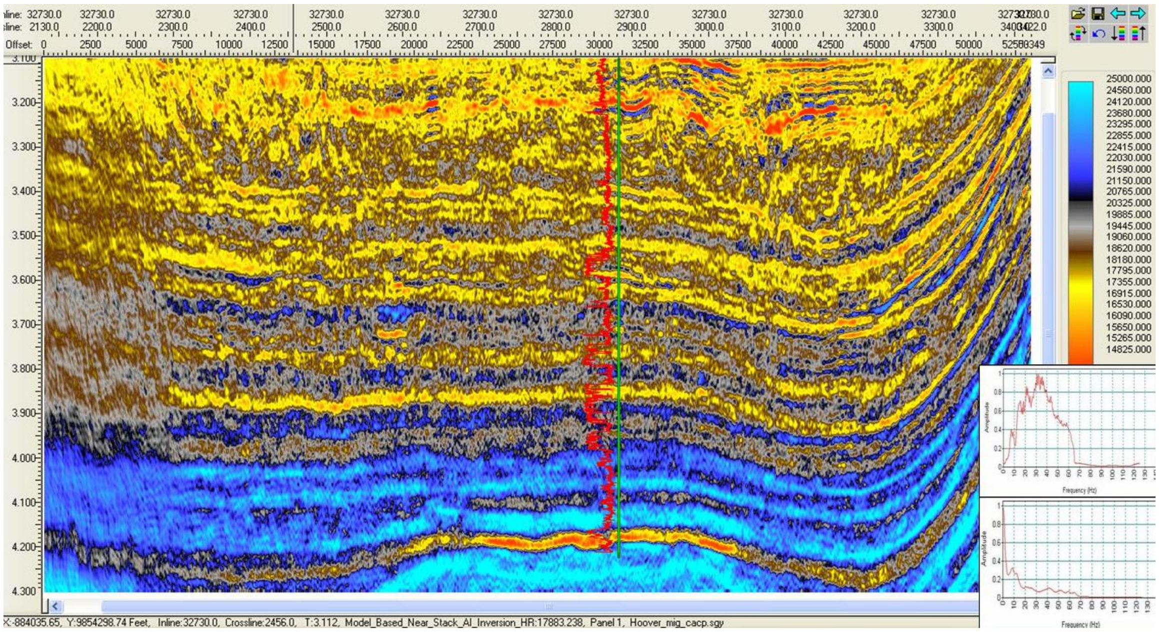

X:-884035.65, Y:9854298.74 Feet, Inline:32730.0, Crossline:2456.0, T:3.112, Model_Based_Near_Stack_AI_Inversion_HR:17883.238, Panel 1, Hoover_mig_cacp.sgy

Figure 4.9: Model-based inversion result from sample rate of 4ms, 15 iterations and 50 % impedance constraint. Inset include: Center (gamma-ray log), top right (frequency spectrum of input seismic lacking low frequencies) and bottom right (frequency spectrum of impedance volume richer in low frequencies).

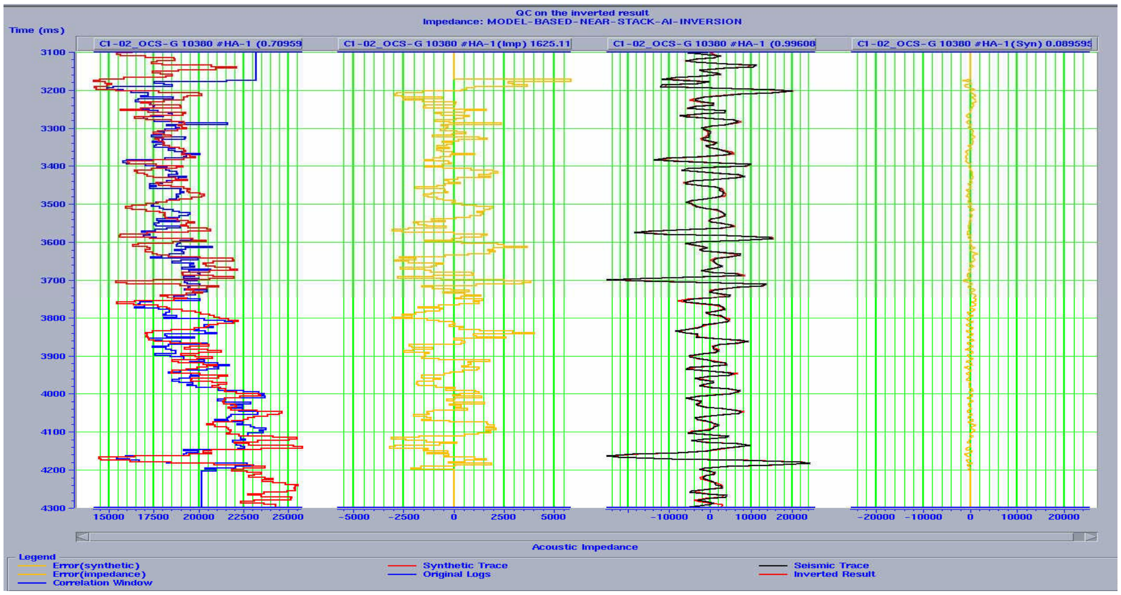

Figure 4.10: Model-based post-inversion validation plot of HA-1. Track 1 (correlation between original impedance log (blue) and inverted result (red)); track 2 (impedance error in yellow); track 3 (correlation between the synthetic trace and the original seismic) and track 4 (synthetic error in yellow).

4.2.2 Band-limited inversion

This is described by Russell (2005) as the earliest and simplest form of inversion whose output has the same bandwidth as the input data. The inversion process involves the derivation of low-frequency impedance model from logs, inversion of seismic traces using the recursive equation (3), and finally adding the low-frequency model to inverted traces (Fig. 4.11). Based on the knowledge of the impedance of a given layer or the shallowest layer, the impedance of the successively deeper layers can be derived using the recursive equation (3) (Russell, 2005; Sen, 2006). This method requires that spherical spreading and transmission losses are completely removed and that input seismic data must be zero phase (Russell, 2005)

$$Z_{pi+1} = Z_i * \left[1 + r_{pi}\right] \Big/ \left[1 - r_{pi}\right] \tag{3}$$

Z_p is acoustic impedance and r_{pi} is the zero offset reflection coefficient of P-wave.

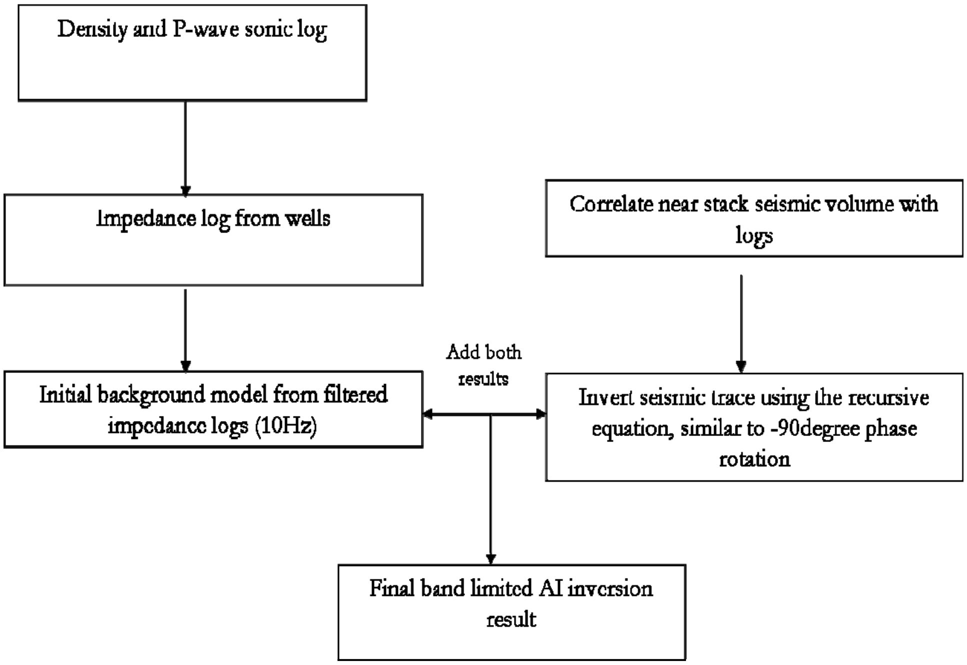

Figure 4.11: Band-limited AI-inversion flow chart (modified from Russell, 2005).

4.2.2.1 Inversion parameters and results

Band-limited inversion result (Fig. 4.12), also shows that the reservoir sand at about 4200 ms has low-impedance relative to brine sands and encasing shales. The AI inversion is smoother and has less detail compared to the model-based inversion. The post-inversion validation plot (Fig. 4.13) shows a correlation of 0.7724 and impedance error of 1282, which is much lower than for model based inversion. This is probably because the low-frequency model was not involved in the inversion process but was simply added after seismic inversion.

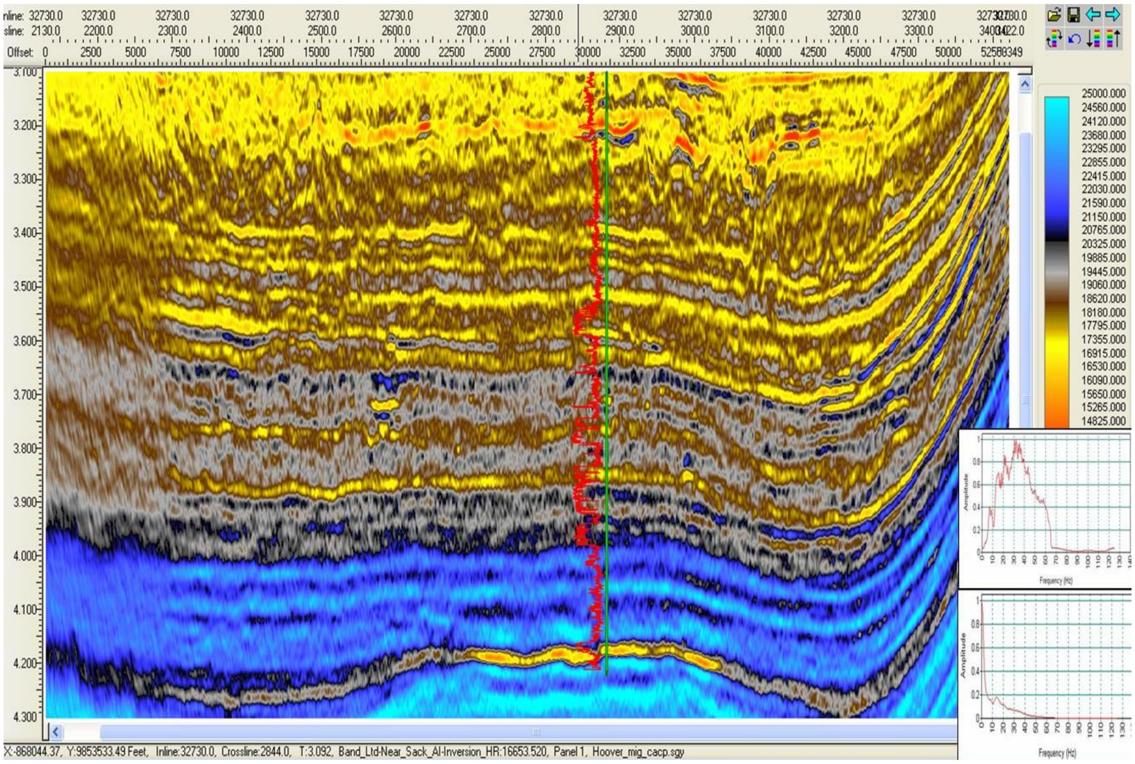

X:-868044.37, Y:9853533.49 Feet, Inline:32730.0, Crossline:2844.0, T:3.092, Band_Ltd-Near_Sack_AI-Inversion_HR:16653.520, Panel 1, Hoover_mig_cacp.sgy

Figure 4.12: Band-limited AI inversion result. Inset include: center (gamma-ray log), top right (frequency spectrum of input seismic which lacks low frequencies) and bottom right (frequency spectrum of impedance volume richer in low frequencies).

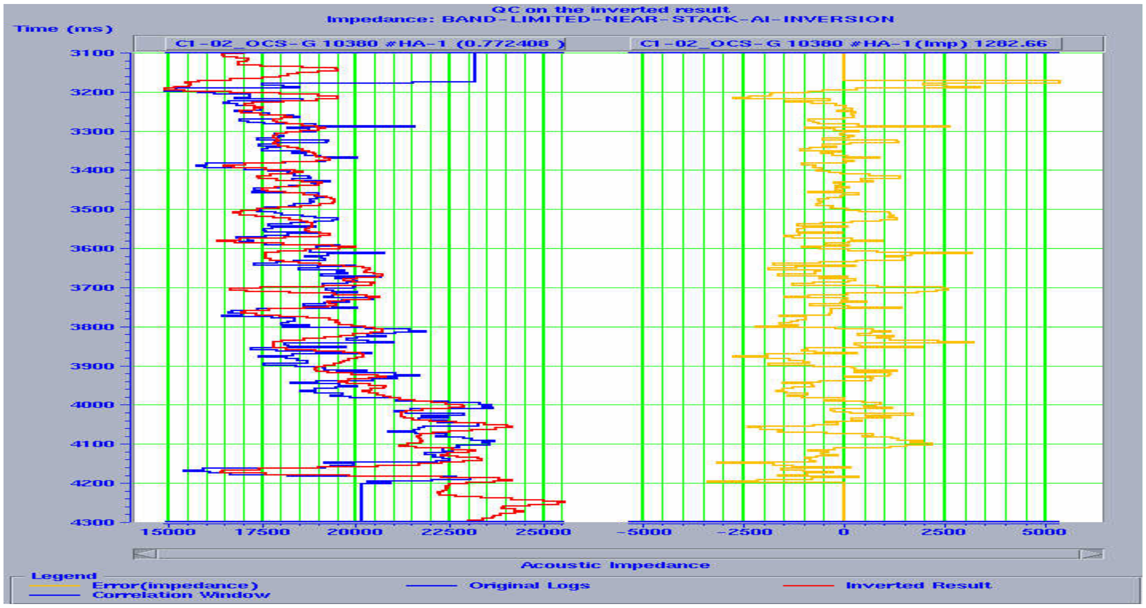

Figure 4.13: Band-limited AI post inversion validation plot for HA-1. Track 1 (correlation between original impedance log (blue) and inverted result (red)) and track 2 (impedance error in yellow).

4.2.3 Sparse-spike inversion:

Russell (2005, p.25) stated that "sparse-spike inversion assumes that the actual reflectivity can be thought of as a series of large spikes embedded in a background of small spikes in which only the large spikes are assumed to be meaningful". With the aid of the model-based inversion algorithm, it attempts to output the simplest possible model consistent with the seismic data, and as a result, gives rise to fewer events than are known to be geologically true (Russell, 2005; Veeken, 2007).

4.2.3.1 Inversion parameters and results

Maximum constraint frequency (MCF) determines the range of frequencies taken from the initial model during inversion and, specifying a wide range of frequencies, increases the influence of the initial model on the final inversion results (Russell, 2005). Russell (2005) also adds that sparseness determines the amount of high frequencies that would be included in the inversion to make it sparse. Li (2001) observes that although the number of spikes in the inverted results reduces with a reduction in the value of sparseness, the value of the correlation coefficient between the synthetic and the seismic does not change.

Inversion is carried out with the following parameters: MCF of 10 Hz, sparseness of 100 %, and window length of 128 samples. Inversion results and analyses are shown in figures 4.14 and 4.15. In order to test the effects of variation in sparseness, one more inversion is carried out using sparseness of 50 %, MCF of 10 Hz, and window length of 128 samples. Inversion results and post-inversion analyses are also shown in figures 4.16 and 4.17.

Similar to model-based and band-limited inversion results, the reservoir is a low-impedance zone. The post-inversion validation plots show that inversion carried out with sparseness of 100 % has impedance error of 1330 (correlation of 0.7913), and synthetic error of 0.2829 (correlation of 0.9602). On the other hand, impedance error of 1406 (correlation of 0.7712) and synthetic error of 0.2828 (correlation of 0.9601) are obtained for same well with 50 % sparseness. Inversion with a reduced sparseness yields an increase in impedance error, while the synthetic error remains unaffected. This is because the inversion always honors the information in the bandwidth of the seismic (Li, 2001).

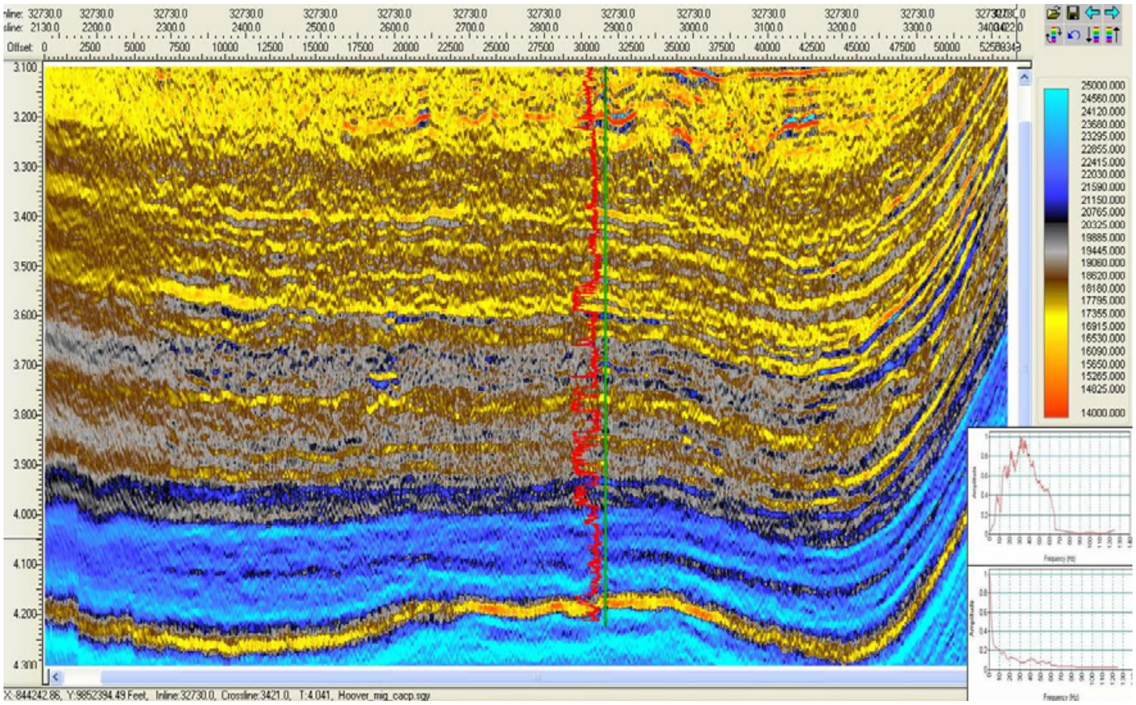

Figure 4.14: Sparse-spike AI inversion result at 100 % sparseness. Inset include: center (gamma ray log), top right (frequency spectrum of input seismic which lacks low frequencies), and bottom right (frequency spectrum of impedance volume richer in low frequencies).

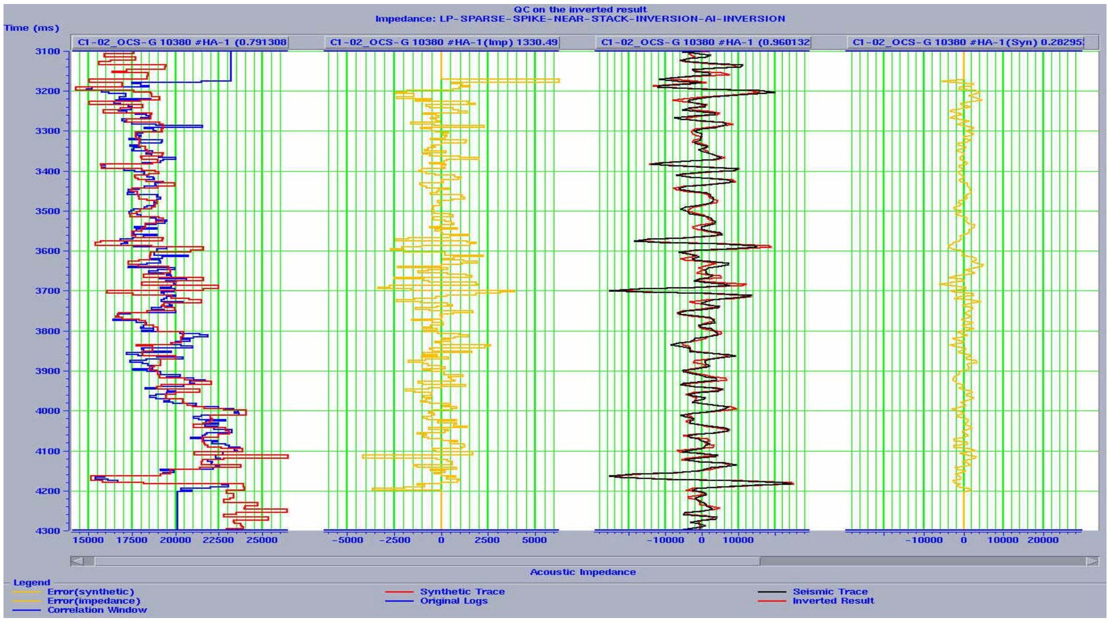

Figure 4.15: Post-inversion validation plot for HA-1 at 100 % sparseness. Track 1 (correlation between original impedance log (blue) and inverted result (red)); track 2 (impedance error in yellow); track 3 (correlation between the synthetic trace and the original seismic) and track 4 (synthetic error in yellow).

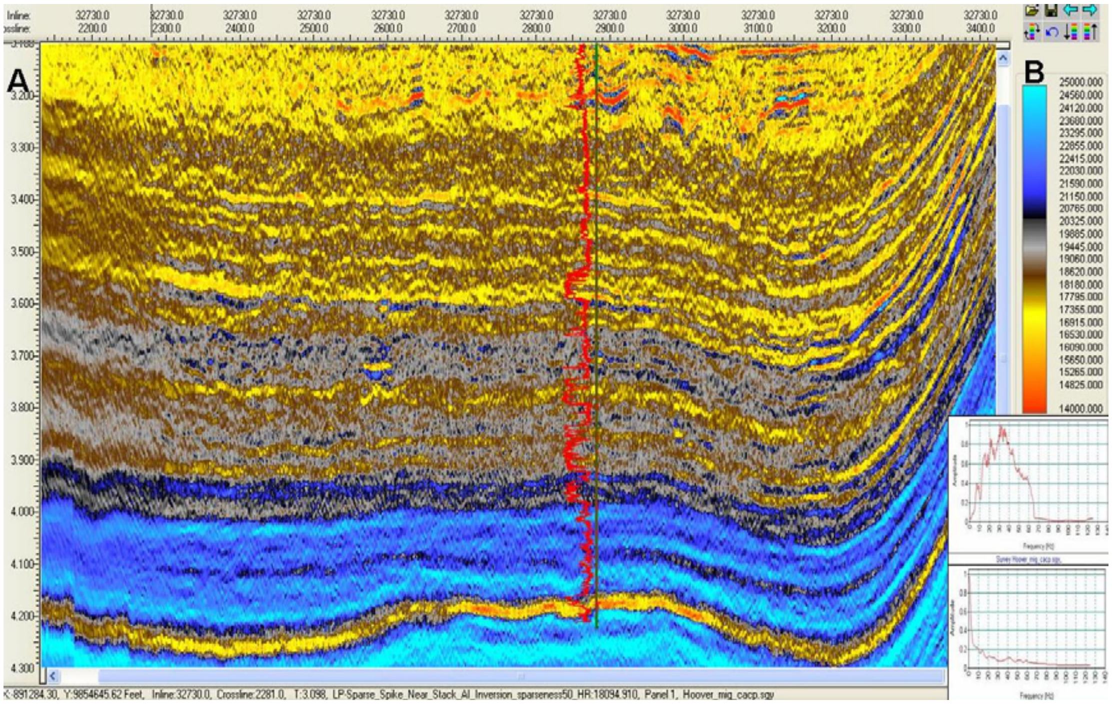

Figure 4.16: Sparse-spike AI inversion result at 50 % sparseness. Inset include: center (gamma ray log), top right (frequency spectrum of input seismic which lacks low frequencies), and bottom right (frequency spectrum of impedance volume richer in low frequencies).

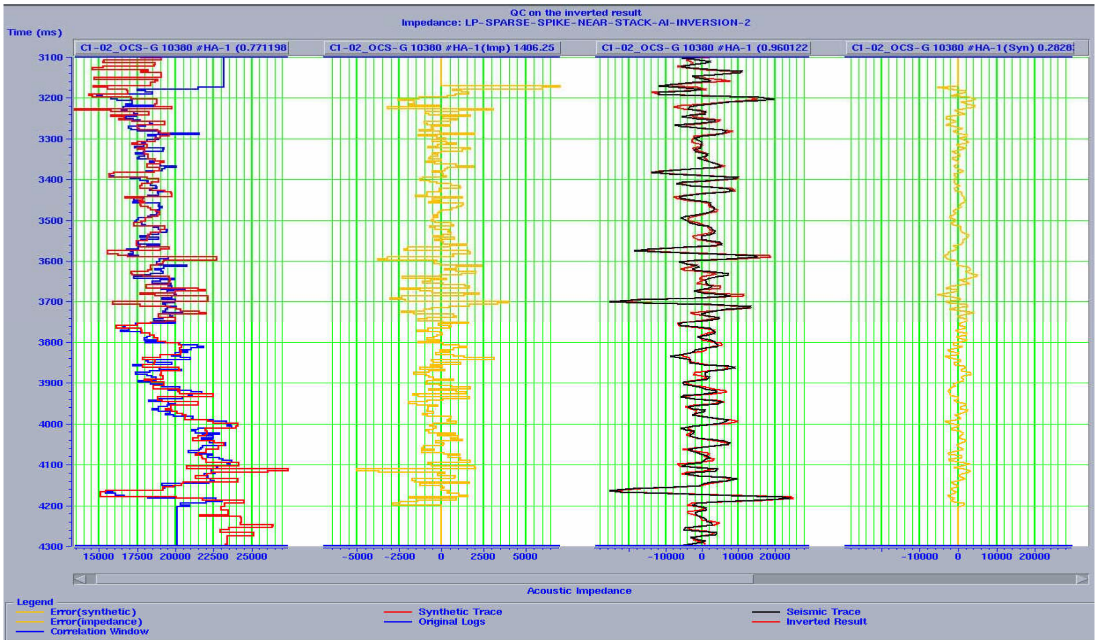

Figure 4.17: Post-inversion validation plot for HA-1 at 50 % sparseness. Track 1 (correlation between original impedance log (blue) and inverted result (red)); track 2 (impedance error in yellow); track 3 (correlation between the synthetic trace and the original seismic) and track 4 (synthetic error in yellow).

4.2.4. High-resolution band-limited impedance inversion

This is an inversion method that involves the integration of inverted reflectivity derived from the application of spectral decomposition on post-stack seismic data (Portnaguine and Castagna, 2005). A commercial application of this method, ThinMAN, is applied on both near- and far-stacked seismic volumes to get inverted impedance volumes which show the contrast in impedance between a unit and its underlying/overlying layer (i.e. relative impedance). This does not require an initial model or interpreted horizon(s), and it can be performed without well calibration (Chopra et al., 2006). It also makes use of a set of time- and space-varying wavelets, unlike the constant wavelet used in model based and sparse-spike inversions. The inversion workflow is as shown in figure 4.18.

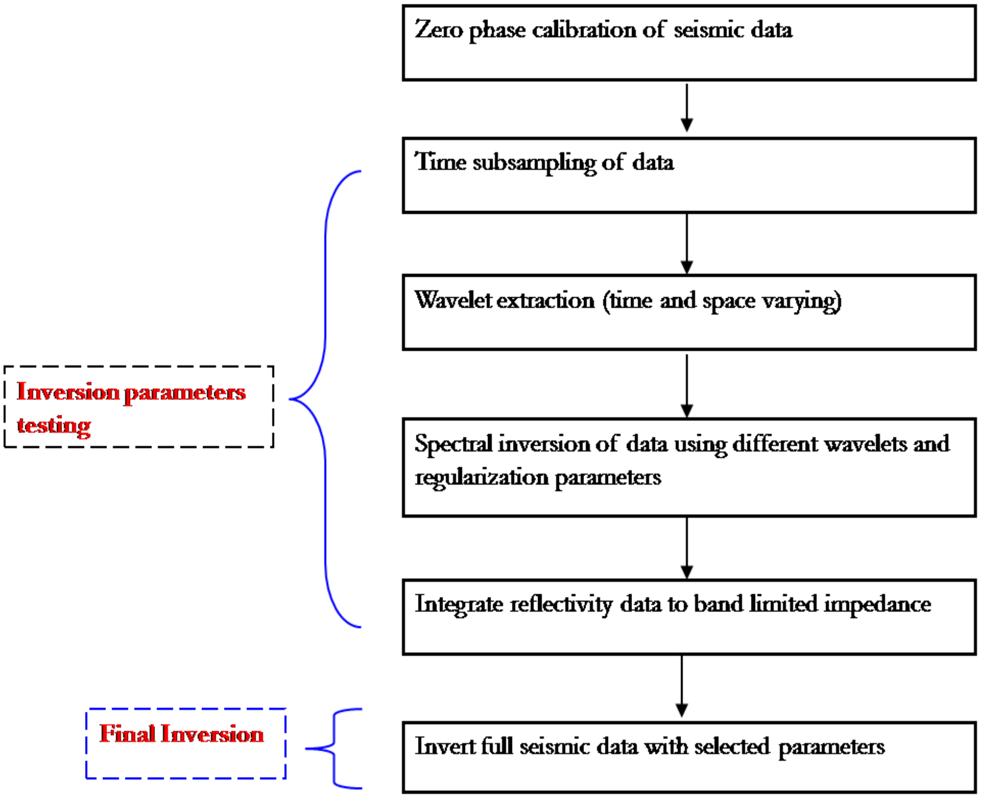

Figure 4.18: High-resolution band-limited impedance inversion work flow.

4.2.4.1 Inversion parameters and results

The inversion process starts with the calibration of seismic data to zero phase, as discussed in section 3.1.4. Spectral inversion leads to broadening of the frequency bandwidth, which would not be achieved if the sampling frequency is greater than the nyquist frequency. To make room for the expected increase, the sample rate of the seismic data is reduced from 4 ms to 1 ms, i.e. a nyquist frequency of 125 Hz to 500 Hz.

One of the factors that affects the quality of inversion is the wavelet. The more representative the wavelet is of the seismic volume, the better the inversion results. In this inversion, a set of time- and space-varying wavelets is extracted statistically from the seismic. The left panel of figure 4.19, shows the time domain of an extracted wavelet with a spike (red) and side lobes (light blue), while the right panel shows the vertical variation of frequency at a given location.

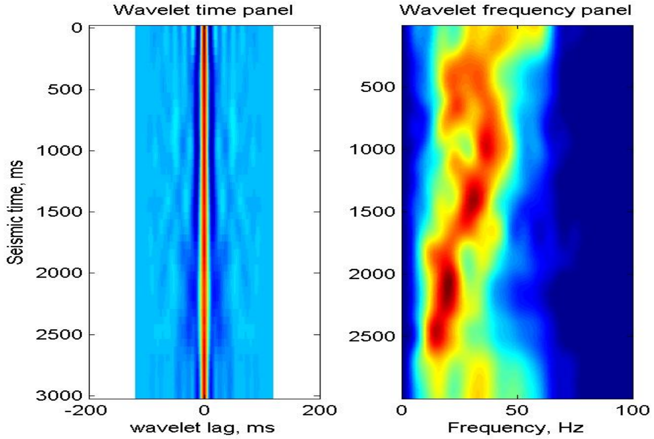

Figure 4.19: An example of an extracted wavelet at a location used for inversion shown in the time domain (left) and frequency domain (right).

Based on the extracted zero-phase wavelet, a series of inversions is carried out to test different regularization parameters, alpha (α), which increases/decreases the stability of the solution, i.e. its sensitivity/insensitivity to small errors in the data (Sen, 2006). Low α values allow one to see subtle structures, whereas high α values smooth the data and get rid of subtle structures. Also, very low α results in a noisy output. The reflectivity volume (Fig. 4.20) is then integrated to get a band-limited impedance volume which is not influenced by the existing well information, unlike the other inversion methods discussed above.

Parameters used in the final inversion includes: ½ wavelet length (WL2) of 120 ms, number of intervals (Nt) of 50 for wavelet extraction, and alpha of 0.5. Because the test was conducted using a time window of 2000 ms to 5000 ms, the wavelet would be extracted every 60 ms i.e. [(5000 – 2000)/50]. The inversion of the near-stacked volume shows low impedance at the prospect and higher impedance in the surrounding shales and water-saturated sands (Fig. 4.21). Although it is richer in higher frequencies than the other inversion methods, it lacks the very low frequencies, which have not been added.

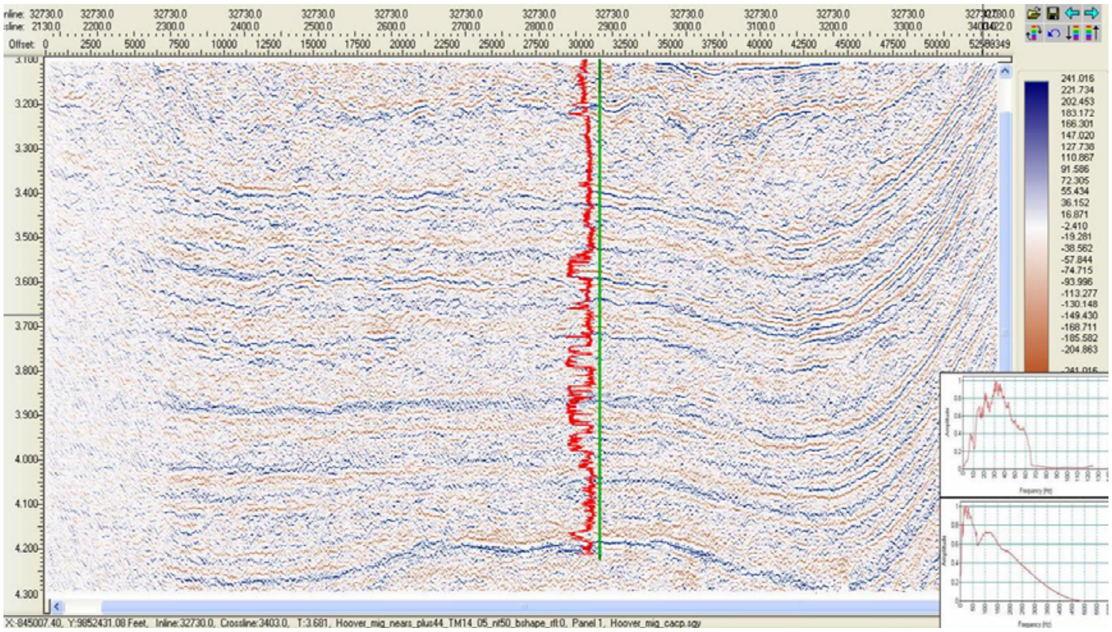

X:845007.40, Y:9852431.08 Feet, Inline:32730.0, Crossline:3403.0, T:3.681, Hoover_mig_nears_plus44_TM14_05_nt50_bshape_rlt0, Panel 1, Hoover_mig_cacp.sgy

Figure 4.20: Spectrally broadened reflectivity volume derived from spectral inversion of near-angle stacked seismic. Inset include: top right (frequency spectrum of input seismic which lacks low frequencies) and bottom right (frequency spectrum of impedance volume richer in higher frequencies but lacking low frequencies).

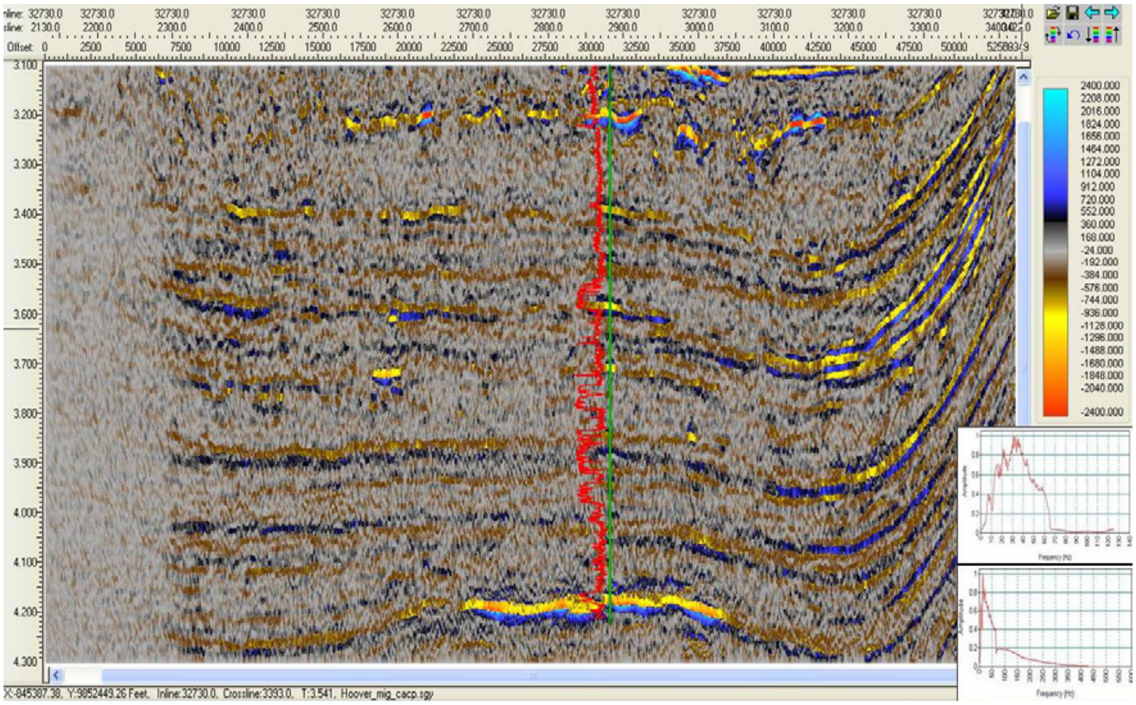

Figure 4.21: Inversion result from high-resolution band-limited impedance inversion of near stack using wavelet with WL2 of 120 ms, time window of 60ms and alpha of 0.5. Inset include: top right (frequency spectrum of input seismic lacking low frequencies) and bottom right (frequency spectrum of impedance volume richer in higher frequencies but lacking low frequencies).

4.3 Elastic impedance inversion

As conventional seismic inversion does not account for amplitude variation with offset, far-angle stacked seismic is inverted (Connolly, 2001). For this purpose, high-resolution band-limited impedance inversion is applied on the far-stacked seismic data.

4.3.1 High-resolution band-limited impedance inversion

Similar to the near-stacked seismic, phase calibration was also carried out on the far-stack prior to inversion. The inversion of far-angle stacked seismic (Fig. 4.22) resulted in a reflectivity volume (Fig. 4.23) which was integrated to a band-limited impedance volume (Fig. 4.24). The impedance volume shows low impedance at the prospect and higher impedance in the surrounding shale and brine-saturated sands. It is observed that fewer units with low impedances are visible.

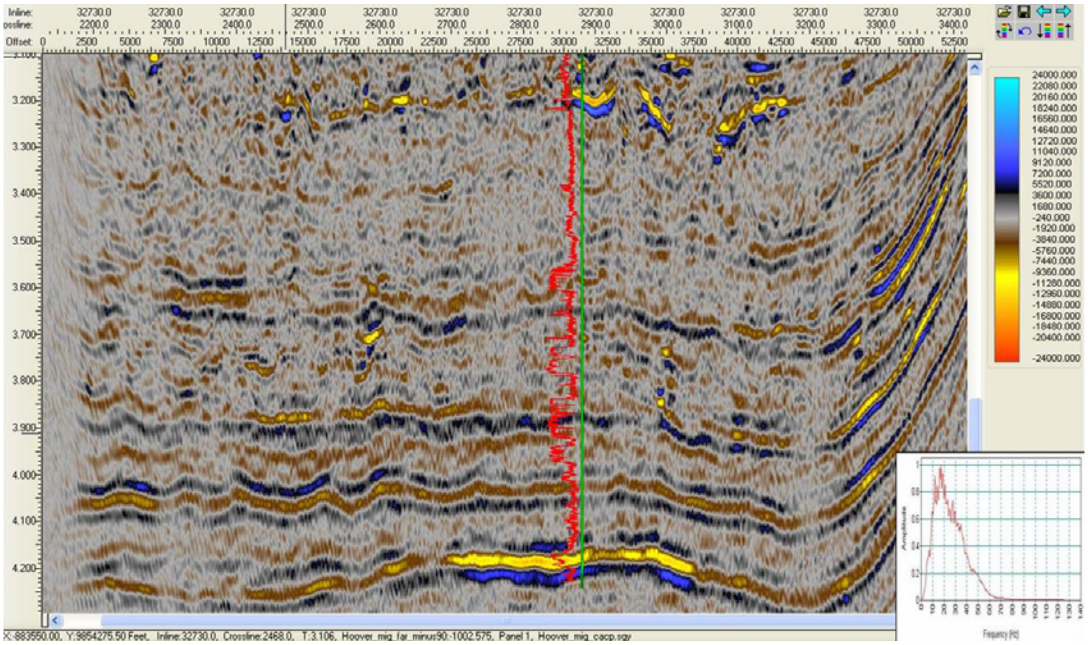

X:883550.00, Y:9854275.50 Feet, Inline:32730.0, Crossline:2468.0, T:3.106, Hoover_mig_far_minus90:-1002.575, Panel 1, Hoover_mig_cacp.sgy

Figure 4.22: Far-angle stacked seismic data. Inset bottom right (band-limited frequency spectrum of input seismic lacking low frequencies).

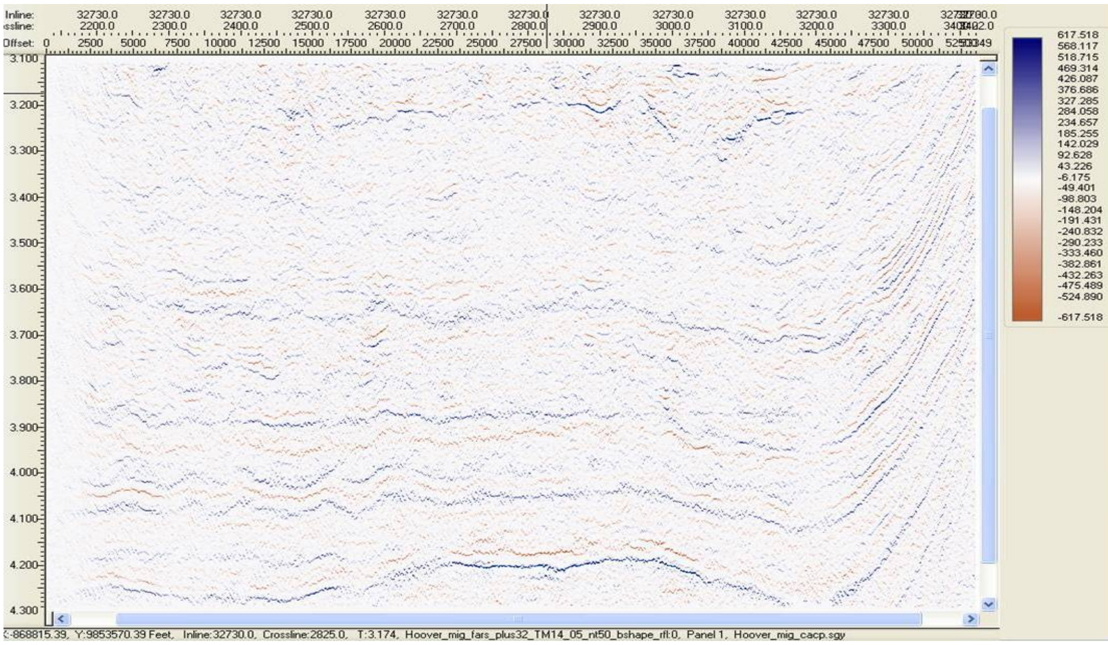

X:-868815.39, Y:9853570.39 Feet, Inline:32730.0, Crossline:2825.0, T:3.174, Hoover_mig_fars_plus32_TM14_05_nt50_bshape_rfl:0, Panel 1, Hoover_mig_cacp.sgy

Figure 4.23: Spectrally broadened reflectivity volume derived from spectral inversion of far-angle stacked seismic.

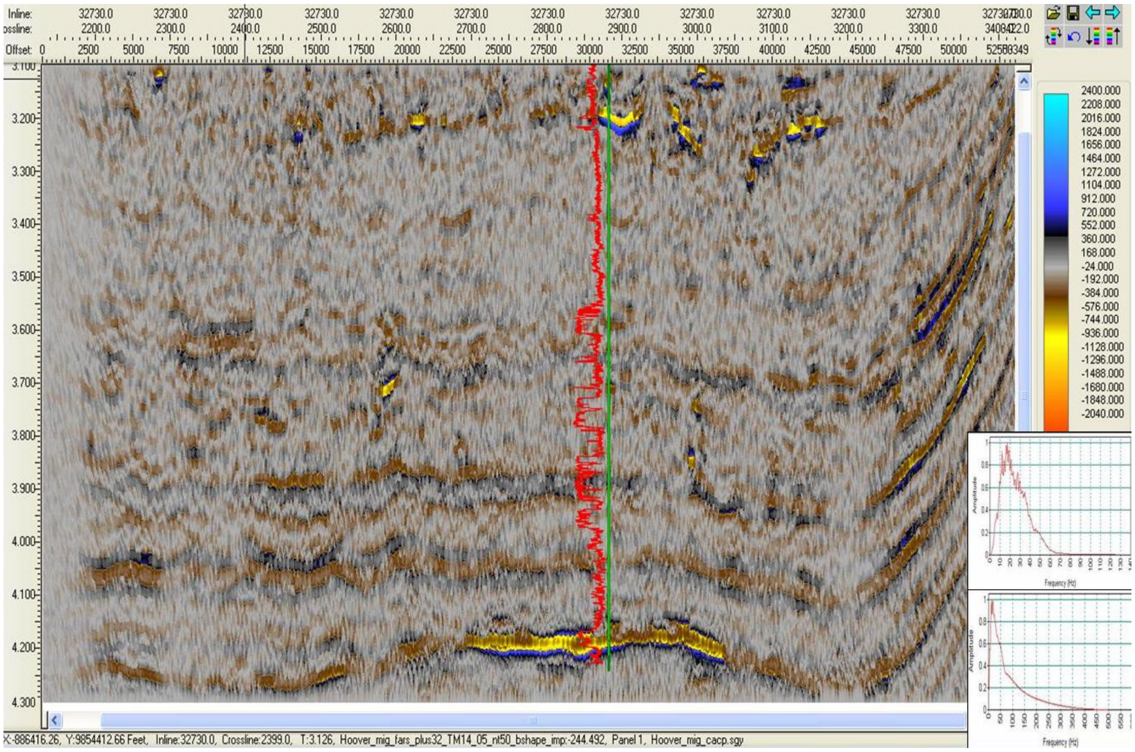

X:-886416.26, Y:9854412.66 Feet, Inline:32730.0, Crossline:2399.0, T:3.126, Hoover_mig_fars_plus32_TM14_05_nt50_bshape_imp:-244.492, Panel 1, Hoover_mig_cacp.sgy

Figure 4.24: Inversion result from band-limited inversion of far stack using wavelet of WL2 of 120ms, time window of 60 ms and alpha of 0.5. Inset include: top right (frequency spectrum of input seismic lacking low frequencies) and bottom right (frequency spectrum of impedance volume richer in higher frequencies but lacking low frequencies).

4.4 Discussions of inversion results

4.4.1 Cross-sections and horizon slices

Both absolute and relative impedance inversion results show sharp contrast between sandstone reservoir and the surrounding shales, as well as varying degrees of contrast between hydrocarbon and non-hydrocarbon saturated portion of the reservoir, depending on the type of inversion. Comparisons of the near- and far-stack relative impedance show fewer numbers of bright amplitudes at far offset. This is a result of the faster decrease in amplitude of shale upon shale and shale upon brine sands than shale upon oil sands, which confirms the AVO gradient analysis plots.

The post-inversion validation plots show that the model-based AI inversion gives the best correlation between the input-seismic and the synthetic-seismic generated after inversion. The band-limited AI inversion gives a better correlation and smaller error between the original log and the inverted result than the model-based case. This is probably because it simply adds the initial model to the inverted traces. Although the sparse-spike AI inversion shows a smaller impedance error, it has a larger synthetic error than the model-based results. This is likely to be caused by its preference of larger spikes for geologic boundaries.

A close up on inline 32730 (Figs. 4.25, 4.26, 4.27, 4.28 and 4.29) shows the distribution of reservoir sands as well as the hydrocarbon-saturated sands. To get a plan view of the reservoir horizon, 30ms window on horizon slices (Figs. 4.30 to 4.34) are taken on these cross sections. Both cross sections and horizon slices show the contrast in impedance between the oil- and brine-saturated reservoir, as well as the heterogeneity of the reservoir, which is more visible in figures 4.33 and 4.34. One observes that although all the inversion methods have a good vertical impedance contrast between the reservoir sands and surrounding shales, the same cannot be said for the horizontal contrast within the reservoir. Sparse-spike inversion produces the least horizontal contrast in impedance. Arbitrary lines from figures 4.35 and 4.37 and their respective cross sections (Fig. 4.36 and 4.38) reveal bright spots away from the main prospect at the north (between crossline 2700 and 3000) and at the west (between inline 32800 and 33300). They are brighter at the near stack and diminish in amplitude on the far stack.

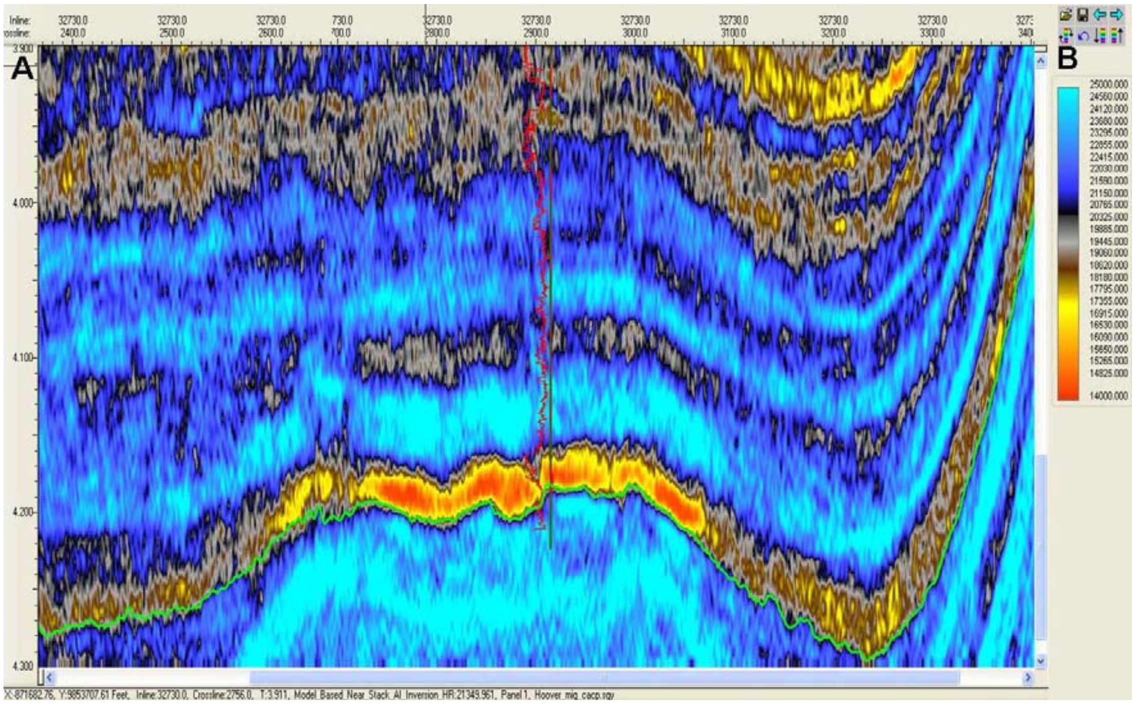

X:871682.76, Y:9853707.61 Feet, Inline:32730.0, Crossline:2756.0, T:3.911, Model Based Near Stack AI Inversion HR:21349.961, Panel 1, Hoover mig cacp.sgy

Figure 4.25: Close up on model-based near-stack AI inversion for cross line 32730 from figure 4.9.

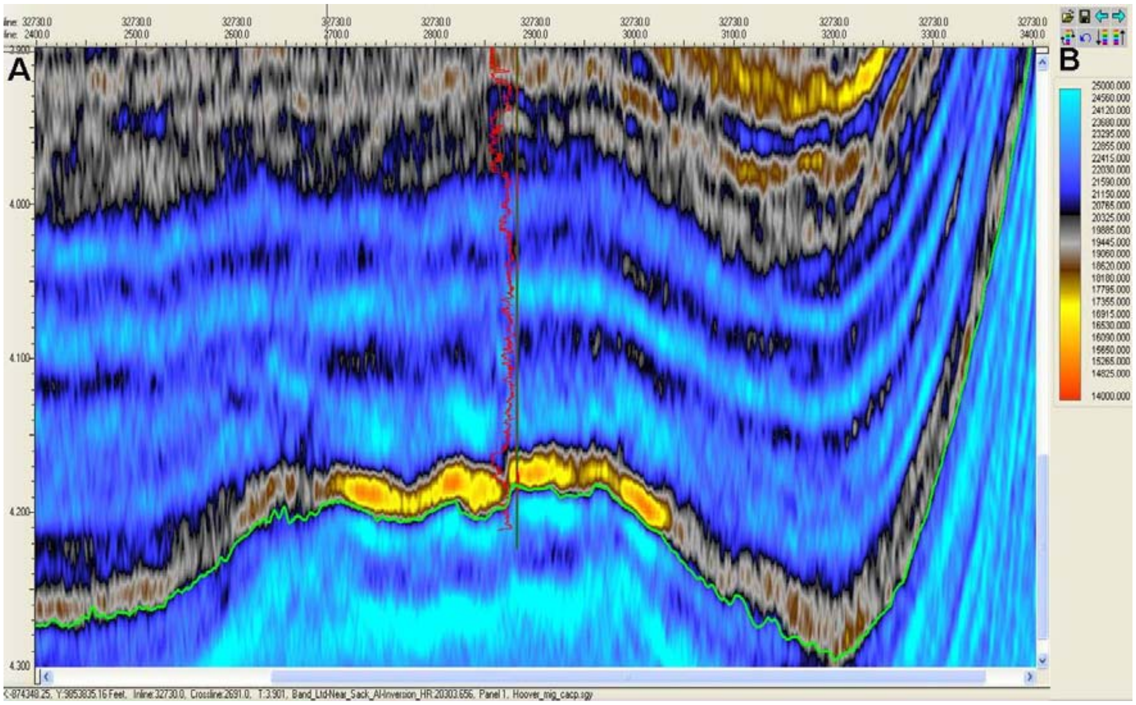

X:874348.25, Y:9853835.16 Feet, Inline:32730.0, Crossline:2691.0, T:3.901, Band_Ltd-Near_Sack_AI-Inversion_HR:20303.656, Panel 1, Hoover_mig_cacp.sgy

Figure 4.26: Close up on band-limited near-stack AI inversion for cross line 32730 from figure 4.12.

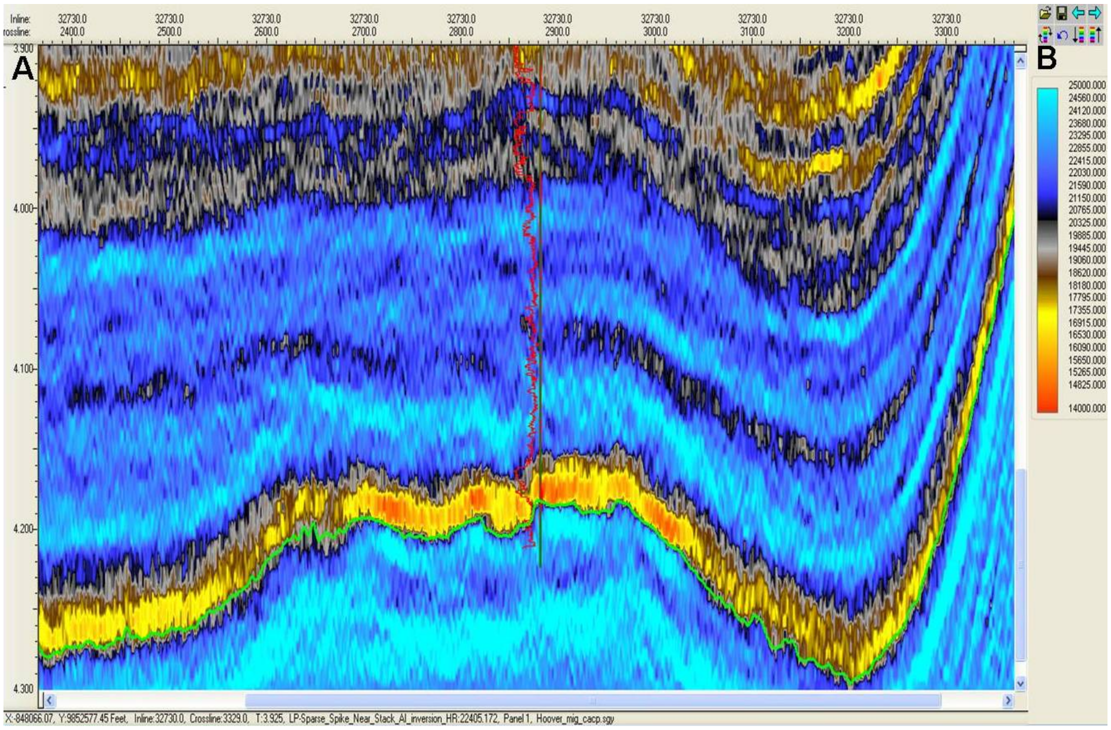

X:-848066.07, Y:9852577.45 Feet, Inline:32730.0, Crossline:3329.0, T:3.925, LP-Sparse_Spike_Near_Stack_AI_inversion_HR:22405.172, Panel 1, Hoover_mig_cacp.sgy

Figure 4.27: Close up on sparse-spike near-stack AI inversion for cross line 32730 from figure 4.14.

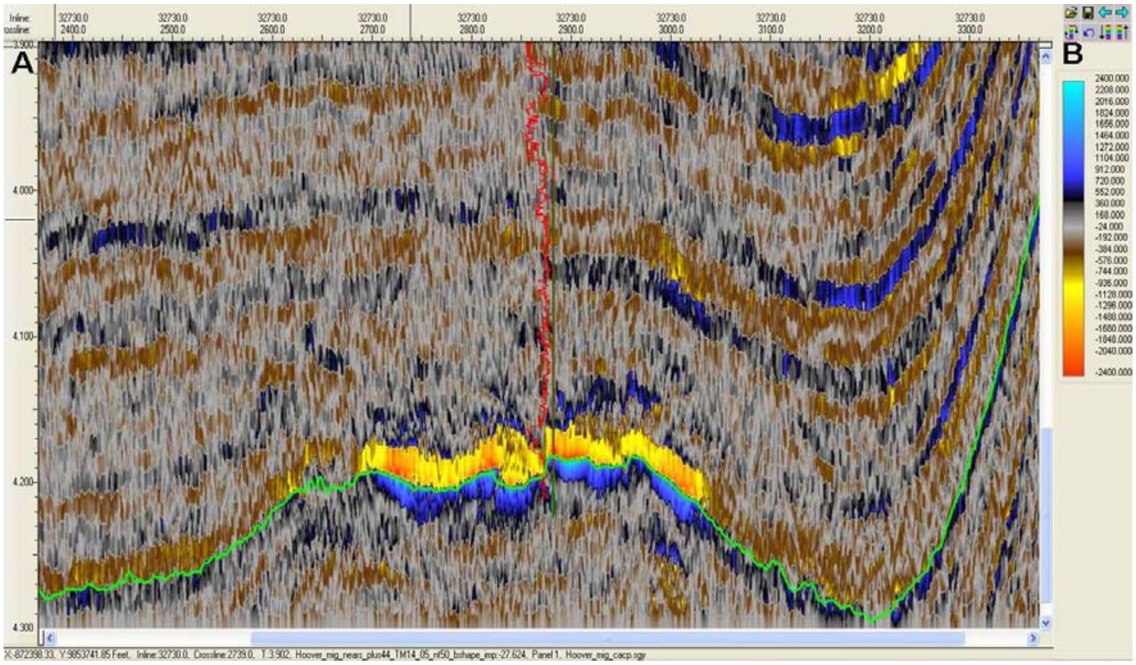

X:-872398.33, Y:9853741.85 Feet, Inline:32730.0, Crossline:2739.0, T:3.902, Hoover_mig_nears_plus44_TM14_05_nf50_bshape_imp:-27.624, Panel 1, Hoover_mig_cacp.sgy

Figure 4.28: Close up on high-resolution band-limited near-stack impedance inversion for cross line 32730 from figure 4.21.

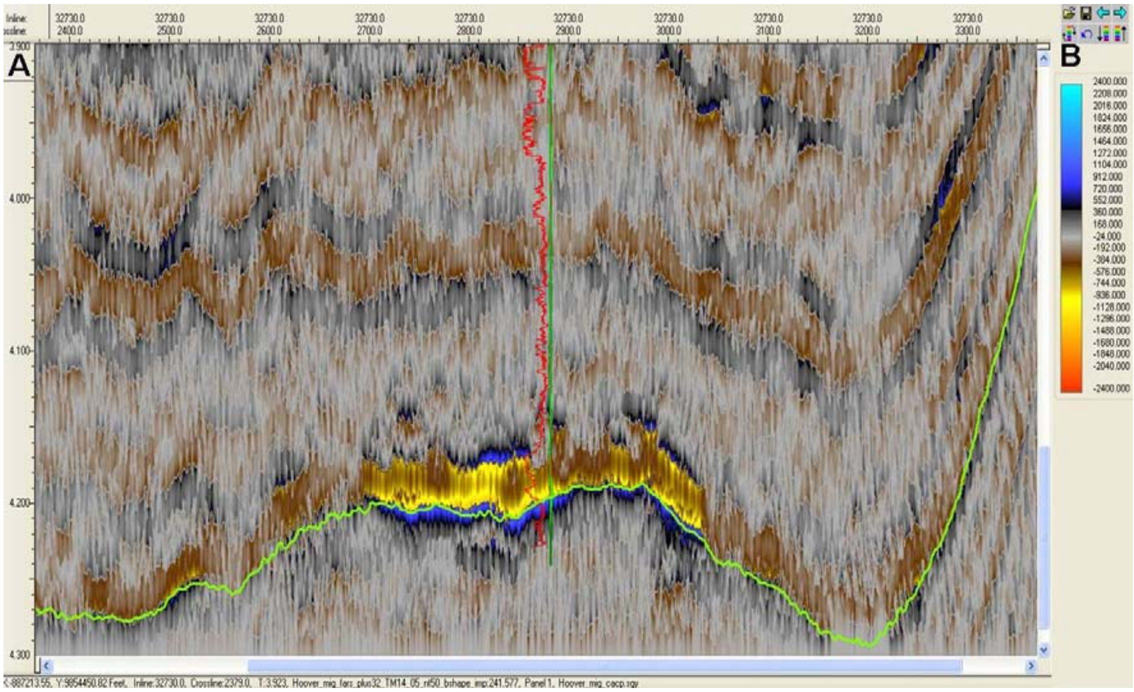

Figure 4.29: Close up on high-resolution band-limited far-stack impedance inversion for cross line 32730 from figure 4.24.

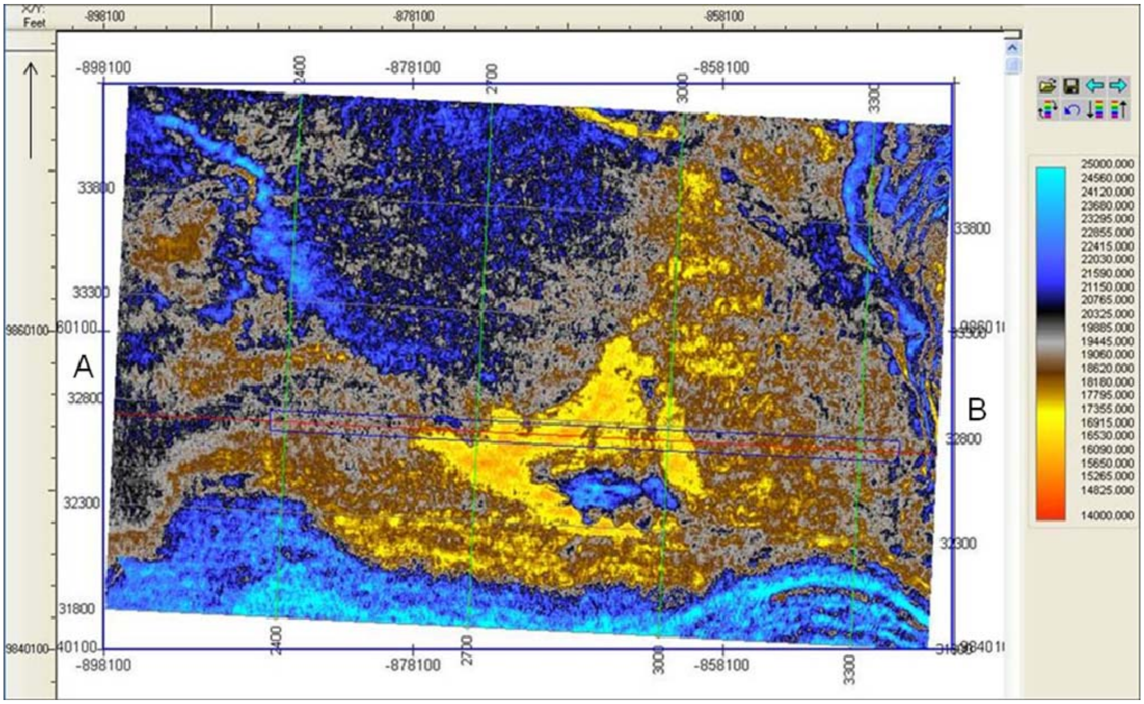

Figure 4.30: Horizon slice on model-based near-stack AI inversion.

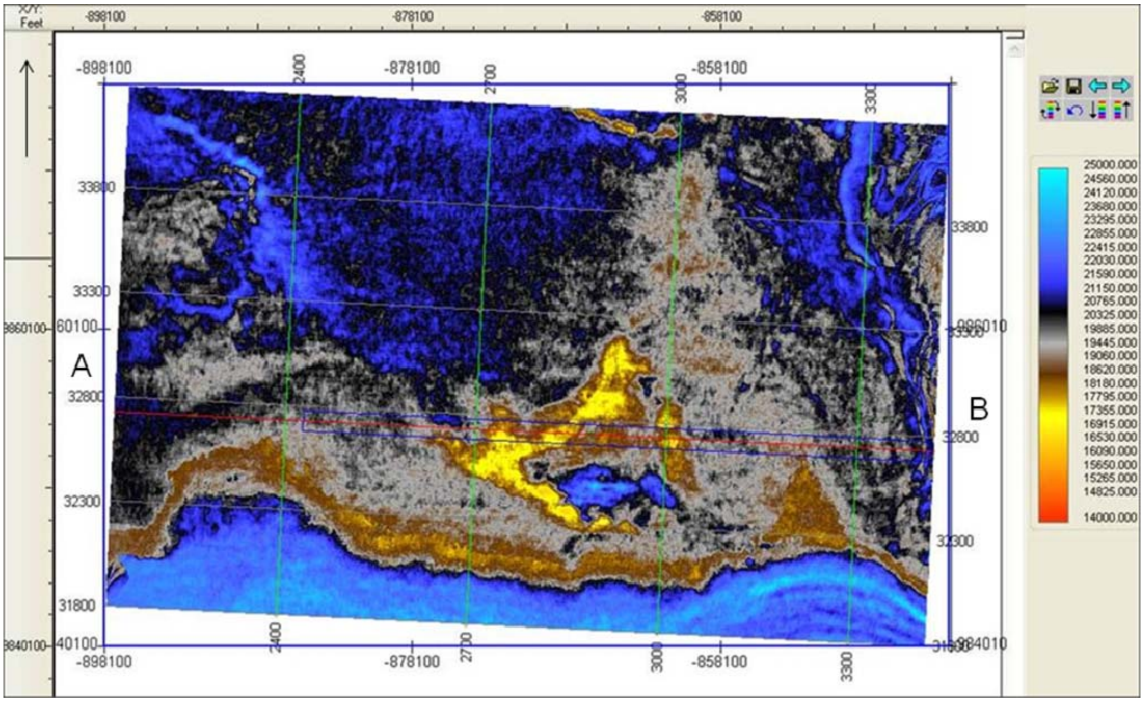

Figure 4.31: Horizon slice on band-limited near-stack AI inversion.

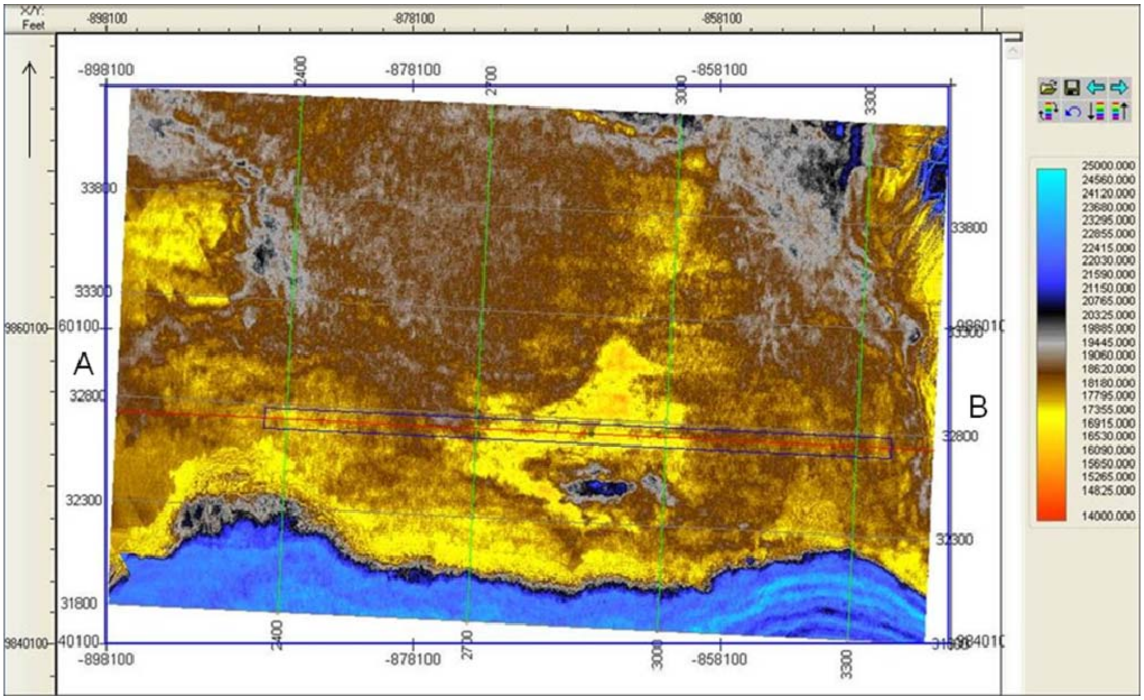

Figure 4.32: Horizon slice on sparse-spike near-stack AI inversion.

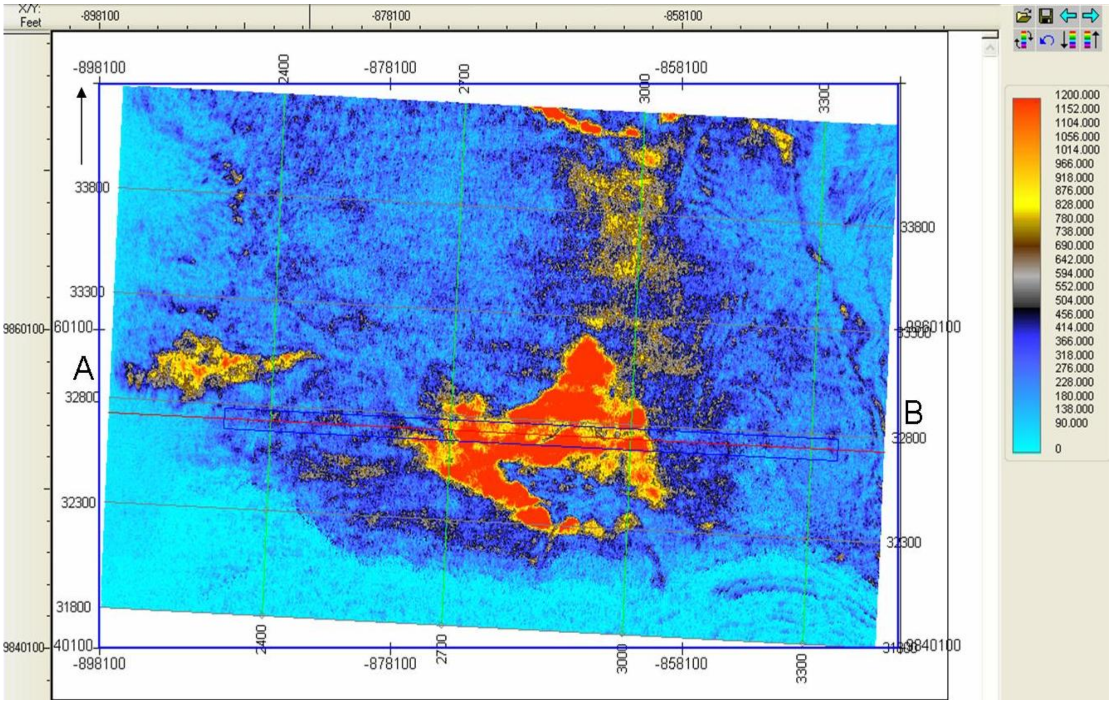

Figure 4.33: Horizon slice on the high-resolution band-limited near-stack impedance inversion.

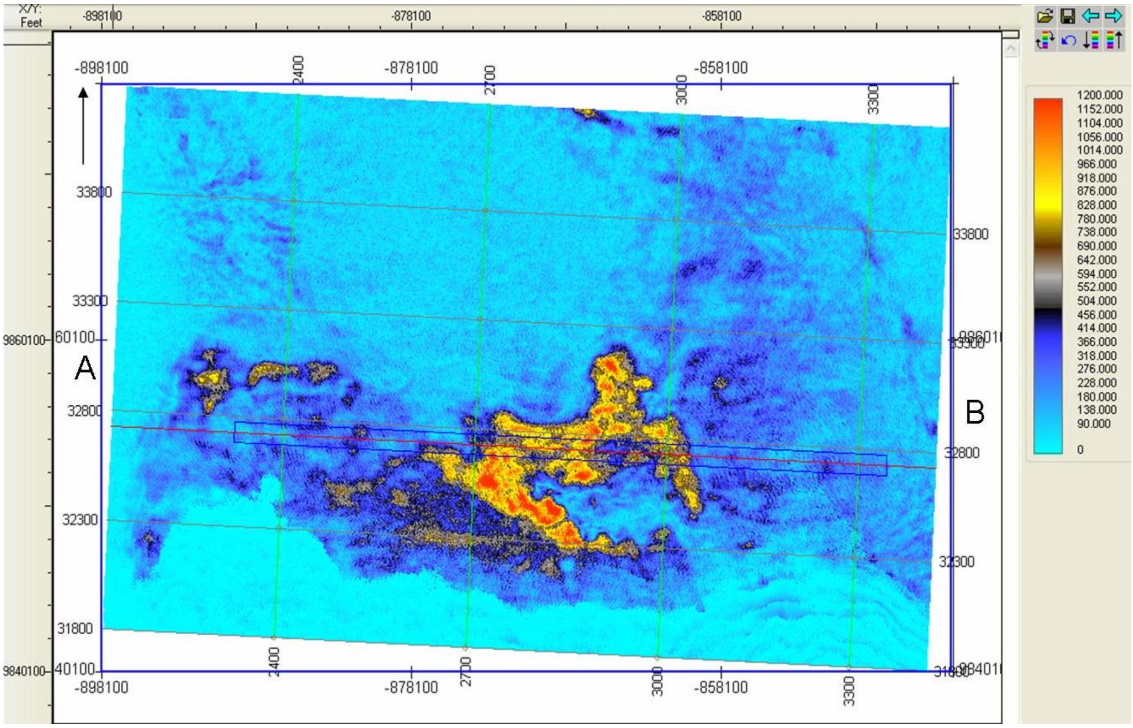

Figure 4.34: Horizon slice on high-resolution band-limited far-stack impedance inversion.

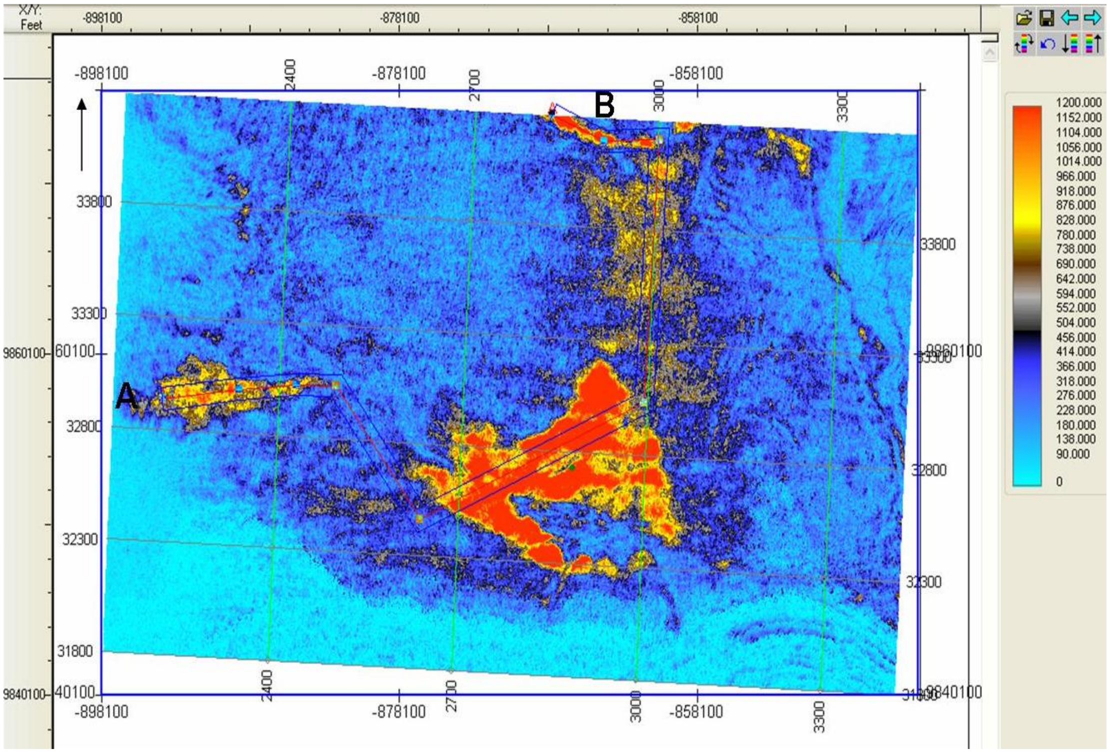

Figure 4.35: Horizon slice on high-resolution band-limited near-stack impedance inversion showing arbitrary line A-B.

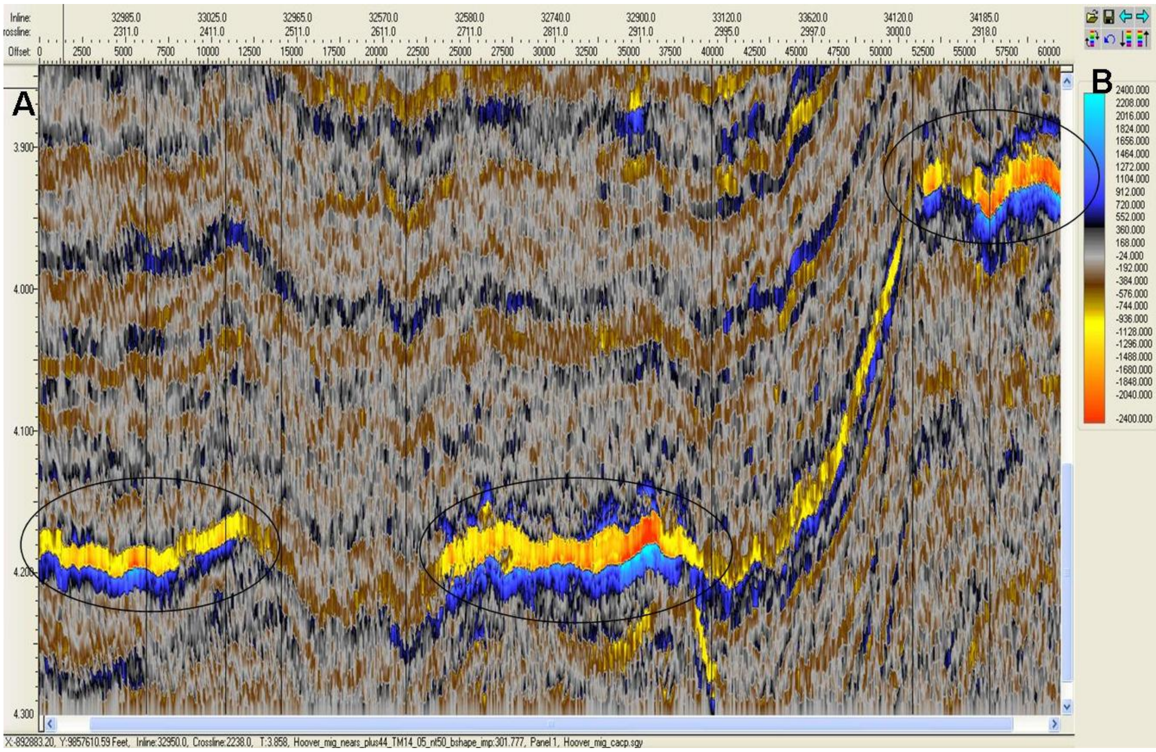

X:-892883.20, Y:9857610.59 Feet, Inline:32950.0, Crossline:2238.0, T:3.858, Hoover_mig_nears_plus44_TM14_05_nt50_bshape_imp:301.777, Panel 1, Hoover_mig_cacp.sgy

Figure 4.36: Cross-section of high-resolution band-limited near-stack impedance inversion from arbitrary line A-B of figure 4.25 highlighting bright spots.

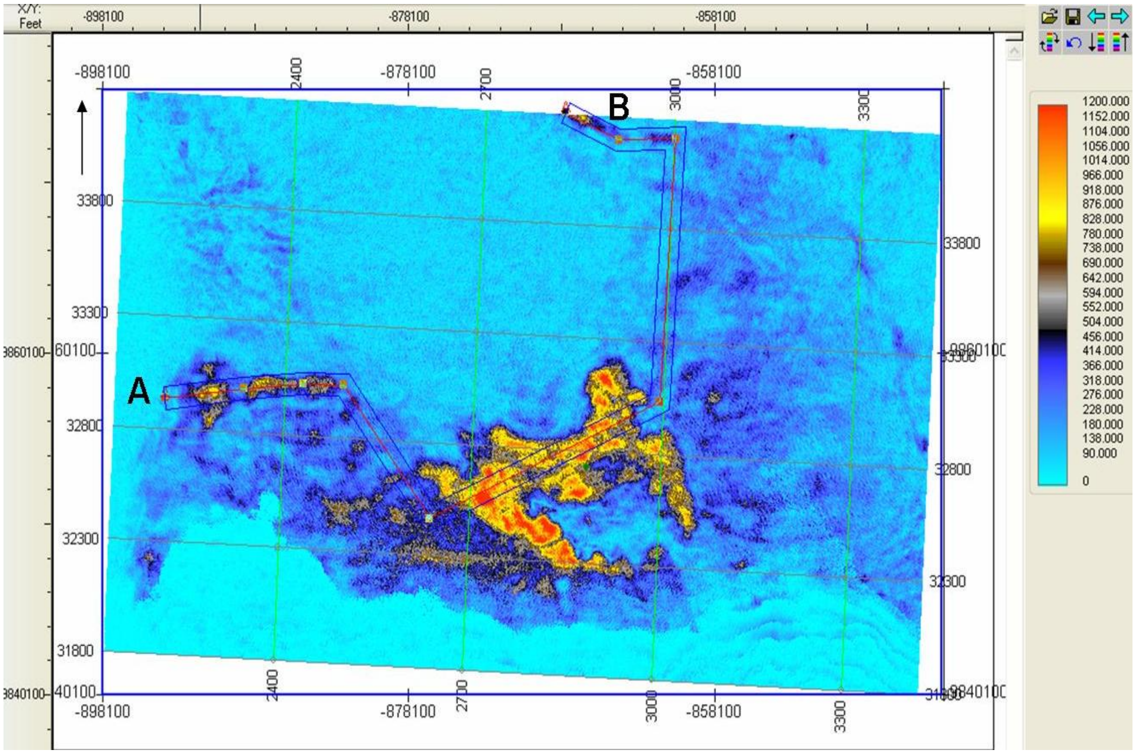

Figure 4.37: Horizon slice on high-resolution band-limited far-stack impedance inversion showing arbitrary line A-B.

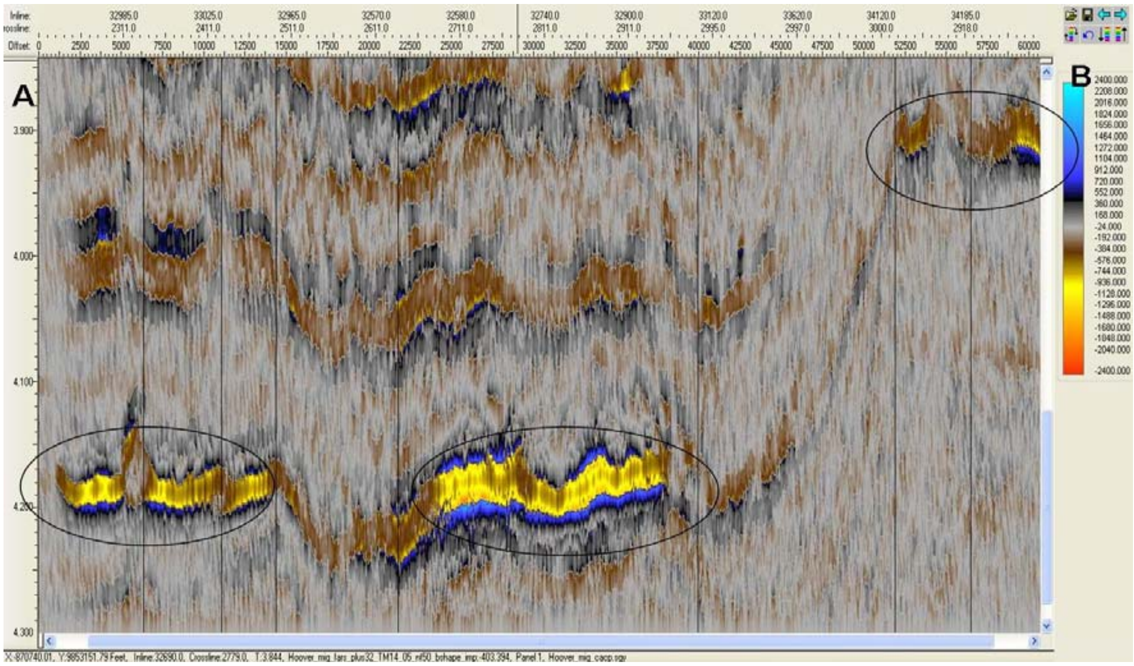

Figure 4.38: Cross-section of high-resolution band-limited far-stack impedance inversion from arbitrary line A-B of figure 4.27 showing change in impedance of bright spots.

4.4.2 Comparison of high-resolution band-limited impedance inversion with input seismic

To assess improvements in vertical and/or horizontal resolution observed on Hoover seismic data after application of high-resolution band-limited impedance inversion, vertical sections and horizon slices from input seismic (-90^0 phase rotated), reflectivity, and impedance volumes are compared. The highlighted areas with arrows show a section of the reservoir which appear to be homogeneous in the input seismic (Fig. 4.39). However, the reflectivity and impedance volumes (Figs. 4.40 and 4.41 respectively) show improved vertical resolution and heterogeneity of some sections of the reservoir. Improved resolution is also observed in figure 4.42 where the reflectivity is compared with the input seismic. Horizon slices (Figs. 4.43, 4.44 and 4.45) show RMS amplitudes of input seismic, impedance, and reflectivity volumes between the top and bottom of the reservoir. Improved resolution of the reservoir is also observed in figure 4.44 and 4.45.

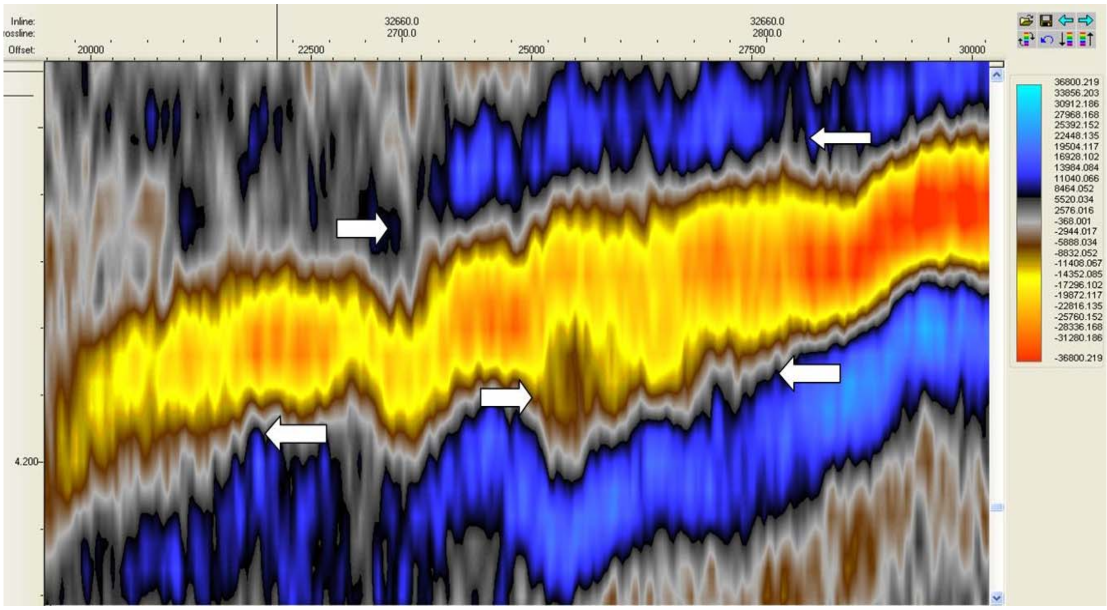

Figure 4.39: Input near-stacked seismic volume (-90^0 phase rotated) with black arrows indicating some areas for which resolution will improve.

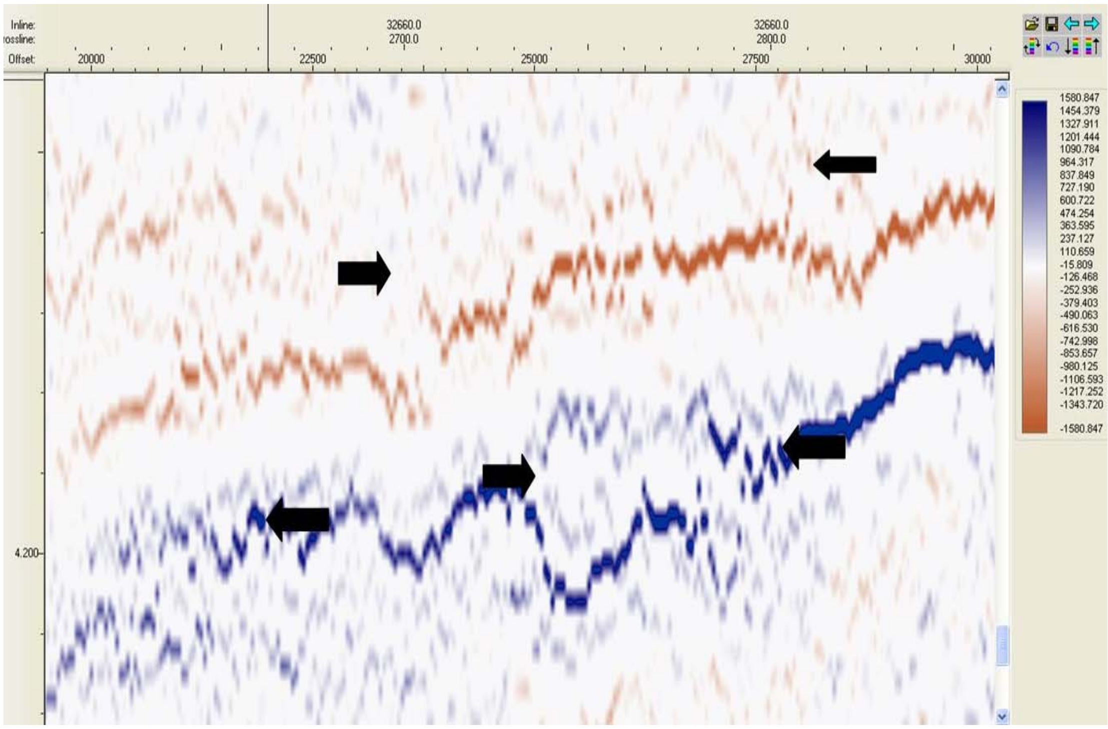

Figure 4.40: Reflectivity volume obtained from spectral inversion of seismic volume in figure 4.39, with black arrows indicating some areas of improved resolution.

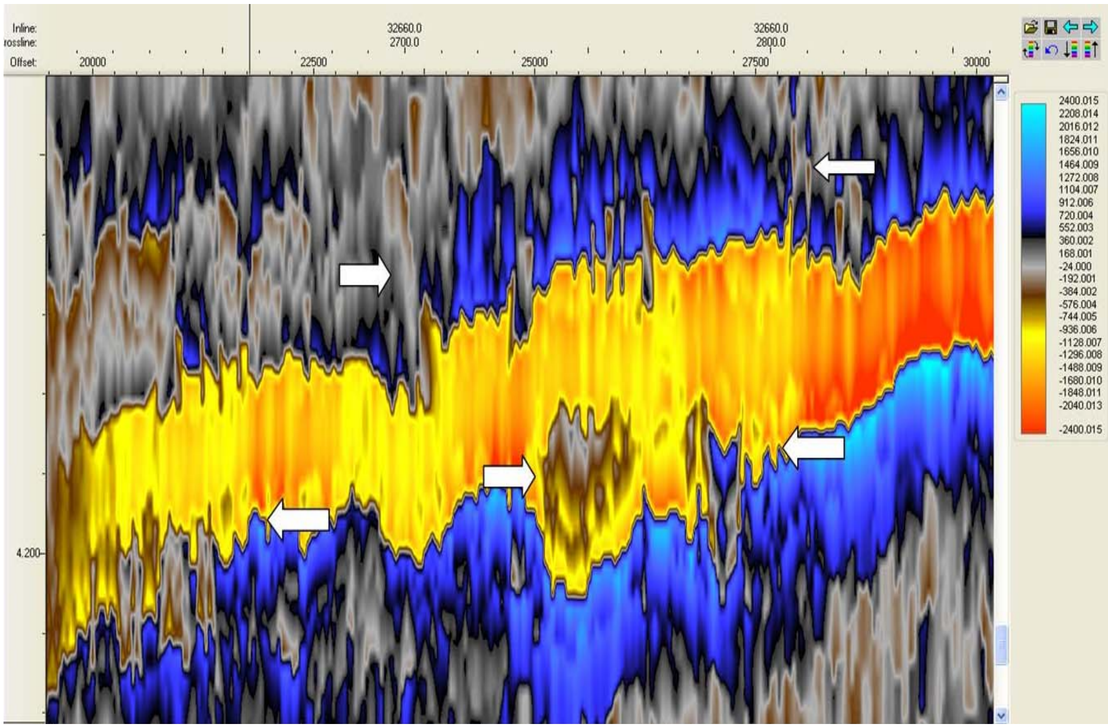

Figure 4.41: Band-limited impedance volume obtained from integration of reflectivity volume in figure 4.40.

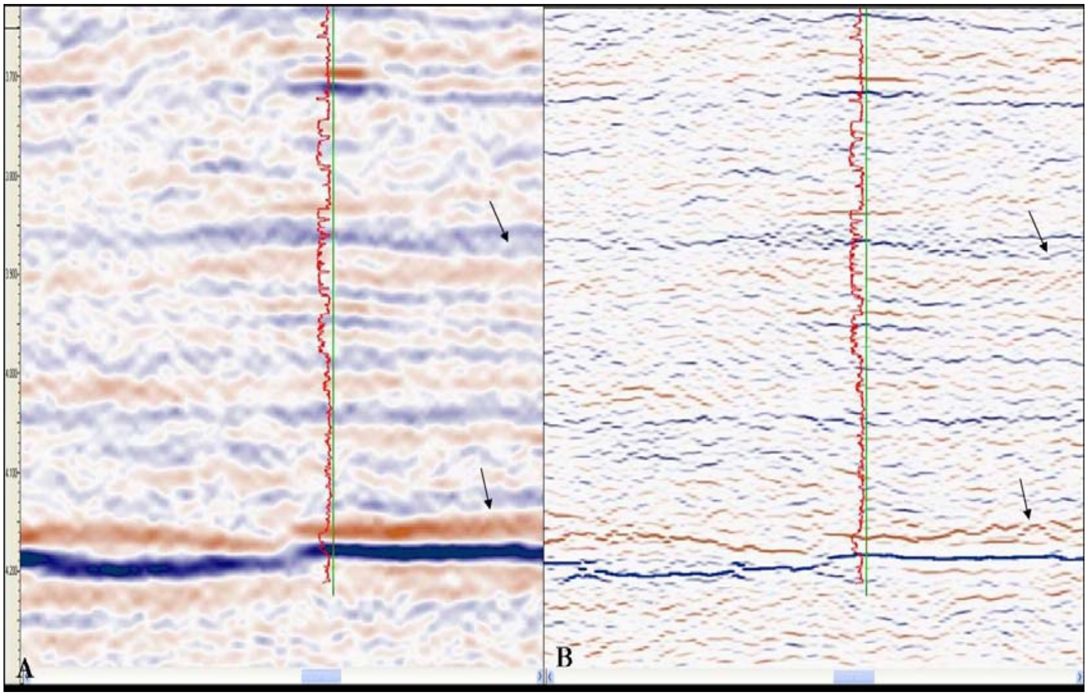

Figure 4.42: (A) Input seismic volume and (B) Reflectivity volume obtained from spectral inversion of seismic volume, with arrows indicating some areas of improved resolution.

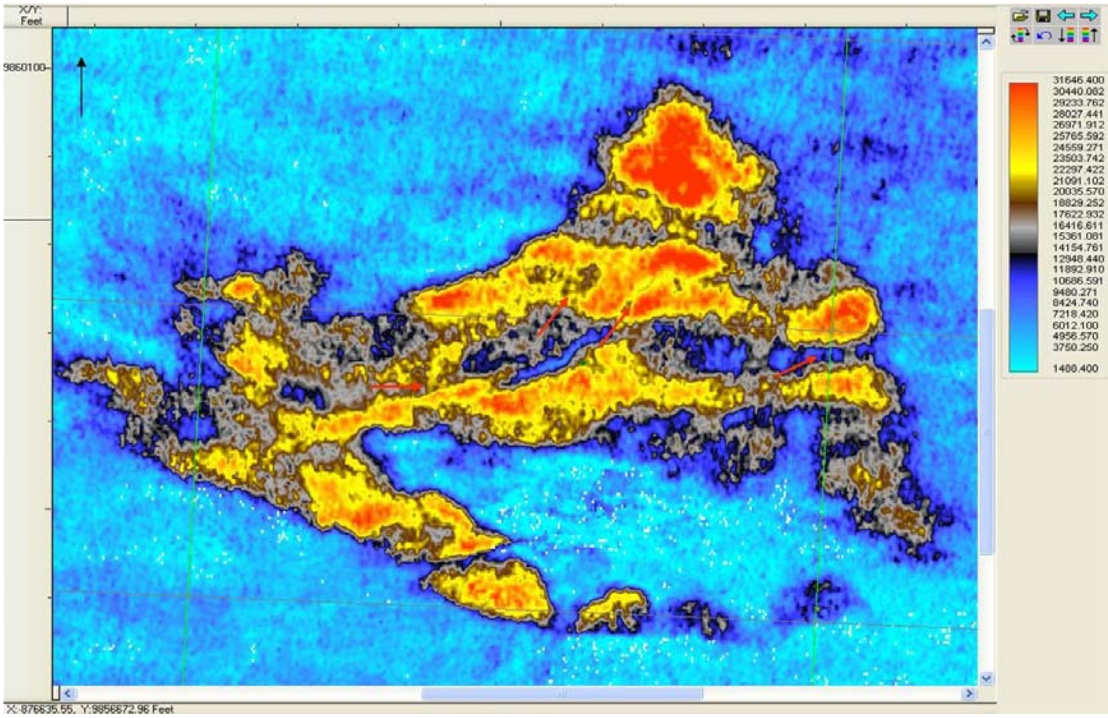

Figure 4.43: Input seismic RMS amplitude horizon slice through the reservoir with arrows indicating some areas for which resolution will improve.

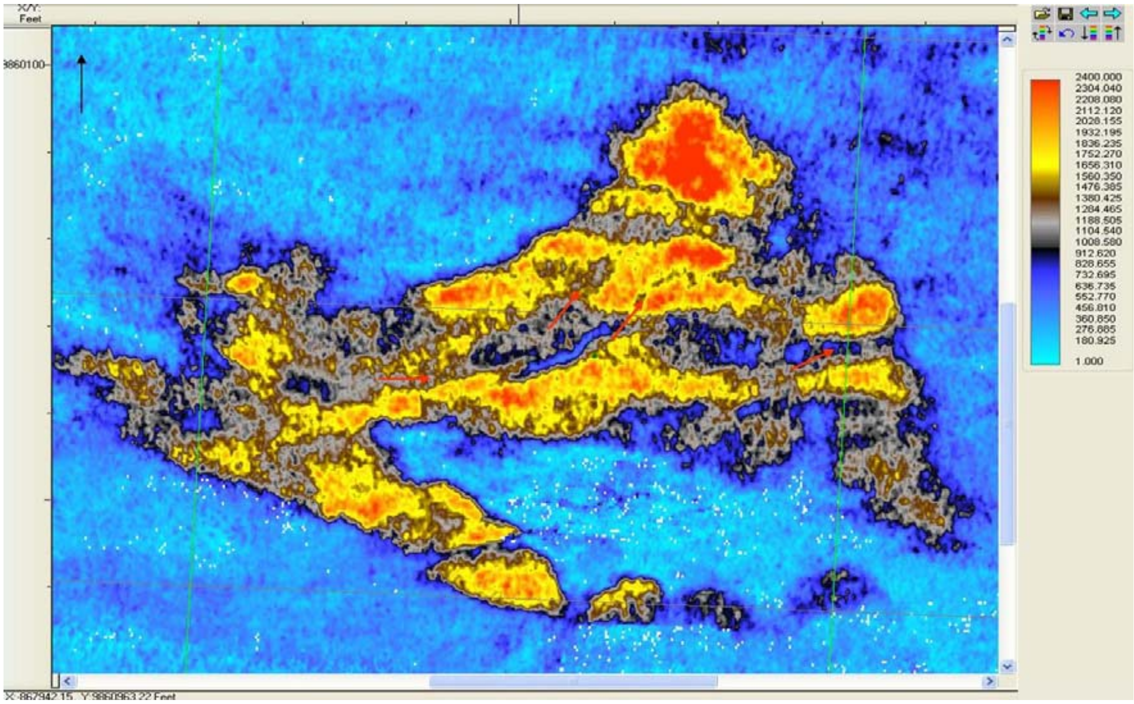

Figure 4.44: High-resolution band-limited impedance RMS amplitude horizon slice through the reservoir with arrows indicating some areas with improved resolution.

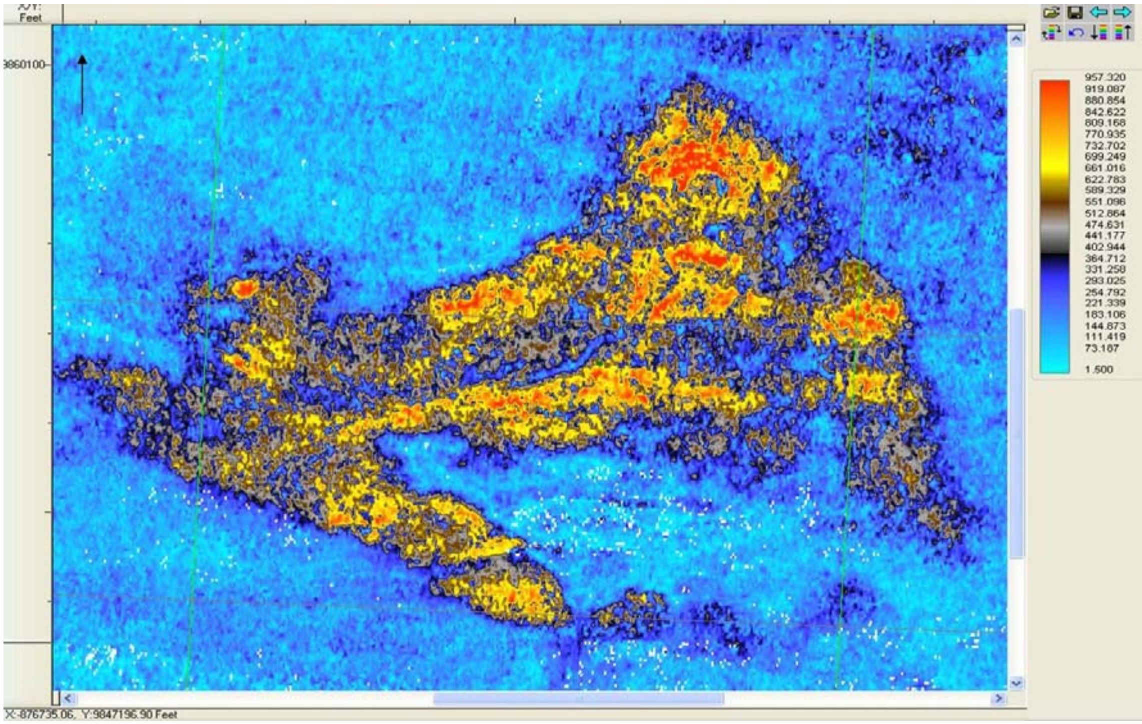

Figure 4.45: Reflectivity volume RMS amplitude horizon slice showing improved resolution of the reservoir.

4.5 Limitations of inversion methods

It is important to note that if the acquired data do not illuminate all sections of the subsurface, such information may not be recovered by inversion (Treitel and Lines, 2001). Francis (2002, p.2) also noted that “seismic inversion is an averaging process, caused both by minimization and by bandwidth limitations”. Lastly, inversion is also known to be non-unique, as there is more than one possible model which may fit the seismic data. However, solutions can and have been constrained to give a more likely result.

Chapter 5: Conclusions

During the course of this research, Hoover field data (seismic and well logs) have been investigated for hydrocarbons using 3D seismic attributes, conventional AVO analysis, and post-stack impedance inversion methods.

Three-dimensional interpretations of the seismic data show that the reservoir is made of turbidites sands and that the hydrocarbon-saturated section is a bright spot which is slightly elevated by the underlying salt body. It also displays apparent Class IV AVO properties. In the process of validating the presence of hydrocarbons from 3D interpretations, some questions raised by Brown (2006) have been answered. These answers include: (1) there is a reflection at the top and another at the bottom of the reservoir, (2) the reflection from the reservoir is anomalous in amplitude, (3) the seismic amplitude anomaly is structurally consistent, and (4) it is also large relative to the background values, with a ratio of about 3:1 i.e. 300 % increase.

Logs in the survey area are made of stacked sandstone and shale sequences. The reservoir sands, about 77 ft (≈23 m) thick, are characterized by low bulk densities, low P-wave velocities, and relatively higher resistivities and porosities compared to the overlying shales. The reservoir however is a low-resistivity oil reservoir with values below 10 ohm-m.

Fluid substitution, AVO modeling and analysis shows that whereas amplitude of brine sands decreased rapidly with offset, oil- and gas-sand amplitudes on synthetics decreased relatively slower (Figs. 3.34, 3.35 and 3.36). AVO attributes based on gradient (B), intercept (A), and P-wave (Rp) and S-wave (Rs) reflection coefficients on synthetics and extracted seismic traces shows that the AVO product is not good for Class IV environment

(Figs. 3.40 and 3.41). However, attributes such as scaled Poisson's ratio change (Figs. 3.42, 3.43, 3.56 and 3.57), fluid factor and sum of reflection coefficients produced better results. Although the AVO effect on oil is minimal when considered in isolation (Fig. 3.35), it is significant when compared with brine (Fig. 3.34), such that one is able to discriminate oil from brine in Hoover field (Figs. 3.50 and 3.51). This is because brine has a less negative intercept compared to oil and this decreases faster with offset, unlike oil which decreases very slowly with offset.

Both absolute and relative impedance inversion results show sharp contrast between oil-saturated reservoir sands with the encasing shales, as well as varying degrees of contrast between oil- and brine-saturated portions of the reservoir, depending on the inversion method used. The far-stack high-resolution impedance inversion resulted in a smaller number of bright amplitudes, compared to the near-stack, as a result of the faster decrease in amplitude of shale upon shale and shale upon brine sands compared to shale upon oil-sands. In addition to the central portion of the reservoir, low-impedance sands are also observed in the northern and western portions of the reservoir (Figs. 4.35 to 4.38). At far offset, the bright spot left in the reservoir is probably hydrocarbon-saturated turbidites. A comparison of the absolute impedance inversion results shows that the model-based inversion produced the best correlation with the synthetic generated after inversion, relative to the sparse-spike and band-limited AI inversion. Although the high-resolution impedance inversion (Figs. 4.40 and 4.41) shows that the oil-saturated section of the reservoir is not as homogenous as shown on the input near-stacked seismic volume (Fig. 4.39), it gives results similar to other inversion methods carried out with an initial model, thereby increasing ones confidence on the inversion results.

6. References

Asquith, G. and Krygowski, D., 2004, Basic Well Log Analysis (2nd edition), AAPG.

Batzle, M., and Wang, Z., 1992, Seismic properties of pore fluids: Geophysics, Vol. 57, No. 11, 1396-1408.

Boorman, C., Cowgill, M., Ginal, E., Mandley, R., Thompson, J., Roberts, G., and Archer, S., 2006, Huge potential still waiting in the Gulf of Mexico: GEO Expro Issue No. 4/5.

Boyd, A., Davis, B., Flaunm, C., Klein, J., Sneider, R., Sibbit, A., and Singer, J., 1995, The lowdown on low resistivity pay: Oilfield Review, 4-18.

Brown, A.R., 2004, Interpretation of Three-Dimensional Seismic Data (6th edition), AAPG Memoir 42 and SEG Investigations in Geophysics, No. 9.

Burtz, O., Matteucci, G., and Meyer, W., 2002, Model-based calibration of band-limited impedance data: Hoover field, SEG International Exposition and 7th Annual Meeting.

Castagna, J.P., and Swan, H.W., 1997, Principles of AVO crossplotting: The Leading Edge, Vol. 4, No. 16, 337-342.

Castagna, J.P., Swan, H.W., and Foster, D. J., 1998, Framework for AVO gradient and intercept interpretation: Geophysics, Vol. 63, No. 3, 984-956.

Chiburis, E., Franck, C., Leaney, S., McHugo, S., and Skidmore, C., 1993, Hydrocarbon detection from AVO: Oilfield Review, 44-50.

Chopra, S., Portniaguine, O., and Castagna, J. P., 2006, Seismic resolution and thin-bed reflectivity inversion: CSEG Recorder, 19-25.

Cogswell, T.L., 2001, Diana basin development – a pragmatic approach to the exploitation of two deepwater GOM fields: AAPG Annual Convention, Denver, 6 p.

Connolly, P., 1999, Elastic impedance: The Leading Edge, Vol. 18, No. 4, 438 - 452.

Encarta, 2009, http://encarta.msn.com/dictionary_/attribute.html accessed 02/18/2009

Francis, A., 2002, Deterministic inversion – Over due for retirement? Petroleum exploration society of Great Britain (PETEX) 2002 Conference, 1-8.

Gao, D., 2007, 3D seismic interpretation, unpublished lecture notes.

Gluyas, J., and Swarbrick, R., 2004, Petroleum Geoscience, Blackwell Publishing Company, 359 p.

Hamada, G.M., Al-Blehed, M.S., and Al-Awad, M.N.J., 2000, Nuclear magnetic resonance log evaluation of low resistivity sandstone reservoirs by-passed by conventional logging analysis: Society of Petroleum Engineers International, SPE 64406, 1-11.

Hilterman, F., 2001, Seismic amplitude interpretation, SEG/EAGE Distinguished Instructor Short Course, Distinguished Instructor Series, No. 4.

Latimer, R., Davidson, R., and van Riel, P. 2000, An interpreter's guide to understanding and working with seismic-derived acoustic impedance data: The Leading Edge, Vol. 19, 242-256.

Li, Q., 2001, LP sparse-spike inversion, Strata technique document, Hampson-Russell software services limited, 14 p.

Liner, C. L., 2004, Elements of 3D Seismology (2nd edition): PennWell Corporation, 608 p.

Moore, J.C., Klaus, A., et al., 1998, Explanatory notes: Proceedings of the oceanography drilling program, Initial reports, Vol. 171A, 11-15.

Pendrel, J.V., and van Riel, P., 2000, Effect of well control on constrained sparse-spike seismic inversion. CSEG Recorder, Vol. 21, 18-28.

Portniaguine, O., and Castagna, J. P., 2005, Spectral inversion: Lessons from modeling and Boonesville case study, 75th SEG Meeting, 1638-1641.

Posamentier, H. W., and Walker, R.G., 2006, Deep water turbidites and submarine fans, *in* Facies Models Revisited, SEPM Special Publication, No. 84, 399-520.

Posamentier, H. W., Davies, R. J., Cartwright, J. A., and Wood, L., 2007, Seismic geomorphology – an overview, *in* Posamentier, H. W., Davies, R. J., Cartwright, J. A. and Wood, L., eds., Seismic Geomorphology: Applications to Hydrocarbon Exploration and Production. Geological Society, London, Special Publications, No. 277, 1-14.

Ross, C. P., 2000, Effective AVO crossplot modeling: A tutorial, Geophysics, Vol. 65, No. 3, 700-711.

Russell, B., 2005, Strata workshop: Theory and exercises in seismic inversion and AVO, unpublished lecture notes.

Russell, B., and Hampson, D., 1999, AVO theory, Hampson-Russell software services limited, 69 p.

Russell, B., and Hampson, D., 2006, The old and the new in seismic inversion: CSEG Recorder, 5-11.

Rutherford, S.R., and Williams, R.H., 1989, Amplitude versus offset variations in gas sands, Geophysics, Vol. 54, No. 6, 680 - 688.

Savic, M., VerWest, B., Masters, R., Sena, A., and Gingrich, D., 2000, Elastic impedance inversion in practice: SEG Expanded Abstracts Vol. 19, 689.

Selley, R., 1985, Elements of Petroleum Geology, W. H. Freeman and Company, 449 p

Sen, M. K., 2006, Seismic Inversion, Society of Petroleum Engineers, U.S.A, 120 p.

Sheriff, R. E., 2002, Encyclopedic Dictionary of Applied Geophysics (4th edition), SEG, 429 p.

Shrestha, R. K., 2008, Reservoir characterization of high impedance sands in the Ada field, North Louisiana, USA: GSH/SEG Spring Symposium Technical Program, 5 p.

Slatt, R. M., 2006, Stratigraphic reservoir characterization for petroleum geologists, geophysicists and engineers, *in* Cibitt, J., ed., Handbook of Petroleum Exploration and Production, Vol. 6, 478 p.

Smith, T. M., Sondergeld, C.H., and Rai, C.S., 2003, Gassmann fluid substitutions: A tutorial, Geophysics, Vol. 68, No. 2, 430-440.

Treitel, S., and Lines, L., 2001, Past, present and the future of geophysical inversion-A new millennium analysis: Geophysics, Vol. 66, No. 1, 21-24.

Veeken, P. C. H., 2007, Seismic stratigraphy, basin analysis and reservoir characteristics, *in* Helberg, K., and Treitel, S., eds., Handbook of Geophysical Exploration, Seismic Exploration Vol. 37, 509 p.

Wang, Z., 2001, Fundamentals of seismic rock physics: Geophysics, Vol. 66, 398-412.

Weimer, P., and Slatt, R.M., 2007, Petroleum geology of deep water settings, AAPG Studies in Geology No. 57, AAPG/Datapages Discovery Series No. 8.

http://www.worldatlas.com/aatlas/infopage/gulfofmexico.htm accessed 02/18/2009

http://earth.google.com/ accessed 04/18/2009